Chapter 1 : General Introduction

Global food security remains an imposing challenge for the 21st Century. The burgeoning human population (c. 40% increase by 2030) is applying increased demand for crop products on an agriculture sector where resources are finite (Ingram *et al.* 2012). The area of available arable land for farming remains stable (or is decreasing) and there is already heavy dependence on supply-limited fertilisers to maintain crop yields (Mann 1999; Tillman *et al.* 2002). Currently, 30-50% of the world population depend on crop products grown with fertiliser application (Ingram *et al.* 2012). This supply pinch is accentuated by the decreasing availability of readily accessible phosphate rock reserves, which are the primary product for ameliorating the world's second most limiting nutrient deficiency (Vance *et al.* 2003). It is therefore logical to pursue greater fertiliser use efficiency in crop breeding programs with the intention to increase productivity with limited nutritional inputs.

There has been substantial productive progress in many agriculturally significant species on the back of careful selection and breeding, notably of above ground plant features. Further productive increases, particularly in hostile environments, are likely to come from the improvement of the plant organs that acquire water and nutrient resources, the roots (Lynch 2007). Current breeding programs routinely use criteria that inadvertently select plants with high internal nutrient use efficiencies (NUE), however, there is significant opportunity to improve plant productivity and fertiliser use efficiency by selecting plants that have more competitive macro-nutrient acquisition strategies (NAE) (Henry *et al.* 2010; Ingram *et al.* 2012; Lynch 2007; Zhu *et al.* 2004). Root system architecture (RSA) influences the edaphic resources available to the plant and differential architecture can improve plant productivity in resource limiting and spatially heterogeneous environments (Henry *et al.* 2010; Ho *et al.* 2004; Hodge 2004). For example, shallow rooted variants have exhibited improved P uptake, while deep-rooted variants can be more drought tolerant (Henry *et al.* 2010; Ho *et al.* 2004; Lynch *et al.* 2001). These constitutive attributes can be complemented by plastic responses like the proliferation or extension of lateral branching to high concentration patches of phosphorus or nitrogen. These localised

responses can substantially improve nutrient uptake for low mobility ions like P (Hodge 2004). The limitation to improving RSA through breeding programs is the ability to rapidly and reliably analyse root system characteristics (a 3D trait) (Ingram *et al.* 2012) through opaque soil matrix.

Abundant genetic breeding tools and improving levels of automated phenomic technology has initiated the development of high-throughput methods for phenotyping RSA, commonly using transparent media such as gellan gum (Clark *et al.* 2011; Ingram *et al.* 2012; Iyer-Pascuzzi *et al.* 2010). This enables rapid and high quality assessment of root system traits but is unable to fully imitate field physical and chemical properties, especially spatial heterogeneity. The ideal solution is therefore to image the root system in a natural soil using technology that makes the soil itself 'transparent'. The use of X-ray CT for analysis of soils has been under development for c. 30 years (Mooney *et al.* 2012) but recent improvements in X-ray sources, detector sensitivity and computational capabilities have converged to allow the rapid assessment of field relevant sized samples (e.g. Scan time approx. 4 mins (Flavel *et al.* 2012)). X-ray CT is amongst a small number of techniques that are able to quantify RSA in 3D and at high spatial resolutions, exposing a suite of architectural measures (e.g. branching angle, root path tortuosity and spatial distributions) that have been difficult or impossible to establish with more conventional methods (Gregory *et al.* 2003; Perret *et al.* 2007). Coupled with the non-destructive (temporally continuous) capacity of the technique, X-ray CT offers significant potential for expanding the understanding of the root: soil interface.

Despite the substantial time since the first application of X-ray CT to root and soil studies, the technique is only now emerging as practical tool (Gregory *et al.* 2009; Mooney *et al.* 2012). As X-ray instruments have improved in their capacity, speed, contrast and resolution, the limitation for large-scale implementation has shifted from acquisition to processing challenges. Processing challenges were, of-course, always present (Kaestner *et al.* 2008; Mairhofer *et al.* 2012; Mooney *et al.* 2012; Perret *et al.* 2007) but were masked by the impracticalities and low sample throughput possible using the CT technology (Gregory *et al.* 2009). It now remains to develop a fast and robust root segmentation and RSA analysis package capable of extracting pertinent root architectural information from tomographs.

This thesis aims to visualise the morphological responses of wheat root systems to localised P supply using X-ray CT. The implications and significance of this thesis is collated in a General Discussion (Chapter 7) and recommendations for further research opportunities using this technique are briefly discussed. This thesis is arranged in the following structure:

Initially, a thorough review of the literature will be made, first analysing the role and behaviour of P in the plant and in the soil environment. Since P is heterogeneously distributed and immobile in soil, plants have adapted several acquisition strategies to improve P uptake (Hodge 2004). These also will be reviewed with particular reference to the morphological response. Finally the use of imaging and X-ray CT for below ground and particularly root system analysis will be examined. Due to the formidable scope of the review, all of these topics will not be exhaustively explored. However, several relevant and excellent reviews will be identified for further reading. More relevant literature will be cited in the experimental chapters. Both during the course of the review and in conclusion, pertinent deficiencies in the body of literature will be highlighted, but conclude that X-ray CT as a technique has unique potential to explore the spatial dynamics of morphological responses to P.

In the absence of standardised protocol for this emerging technology, a series of pilot studies and a protocol are described to optimise the experimental equipment and scan parameters for root research and root system analysis. As indicated above, image processing has become the major challenge for analysing 3D root architecture, which has placed greater importance in achieving the best possible image quality. Chapter 3 describes the general X-ray imaging principles to optimise scan parameters with specific application and relevance to the University of New England's laboratory based micro-CT scanner (The GE Phoenix V|tome|xs).

Having optimised experimental conditions, image processing poses the next major challenge to root architecture characterisation. In Chapter 4 methods for sequential scan stacking, root segmentation and extracting RSA information are discussed. Stages in the development of the processing methods are described which are used in

experimentation reported in the subsequent chapters. Due reference will be made to the following chapters during the course of Chapter 4.

Chapter 5 validates the application of X-ray CT for observing relatively large and complex root wheat root systems using root length as a relevant and sensitive descriptor of root architecture and function. In addition the trial sought to identify, if any, the effect of repeated X-ray CT scanning at high energy on the key root architectural characteristics; branching, root length and diameter.

Chapter 6 explores the spatial specificity of the local proliferation response in young wheat plants to a highly local band of phosphorus. With the application of more refined computational algorithms, branching density, root length density and branching angles are extracted from the tomographs.

Chapter 2 : Literature Review

The work contained in sections 2.4 to 2.5.6 of this chapter has been published as part of an invited review with the *European Journal of Soil Science*.

Helliwell J.R., Sturrock C.J., Grayling K.M., Tracy S.R., **Flavel R.J.**, Young I.M., Whalley W.R., Mooney S.J. (2013), Applications of X-ray computed tomography for examining biophysical interactions and structural development in soil systems: a review. *European Journal of Soil Scienc*e, DOI: 10.1111/ejss.12028

2.1 Introduction- the global significance of phosphorus

Phosphorus (P) remains the second most limiting nutrient to plant growth globally, impacting the productive capacity of an estimated 30-40% of the world's arable land area (Vance *et al.* 2003; Yang *et al.* 2007). Fertiliser application is a common and effective solution (particularly in developed nations) but is often expensive and unsustainable in the long term. Despite the controversy surrounding the longevity of phosphate reserves, it is clear that the world's rock phosphate supply is finite and the easily accessible sources will eventually decline causing significant increases in the price and availability of P fertilisers (Bumb *et al.* 1996; Cordell *et al.* 2009; Vance *et al.* 2003). Coupled with a rising global population and the concordant need to double agricultural production by 2020 (Gyaneshwar *et al.* 2002) the necessity for improvements in P fertiliser use efficiency and plant P acquisition efficiencies are logical (Ingram *et al.* 2012).

As a key component of plant biochemistry, P is required in high concentrations (~0.2% dry plant tissue) and critical for maturity and high yield potential in cropping species (Grant *et al.* 2005; Schachtman *et al.* 1998). Phosphorus is often heterogeneously distributed in soil due in part to its low mobility and the spatial variability of the soil itself (Hutchings *et al.* 2004; Robinson 2005). As a result, plants have developed many mechanisms to respond to edaphic P constraints including architectural, chemical and symbiotic adaptations to improve P acquisition (Hodge 2004; Schachtman *et al.* 1998). The former is the focus of this review. The spatial arrangement of the root system (root system architecture) significantly influences the

nutrient and water resources available to the plant and, where these resources are limiting, determines plant productivity (Lynch 1995; Mooney *et al.* 2012). Large variations in root system architecture have been observed in response to environmental stimuli and provide opportunity for improving plant nutrient acquisition efficiencies (Drew 1975; Henry *et al.* 2010; Lynch 2007). Root system studies are hampered by the opaque nature of the soil and consequently methods are often laborious and spatially or temporally discontinuous (Gregory 2006; Lynch 1995). X-ray Computed Tomography (CT) offers significant opportunities to observe and map the spatial and temporal dynamics at the root soil interface (Mooney *et al.* 2012). Despite the 30-year history of using X-ray CT for root studies, the technique is underdeveloped (Mooney *et al.* 2012). However, recent technological advances have allowed faster processing of large datasets with complex algorithms permitting the observation of root systems as they respond morphologically to representative field like conditions (Hutchings *et al.* 2004).

2.1.1 Role of phosphorus in the plant

Phosphorus is an important component of many biochemical pathways in virtually all known forms of life. In plants, it is essential for photosynthesis and respiration, nucleic acid synthesis, enzyme activation, membrane synthesis and stability (Grant *et al.* 2005; Schachtman *et al.* 1998; Vance *et al.* 2003). With such substantial contribution to the plants biochemistry it is required in large quantities (termed a macro-nutrient) and typically represents 0.2% (ranging between 0.05-0.5% species dependent) of plant dry tissue weight (Schachtman *et al.* 1998; Vance *et al.* 2003). The high tissue concentrations are approximately 3 orders of magnitude greater than the abundance of inorganic phosphate (P_i) ions in soil (typically <10μM), consequently P is taken up by active transport as orthophosphate, the form of which ($H_2PO_4^-$ or HPO_4^{2-}) is dependent on soil pH (pKa for H_3PO_4 to $H_2PO_4^-$ is 2.15 and for $H_2PO_4^-$ to HPO_4^{2-} is 7.2) (Perez Corona *et al.* 1996; Schachtman *et al.* 1998; Vance *et al.* 2003). Phosphorus is readily translocated in the phloem tissue and plants differentially partition, redistribute and store P in and to different regions of the plant in response to environmental conditions (Grant *et al.* 2005). These mechanisms allow the plant to buffer tissue P concentration and implement strategies to attain more P, particularly later in maturity. However, in the early stages of annual cereal crops, P

requirements are higher and sufficient P supply for the first 6 weeks influences final yield more than late season nutrition (Grant *et al.* 2005). Insufficient P supply in this window is thought to retard meristem development resulting in reduced dry matter production and fewer initiated kernels (Grant *et al.* 2001). Therefore early season P availability is critical for optimum growth, development and ultimately yields of annual cropping species.

2.1.2 Phosphorus behaviour in soil

A large proportion (98-99%) of P in soil is in adsorbed, mineral or organic forms and consequently unavailable to plants (Pierzynski *et al.* 2005) (Figure 2.1). Orthophosphate in the soil solution is the only form of P plants can acquire and its concentration is determined by the equilibrium of precipitation and sorption reactions as well as microbially mediated breakdown of organic matter (Vance *et al.* 2003) . As a highly reactive molecule, P_i readily forms complexes with Fe, Al and Ca, the relative abundance of the complexes formed is determined by the prevailing soil pH (Gyaneshwar *et al.* 2002; Haynes *et al.* 2001; Perez Corona *et al.* 1996). Phosphate is also specifically adsorbed to the soil colloid where Fe and Al hydroxides form covalent bonds to the P_i molecule (Yang *et al.* 2007). The types and amount of clay minerals present, the abundance of metal hydroxides, ions that compete for P sorption sites (e.g. Sulphate or molybdate), pH, ionic strength and conditions affecting microbial growth all influence the equilibrium of solution P_i concentration (Horst *et al.* 2001; Vance *et al.* 2003). For example, highly weathered acid soils with a high prevalence of Fe and Al oxides such as Ferrosols (Isbell 2012) have high sorption capacities and generally low concentrations of bioavailable P (Haynes *et al.* 2001). Likewise, Calcarosols (Isbell 2012) also have low solution P concentrations but in this case the dominant mechanism is precipitation of insoluble Ca phosphate minerals (Lombi *et al.* 2004). The reactivity, low solubility of many P_i complexes and the high level of microbial demand for P in soil contributes to the typically low solution concentrations (<10μM) observed in soil (Gyaneshwar *et al.* 2002).

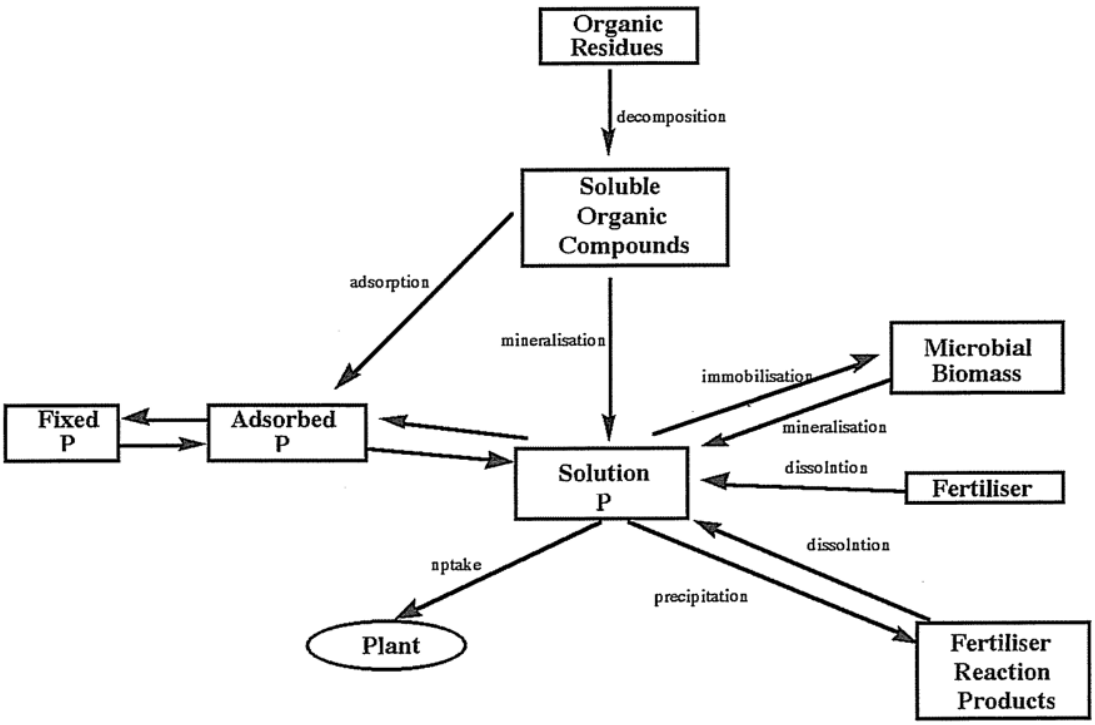

Figure 2.1| The phosphorus cycle, reactions that influence the solution P concentration. Reproduced from Moody *et al.* (2005).

Understandably then, P_i is the most immobile macronutrient and the least available under most environmental conditions (Ramaekers *et al.* 2010). While mobile nutrients, such as nitrogen, move by mass flow through the soil matrix, P_i moves by diffusion to the root surface and is many orders of magnitude slower. The diffusion rate of P through non-adsorbing soil is 10^{-12}-10^{-15} m^2s^{-1} (approx. 1mm in 10 days) (Gahoonia *et al.* 2001; Schachtman *et al.* 1998; Tinker *et al.* 2000). In comparison root uptake of P from the soil is much more rapid and consequently creates a cone shaped diffusion zone behind the root tip (Smith 2002). The radius of the depletion zone varies depending on root characteristics (such as root hair length) and soil type but usually extends 0.2-2.0mm from the root surface (Gahoonia *et al.* 2001; Vance *et al.* 2003). The depletion zone shifts the equilibrium in favour of dissolution or desorption of precipitated complexes or adsorbed P respectively. While this increases the P available to the plant, the process is typically slow (Smith 2002). In high concentration patches such as around fertiliser granules the rate of diffusion is thought to be substantially higher due to the steep concentration gradient (Grant *et al.* 2005).

The chemical interactions between P_i and the soil have two dominant implications for root systems. Firstly, the immobility of P_i in the soil means that P is often heterogeneously distributed in the soil volume. In both agricultural and natural ecosystems higher surface P concentrations occur due to litter accumulation and input of manures and fertilisers (Henry *et al.* 2010). Minimal or no-tillage practices and precision placement of starter fertilisers has served to intensify this pattern in higher input agricultural systems (Ma *et al.* 2009; Rose *et al.* 2009). Regardless of the fertiliser inputs into the system, P is typically heterogeneously distributed in the soil environment and provides opportunities for exploitation by changes in root system architecture (RSA) (Hodge 2004; Lynch *et al.* 2005). Secondly, the low diffusion gradient of P_i limits plant uptake of P from outside the rhizosphere. Therefore, to improve acquisition of P the root system must increase P interception or soil exploration (Gahoonia *et al.* 1997; Ramaekers *et al.* 2010; Schachtman *et al.* 1998). This matter will be discussed in greater detail below. While complex and environmentally specific, the chemical characteristics of P in soil simultaneously make P the second most limiting nutrient to global plant production and offer the basis for the root system architectural adaptions to overcoming this challenge.

2.1.3 Fertiliser use and efficiency

There is already significant global reliance on fertilisers, with 30-50% of the current global population dependent on products grown with the application of fertilisers (Ingram *et al.* 2012). Human population growth is estimated to increase the demand for phosphatic fertilisers by 50% by 2050 (estimates made in 2000) (Manske *et al.* 2000). Regardless of confusion in the literature regarding current phosphate rock reserves, market forces are expected to increase the cost of P fertiliser products into the future (Ingram *et al.* 2012) placing pressure on the agricultural sector for greater P use efficiency. Estimates of P fertiliser use efficiency vary with environment and crop species but are consistently low, ranging from 5-30% recovery in the first year (Lombi *et al.* 2004; Manske *et al.* 2000; Vance *et al.* 2003). One reason for the low uptake from fertiliser sources is that 80-90% of inorganic P fertilisers applied are rapidly adsorbed or form precipitates when applied to the soil (Gyaneshwar *et al.* 2002; Schachtman *et al.* 1998). To reduce losses to sorption processes in high phosphate buffer capacity (PBC) soils, fertilisers are often banded, saturating sorption

sites in local regions. This increases P availability from the fertiliser and often recovery but bands close to the surface are susceptible to drying, reducing P availability (Ma *et al.* 2007; Rose *et al.* 2009). There are also concerns that banding P fertilisers produces a smaller volume of enriched soil and a corresponding decrease in exposure to particularly small young root systems (Grant *et al.* 2001). With increasing pressure for higher crop productivity from increasingly expensive fertilisers, there is considerable impetus to improve the typically low P fertiliser use efficiency of current agricultural systems.

2.1.4 Improving phosphorus use efficiency

Fertiliser use efficiency is the product of plant fertiliser acquisition and internal nutrient use efficiency (Manske *et al.* 2000). Improvements to P use efficiency could be achieved by increasing the proportion of P available from fertiliser sources (by placement or fertiliser design), by developing plant uptake mechanisms (P uptake efficiency-PUPE) or by using alternative, more P efficient, physiological mechanisms (P utilisation efficiency-PUTE).

There are numerous plant physiological responses to P stress and most adaptations appear to increase plant competitiveness under stressed conditions. For example, redistribution and use of P reserves stored in the cellular vacuole can buffer tissue P concentration maintaining plant productivity in the early stages of P limitation (Grant *et al.* 2001; Ma *et al.* 2007; Vance *et al.* 2003). As P deficiency develops in common bean and maize, conversion of root cortical cells to aerenchyma can reduce respiration costs and release P compounds for maintained growth rates (Ramaekers *et al.* 2010). Alternative biochemical pathways that do not require as much P can be used. For example, increasing dependence on secondary rather than primary metabolism or using the hypothesised cyanide resistant respiration pathway and an alternative to the Cytochrome–C electron transport pathway reduces the P requirement for energy metabolism (Vance *et al.* 2003). In some instances, P components can be substituted for example, phospholipid molecules in photosynthetic membranes can be replaced with sulfolipids (Vance *et al.* 2003). However, the absence of these processes under sufficient P status may suggest a competitive disadvantage of these mechanisms such as decreased energy efficiency or reduced functionality. To this effect, oxidative

respiration rates in some species have been observed to decrease under P stress when low P use pathways are utilised (Vance *et al.* 2003).

Advances in fertiliser use efficiency have been observed with banding of P fertilisers in high PBC soils. The application of P_i into a small soil volume decreases the influence of sorption processes, improving the availability of fertiliser P to the plant (Jackson *et al.* 1996; Valizadeh *et al.* 2002). As shallow bands are susceptible to drying in low rainfall systems, further improvements may be achieved with deeper profile banding where water availability is less limiting (He *et al.* 2002; Ma *et al.* 2007; Rose *et al.* 2009). However, before available P can improve fertiliser recoveries it must be assimilated by the root system. Therefore, root system traits (including RSA) that improve access and uptake of P will contribute to improved PUE and productivity (Lynch 2007; Lynch *et al.* 2005; Mooney *et al.* 2012). Traits such as increased root exploration, length and density of root hairs, mycorrhizal infection, as well as up-regulated uptake transporters or excretion of acids and enzymes have all been recognised as potential objectives for improving PUPE (Manske *et al.* 2000; Smith 2002; Vance *et al.* 2003). As reviewed more exhaustively by Lynch (2007), breeding for macro nutrient acquisition strategies appears to be a more promising strategy than for nutrient use efficiency. Where PUTE is associated with current breeding objectives and has been subject to indirect selection, PUPE characteristics have not. In fact, the high nutrient media used in many breeding programs can apply neutral to negative selection pressure on efficient P uptake strategies (Lynch 2007). Consequently the variation observed in RSA traits should provide useful selection criteria for improvement of P recovery and efficiency in fertilised and unfertilised systems (Henry *et al.* 2010; Lynch 2005; Lynch 2007; Smith 2002).

2.2 Plant P acquisition strategies

The primary function of the root system is to capture water and nutrient resources from the soil (Fitter 1987; Gregory 2006). Plant responses for increased P acquisition fall into four broad categories; physiological and molecular level adaptations, symbiotic and architectural adaptations. Generally, physiological adaptations are rapidly regulated, reversible and act to increase the availability or rate of uptake of P

by the roots (Ma *et al.* 2008). They include adapting transport proteins to solution P concentrations, and producing chemical exudates capable of influencing rhizosphere chemistry to increase P availability (Strom *et al.* 2005; Yang *et al.* 2007). Both symbiotic and morphological adaptions are slower to implement, more enduring and function by increasing the volume of soil explored and commensurate P interception (Ma *et al.* 2008). Plant capture of immobile nutrients is directly correlated with root length and the volume of soil explored (Gahoonia *et al.* 1997; Horst *et al.* 2001; Officer *et al.* 2009). In this way root system architecture that increases the soil exploration such as root extension, branching density, root hair length or spatial arrangement specific to a patchy environment can lead to improved resource acquisition and increased plant competiveness (Lynch 2007). Likewise mycorrhizal infection can have significant productive advantages under P limiting conditions (Schachtman *et al.* 1998).

2.2.1 Physiological

Assimilation of P into plant tissue is by apoplastic diffusion of P ions through cell walls and intracellular spaces (Smith 2002). Transport across the plasmalemma is active and requires energy input to maintain the strong electrochemical gradient and 1000 fold increase in internal P concentration. Under P deficient conditions, many species including tomatoes, potatoes, Arabidopsis and barley increase the number or alter the type of transporter proteins present at the root-soil interface, in some cases increasing the rate of P uptake 2-3 fold (Hodge 2004; Smith 2002). There is thought to be two uptake systems in most terrestrial plants, a low and a high affinity system. The low affinity system appears to be constantly expressed and operates between 50-300μM (k_m). By comparison, the high affinity system is de-repressed under P stress conditions with an estimated uptake range of 3-10μM (k_m) (Ramaekers *et al.* 2010; Schachtman *et al.* 1998; Vance *et al.* 2003). Increasing the uptake rate of P may increase the diffusion gradient in the depletion zone, improving the rate of diffusion to the root surface (Horst *et al.* 2001). This may be of particular benefit in high concentration patches such as those surrounding starter fertiliser granules, according to modelled simulations (Caldwell *et al.* 1992; Hodge 2004). Despite these theoretical benefits, there is consensus that the diffusion rate of P remains rate limiting and that morphological responses are more significant for P uptake (Caldwell

et al. 1992; Hodge 2004). A further benefit attributed to physiological adaption for increased P uptake is the rapid response (~3-5 days) and assumed lower carbon cost as compared to architectural adaptions. However, there is evidence to suggest that the energetic expenditure of the up-regulated P uptake mechanism may not be much lower than that of architectural adaptions (Hodge 2004) which have also been observed to be rapid (within ~1 day) (Jackson *et al.* 1989).

A further physiological adaption to P stress is the exudation of various molecules and enzymes from the roots to alter the rhizosphere chemistry and improve P availability. Yang *et al.* (2007) observed increased activity of H-ATPase activity extruding H+ ions from the roots, reducing rhizosphere pH and solubilising P precipitates. In a similar fashion, organic acids such as citrate and malate have been observed in root exudates in response to P stress. These ions function by both solubilising P complexes and by chelating Al, Fe and Ca ions, and provide competition for P sorption sites (Horst *et al.* 2001; Vance *et al.* 2003). Extracellular enzymes such as phytase are also present in exudates and are thought to catalyse P_i release from the organic P fraction (specifically phytate) (Gyaneshwar *et al.* 2002). The release of complex organic molecules from the plant is energetically expensive with some slow growing perennials excreting up to 28% of net photosynthate into the rhizosphere (Schachtman *et al.* 1998). The high rates of chelation, complexation and sorption of all of these organic exudates (previously mentioned as a possible mode of action) result in very low mobilisation efficiencies. Strom *et al.* (2005) observed a 1.9 μM and 0.8μM return of P_i following 10 000 μM applications of citrate and oxalate respectively equating to a 1000 fold molar 'loss' or inefficiency. Similar sorption and microbial degradation of enzyme exudates confine the benefit of exudative mechanisms to local areas of high excretion concentrations such as root apices or proteoid roots (Horst *et al.* 2001; Watt *et al.* 1999). While genetic and selective breeding has been proposed to increase the solubilising capacity of plants, the inefficiencies and photosynthetic cost of such a mechanism is likely to negate the possible productive advantages of increased P acquisition in low P conditions.

2.2.2 Symbiotic

Arbuscular mycorrhizae form symbiotic associations with 70-90% of land plant species, increasing influx of P of the colonised plants 3-5 fold (Ramaekers *et al.* 2010; Schachtman *et al.* 1998). In field studies, early infection of corn plants is estimated to have contributed the equivalent of 7 kg P/ha (Grant *et al.* 2005). The mechanism for this increase in P uptake is increased soil volume exploration (Gyaneshwar *et al.* 2002; Ramaekers *et al.* 2010; Schachtman *et al.* 1998). There is some evidence to suggest that mycorrhizae also have higher affinity uptake mechanisms than that of plants (k_m 2-3μM) however, there is some dispute whether these transporters are associated with P uptake from the soil or for internal transport (Gyaneshwar *et al.* 2002; Schachtman *et al.* 1998). Mycorrhizal symbionts exchange P for a reduced carbon source and as such, in non-P limiting conditions, mycorrhizal infection can reduce productivity (Ramaekers *et al.* 2010). In an excellent review on crop and mycorrhizal interactions, Grant *et al.* (2005) noted that mycorrhizal infection does not guarantee P sufficiency and that fertilisation may still be required for optimum yields. The benefit of mycorrhizal associations is clear and the suggestion has been made that localised root proliferation is redundant when suitable mycorrhizal infection has been achieved (Tibbet 2000). However, when roots and mycorrhizal hyphae are co-located in a high P patch, root proliferation is more significant for P uptake than mycorrhizal pathways (Hodge 2004). This has implications for fertiliser recovery of point source applications.

2.2.3 Morphological -Root architectural adaptions

Soil is heterogeneous at all scales of measurement (Robinson 2005). This is especially the case for immobile nutrients like P, which tends to stratify in the profile and exist in local patches around input sources (e.g. fertilisers, manure or organic material) (Lynch 1995; Lynch *et al.* 2005; Rose *et al.* 2009). Concordantly, root length (proportional to absorptive area) and the spatial placement of that root length determines the P resources available to the plant (Hargreaves *et al.* 2009; Ho *et al.* 2005; Lynch 1995; Lynch *et al.* 2005; Mooney *et al.* 2012). The placement of higher root length density (RLD -root length per volume of soil) in high concentration P patches, improves P foraging and increases P uptake (Hodge 2004; Lynch *et al.* 2005). While substantial inter- and intra-species variation exists in RSA traits, there

are measurable architectural adaptions to P stress conditions. These adaptions occur at two scales within the root system. The first are 'global' (also termed 'constitutive ', 'intrinsic' or 'systemic') adaptions, which affect the characteristics of the whole root system in response to signals originating in the plant shoots or based on the internal P status of the plant. The second are 'localised' (also termed 'plastic', 'extrinsic' or 'response') reactions, which affect a proximate subsection of the root system, often in response to high local nutrient concentrations (Hodge 2004; Lynch *et al.* 2005; Malamy 2005; Robinson 2005). The local responses appear to function within the limits of the global adaptions (such as root to shoot ratio) but alter local distribution of roots to improve P uptake from regions of high availability (Hutchings *et al.* 2004; Robinson 2005). These mechanisms have been shown to increase P acquisition efficiency, in part due to the ability of the root system to adapt to the prevailing conditions.

Breeding crop species for root architectural traits is relatively unexplored (Bengough *et al.* 2006). However, some recent work has demonstrated that genotypes with particular root traits can be well matched to environmental conditions (Henry *et al.* 2010). The heterogeneity of P in the landscape means that no RSA is suited to all environments and the optimum architecture is dependent on the distribution of the required resources. This is especially the case when more than one environmental constraint may be present with competing acquisition strategies. For example, P uptake can be improved with shallow roots while drought tolerance is achieved with a deep root system (Ho *et al.* 2005). Overcoming two or more environmental constraints requires a degree of root system 'plasticity' or 'responsiveness', which must occur at both global and local levels. Root plasticity is a potentially heritable trait (Grossman *et al.* 2012) but selection is hampered by both the opaque nature of soil and the difficulties accompanying measurements in this medium, as well as the need to observe the root system temporally (Gregory *et al.* 2003). As such X-ray CT will be investigated as a possible tool for overcoming these difficulties and is discussed below.

2.2.4 Global root architecture responses to phosphorus nutrition

The ratio of root dry weight to shoot dry weight (R:S) is commonly used to determine the relative allocation of resources to the root system. While this measure varies greatly with genotype and allometry the ratio is maintained within a range. The nutritional status of the plant is one factor that shifts R:S within this range (Robinson 2005). Split root studies amongst many other designs have revealed that the R:S ratio is inversely proportional to the P status of the plant but is not influenced by locally high or low concentration patches of P (Lynch *et al.* 2005; Manske *et al.* 2000; Robinson 1994; Smith 2002). This observation occurs at a global root system level and is generally interpreted as 'exploratory' behaviour where P deficient root systems are allocated greater resources to acquire the limiting nutrient (Ho *et al.* 2005; Ramaekers *et al.* 2010). Similarly, the previously mentioned genotypic variation in R:S also appears to be positively correlated with P acquisition efficiency in wheat (Manske *et al.* 2000; Nielsen *et al.* 2001). Despite the apparent advantages of a proportionally larger root system, the potential benefit may be partially offset by the associated increase in respiratory burden of below ground biomass (Lynch *et al.* 2005). In addition, care should be taken in interpreting the R:S metric, as it is not a direct measure of the absorptive surface of the root system. For these reasons, R:S alone may not be an appropriate selection target for improved P efficiency breeding targets.

In a similar fashion, plant P status is associated with the global redistribution of resources within the root system, altering the architecture and distribution of roots in the soil profile. Particularly in tap rooted species such as Arabidopsis and rape cultivars, low P status has been observed to increase branching density at the expense of primary root extension (Al-Ghazi *et al.* 2003; Ho *et al.* 2005; Linkohr *et al.* 2002; Ramaekers *et al.* 2010; Williamson *et al.* 2001; Yang *et al.* 2007). Many other species have been observed to maintain main axis elongation as well as increase branching density and extension of lateral branch roots in response to P deficiency (Malamy 2005; Ramaekers *et al.* 2010; Zhu *et al.* 2004). Inversely, increases in P uptake resulted in the comparative reduction of branch root density (Lopez-Bucio *et al.* 2002). The perceived benefit is dependent on the characteristic stratification and immobile nature of P. Plants with greater root length in the surface soil have greater P uptake (Lynch 2007). As has been observed in maize, plants that exhibit greater

branching and extension of roots, particularly in the surface soil layers, had greater P foraging capabilities (Lynch 2007; Lynch *et al.* 2005; Ramaekers *et al.* 2010).

The mechanism for initiating the generalised increase in lateral branching and extension has not been determined, however there is some evidence to indicate plant hormones ethylene, auxins and cytokinins may be associated with regulation of this response (Malamy 2005; Vance *et al.* 2003; Williamson *et al.* 2001). In a review on the subject, Malamy (2005) summarises that adding and blocking auxin at the root shoot interface, increases and decreases branching density of roots respectively. Low root tissue auxin levels (associated with higher tissue P) are known to prevent pericycle activation and consequently reduce branch development (Al-Ghazi *et al.* 2003; De Smet *et al.* 2003). To similar effect, brassinosteroids, abscisic acid and nitrous oxide growth regulators are expected to function through the auxin pathway (Malamy 2005). However, the role of auxin in the P starvation response is disputed with some research indicating that the P deficiency responses are independent of auxin, ethylene and abscisic acid (Lopez-Bucio *et al.* 2002; Reymond *et al.* 2006; Ticconi *et al.* 2004). Despite confusion regarding the regulation mechanism, P starvation of the plant has implications for the allocation of resources within the root system favouring branch development and surface soil exploration for improved P uptake.

Root growth angle (also referred to as the gravitropic set-point angle (Rubio *et al.* 2001)) is the vector of root extension relative to gravity. The more horizontal the direction of growth and perpendicular the branching angle the less P depletion zones overlap and shallower soil is more thoroughly explored (Ge *et al.* 2000). Modelling supports the intuitive conclusion that the direction of root growth strongly influences the volume of soil explored and degree of inter-root competition (Ge *et al.* 2000; Hargreaves *et al.* 2009; Rubio *et al.* 2001). With some elegant work, Bonser *et al.* (1996) demonstrated that under P limiting conditions, some genotypes of common bean decreased their growth angle (more horizontal) to increase P foraging near the soil surface. There is suggestion that the regulation of this response may involve ethylene derived from the shoots although there appears to be limited work completed in this area (Malamy 2005). The lack of *in-situ* empirical measures of branching angles and growth vectors also limits root system modelling (Lynch *et al.* 1997).

Since then, Henry *et al.* (2010) have demonstrated the productive advantages of this P stress response in low input, high sorption soils. In particular they demonstrated that specific root system architectural traits, can be selected for the prevailing environmental conditions. However, these assertions are made on the basis of a single limiting factor. As demonstrated by Ho *et al.* (2004), where more than one resource may be limiting, RSA traits may be mutually exclusive. For example, a shallow root system for P foraging may preclude a drought tolerant deep root system. Where multiple resources are likely to be limiting, root system plasticity is likely to be important for optimum productivity. Growth angle adaptation to P status of the plant is a plastic response at a global root system level to tissue P concentration (Bonser *et al.* 1996; Ho *et al.* 2004; Lynch *et al.* 1997).

Root hairs form an important mechanism for P nutrition (Gahoonia *et al.* 1998). They function by increasing the volume of soil explored, extending the depletion zone and are the primary site for P uptake behind the extending root tip (Officer *et al.* 2009). The density and length of root hair development is proportional to the P uptake of the plant, with P deprived plants producing more and longer root hairs (Gahoonia *et al.* 1997; Gahoonia *et al.* 1999; Ramaekers *et al.* 2010; Vance *et al.* 2003; Yang *et al.* 2007). In Arabidopsis, root hairs have been observed to be 5 times more dense and 3 fold longer in P deficient conditions as compared to high P availability (Vance *et al.* 2003). Root hairs are the extension of trichoblast (root epidermal) cells into the rhizosphere and subsequently do not require further cellular division, extension or incur significant metabolic cost (Gahoonia *et al.* 1997). Root hair characteristics correlate well with P uptake efficiency. Amongst the cereal species observed, Gahoonia *et al* (1997, 2001, 2004) noted significant variation in root hair expression. If the substantial heritability quantified in other species (e.g. h^2 =0.33-0.44 white clover) is consistent in cereals, root hair elongation has potential as a beneficial breeding target for improved P uptake (Gahoonia *et al.* 1997; Gahoonia *et al.* 2004; Gahoonia *et al.* 2001). Root hair stimulation may be mediated by ethylene pathways (Vance *et al.* 2003). However, the sensing or trigger mechanism is less clear with some authors interpreting the correlation of root hair extension and P nutrition as a response to internal P concentration, while others attribute the trigger to perception of external P concentration (Gahoonia *et al.* 1997; Grant *et al.* 2001; Lopez-Bucio *et al.* 2003; Lynch *et al.* 2001). The fundamental correlation of P deficiency with low

solution P concentration makes this a complex question to answer. Interestingly, suppression of root hair expression is highly localised in the presence of high external P concentration (Bates *et al.* 2001), supporting the hypothesis that root hair initiation is responsive to local P concentrations. This provides evidence for localised responses to P patches and the associated perception of external solution P concentration (Bates *et al.* 2001). The negative response of root hair length and density to high P availability appears contradictory to that of branching and root length density (discussed in the next section) to the same stimuli. The mechanism for this control and the evolutionary advantage of the response remain unclear but may suggest an unknown liability of root hairs such as increased susceptibility to pathogen attack (Bates *et al.* 2001). It is not within the scope of this review to discuss the possible competitive function of root hair production, however, it is clear root hair regulation provides evidence for root system plasticity, which may function at one or both of the global and localised scales.

2.2.5 Local root architectural responses

Drew (1975) was one of the first to demonstrate the magnitude of localised root proliferation to high nutrient patches. Since then the phenomena has been the subject of many investigations and reviews exploring the response; its regulation, implications for productivity and plant competition (Hodge 2004; Robinson 1994). There is however, a wide range of definitions for the term 'proliferation'. As Hodge (2004) summarises, the term has been applied to a range of root architectural mechanisms such as generalised increases in root allocation (R:S), localised RLD and increased branch length but suggests that the more appropriate definition is the increase in branch root initiation. Branch initiation is potentially more spatially specific than other architectural features and allows for measurement of root system modular responses to a patchy environment.

Localised root proliferation occurs most dramatically in response to high N and P patches, K also appears to have a stimulatory effect, albeit more global (Drew 1975; Robinson 1994). The typical response to heterogeneous distribution of N and P produces an increase in branch initiation in the patch (Drew 1975; Hutchings *et al.* 2004; Lynch 1995; Officer *et al.* 2009). There appears to be some variation in this

response between species, for example, Linkohr *et al.* (2002) reported no detectable increase in branching density but did observe an increase in root length. Although it does not fall within the definition as proposed by Hodge (2004), many authors also describe stimulation of branch extension within the patch (Bonser *et al.* 1996; Drew 1975; Linkohr *et al.* 2002). Regardless, the result is an increase in RLD within the patch for enhanced uptake of nutrients (Hodge 2004). The advantage of local proliferation for immobile nutrient uptake (e.g. P) is clear (although remains unquantified) since RLD is proportional to P uptake (Grabarnik *et al.* 1998; Hodge 2004). The functional advantage for N (being a mobile nutrient) remains less clear given the temporally and spatially transient nature of N distribution in the soil profile (Hutchings *et al.* 2004).

2.2.5.1 Sensing mechanism

The highly localised nature of the proliferation response implies a corresponding sensory mechanism that is relative to external P concentration. There is evidence that the root system has a mechanism allowing root production to be highly sensitive and proportional to the quality of the P patch, especially for clonal species (Hutchings *et al.* 2004; Jackson *et al.* 1989). There is little empirical evidence regarding the trigger mechanism, however, Hodge (2004) suggested that it may be relative to P uptake transport rate while Robinson (2005) inferred that it is likely to be the local cellular nutrient concentration (e.g. cytostolic P or metabolite). It is also thought that the proliferation response is dependent on the global plant P status, whereby plants with sufficient P will not exhibit morphological responses (Hodge 2004; Jackson *et al.* 1989; Ma *et al.* 2008). To determine the trigger mechanism there is first a need to understand the conditions in which the morphological response is present. Robinson (2005) hypothesised that the trigger conditions may be; 1) an absolute concentration of P, 2) a concentration above or below a threshold or 3) P concentration relative to other metabolites in the cell. In addition to these possible triggers, Hutchings *et al.* (2004) observed that patch contrast (the relative difference between the patch quality and the background P availability) also influenced the proportion of the root system allocated within that patch. In this sense, the contrast of the patch against the background may also affect the plants perception of the patch (Hodge 2004). Robinson (1994) also observed that many of the studies using heterogeneous nutrient

distributions have used concentrations well above those observed in the field which may affect these findings. There is some evidence (predominantly from high contrast in-vivo experiments) implicating a role of root cap sensing in RSA responses to high and low concentrations of P (Desnos 2008; Svistoonoff *et al.* 2007; Ticconi *et al.* 2004; Wang *et al.* 2002). Regardless, there are still unanswered questions regarding the specific conditions under which plants perceive and respond to P patches in the soil.

2.2.5.2 Regulation

More work has been completed into the regulation of the root system responses following a trigger, however the mechanism is not well understood (Ma *et al.* 2008). It appears that under high P conditions, branch root development is halted after the meristem is formed (prior to emergence). These cells remain active for some time and are able to emerge and develop into active roots at a later time (Lopez-Bucio *et al.* 2002). Malamy (2005) suggested that in a patchy environment with low P availability, the proportion of primordium to develop into branch roots increased with the higher local P availability. Karthikeyan *et al.* (2007) proposed sugar accumulation in response to P limitation as a possible signalling mechanism. Changes to auxin sensitivity stimulating lateral root formation has also been suggested as a possible control mechanism, however, as with auxin involvement in global control mechanisms this is also debated (Ramaekers *et al.* 2010). The role of a broader regulatory mechanism is implied by the regular reports of localised proliferation at the cost of root growth outside the patch (Hodge 2004; Linkohr *et al.* 2002; Ma *et al.* 2008; Robinson 1994). Linkohr *et al.* (2002) interpreted the observation as an active suppression of root growth outside the band which would imply a co-ordinated regulatory response independent of external P availability. It may simply be the result of a fixed R:S and increased allocation of resources to the high P patch (Robinson 1994), representing an active response to the high P zone and a consequential passive decrease in allocation of C to regions outside the band. Further research is required to understand both the trigger and regulation mechanisms for the localised proliferation response.

2.2.5.3 Net benefit

Given the clear relationship between RLD and P uptake, the effect of local plasticity for acquiring P from regions of high availability has clear implications for improved acquisition efficiency (Hutchings *et al.* 2004). The net benefit of the proliferation response is hard to quantify and depends on the size and quality of the patch, the quality of the background soil, the nutrient in question and the extent and intensity of the proliferation response of the plant (i.e. cost of plant resources)(Hodge 2004). Despite this, many authors have reported advantages associated with patch exploitation both in terms of nutrient uptake and competitive advantage (Grossman *et al.* 2012; Hodge 2004; Hutchings *et al.* 2004; Jackson *et al.* 1996).

However, local proliferation is not necessarily advantageous. Recently, Grossman *et al.* (2012) observed that local plasticity was only beneficial in low P conditions. This observation is unsurprising as the response is unlikely to be present under high P availability (Hodge 2004). Lynch (2005) suggested that the species variation commonly observed in the proliferation response may imply evolutionary trade-offs; plants in a competitive and patchy environment may benefit, while plants in a less competitive or homogeneous environment would be disadvantaged. However, it is equally likely that species that fail to exhibit proliferation responses may in-fact have lower P requirements (by increased acquisition or utilisation efficiency) rather than an inability to respond locally (Robinson 1994). The net benefit of localised proliferation could also be reduced if there was a disproportionally large morphological response to a small scale patch, reducing the resources available for the remainder of the root system and soil volume exploration (Hutchings *et al.* 2004). Therefore, the location of the morphological response inside the high P patch is important for P acquisition efficiency (high P uptake for low C expenditure).

Due in part, to the challenges of observing root system behaviour *in-situ*, the specificity of the proliferation response to P patches has not been quantified. The development of a method to measure and quantify how spatially accurately genotypes allocate resources to a high P patch, may enable localised plasticity to be included as a breeding target. The intention would be to breed cropping varieties with improved P sensing and morphological response mechanisms that produce high RLD in concentrated P patches. For cropping systems that currently apply P fertilisers,

particularly in bands, this mechanism would potentially improve the currently low recovery of phosphatic fertilisers.

2.3 X-ray Computed Tomography

Root systems remain difficult to observe *in-situ* as they are occluded by soil -an opaque and highly heterogeneous matrix (Lynch 1995). Understandably then, the vast history of plant breeding and research has focussed on the above ground portion of the plant (Ingram *et al.* 2012). Root system research has progressed on the back of many innovative and successful methods, many of which are labour intensive, time consuming and prone to some level of artefacts (Gregory 2006). Three-dimensional, high-throughput methods offer opportunity to measure and characterise root system architecture in almost unprecedented detail with different, if not less, of these artefacts. X-ray Computed Tomography (CT) has been recognised for some time as having potential application to root system studies but until recently, the technology has been in its infancy. With increasing market pressure from the medical and engineering industries, X-ray CT has become a more practical tool with faster acquisition, processing, data handling and access to this level of technology, which have been key restrictions in the past (Mooney 2002; Mooney *et al.* 2012). There remain significant challenges to the implementation of X-ray CT for root studies but current research in this and adjoining fields provides opportunity for rapid development in the near future. It is expected that high throughput root system phenotyping will be a reality (Mooney *et al.* 2012). Direct measurement and improvement of the global and local plasticity of the RSA would become possible and are likely to improve plant nutrient acquisition efficiency and productivity (Ingram *et al.* 2012).

The objective of applying X-ray CT to characterising biotic features within the soil is to non-destructively image a field relevant soil sample and spatially analyse the form and distribution of the solid, water, biotic and air components. By nature, imaging and distinguishing between similarly low attenuating substances inside a dense heterogeneous substance is challenging but the technique has been widely recognised to have significant potential to measure soil properties inside an otherwise opaque and complex medium (Gregory *et al.* 2003; Young *et al.* 2004). Often methods for

measuring and appreciating biotic features within soil are destructive and characteristics such as root systems or earthworm burrows must be washed out, excavated or filled with a fixative and thin sectioned for effective measurement (Capowiez *et al.* 1998; Gregory 2006). These measures are generally labour intensive and preclude any further investigations using the same sample. One of the attributes of CT is the ability to non-destructively and therefore repeatedly measure the same sample in time, allowing *in-situ* measurements of biotic characteristics as they respond to changing conditions (Gregory 2006; Tracy *et al.* 2011). Furthermore, the spatial nature of CT allows precise 3-D measurement of feature arrangement *in situ*, which is absent from many other soil analysis techniques. For example, root architectural and pore space structural characteristics such as branching or liquid contact angles, tortuosity and fractal dimensions can be precisely measured and modelled (Crawford *et al.* 2012; Gregory *et al.* 2003; Lontoc-Roy *et al.* 2006) without the need to extrapolate from 2D measurements.

2.3.1 Basic tomographic principle

The development of X-ray CT is generally attributed to Hounsfield (1973) and since its initial application to the medical field it has been implemented in many disciplines. At its most basic, X-ray CT provides a 3D non-destructive digital representation of an object, differentiating phases based on their varying attenuation of X-rays. The technology with particular application to soil science has been thoroughly reviewed and the reader is directed to Wildenschild *et al.* (2002), Mees *et al.* (2003), Mooney *et al.* (2012),Taina *et al.* (2008) and Anderson *et al.* (1992) for a more exhaustive explanation of the technology.

X-ray tomographs are produced by placing a sample between an X-ray source and a digital detector that is sensitive to X-rays (Figure 2.2). As the X-rays pass through the object they are differentially attenuated by the materials in the object. This radiograph forms a single 'projection' where pixel values are relative to the cumulative density of any one trajectory through the sample. The object is then rotated through 360° with projections acquired at regular intervals and the resulting images are reconstructed into a 3D tomograph, typically using a backprojection algorithm. The tomograph is

often represented by a series of 2D slices where voxel (a 3D pixel) values represent the average attenuation for each discretised unit of the sample.

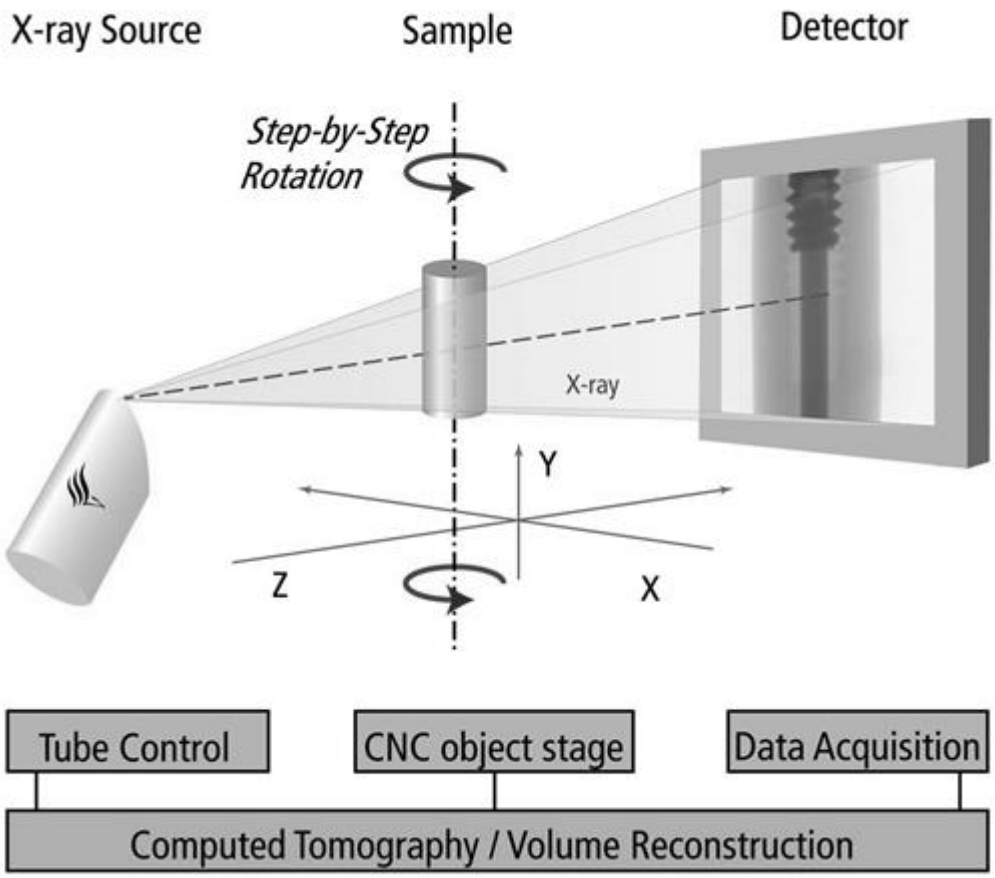

Figure 2.2| A basic schematic for the computed tomography process. The source (left) produces a cone X-ray beam, the sample (centre) is placed between the source and detector, producing a radiographic projection. The sample is rotated through 360 degrees creating a series of projections, which can be reconstructed into a 3D tomograph using specialised software. Image reproduced from Phoenix (2009)

2.3.2 X-ray source

The X-rays used for CT are typically produced by the deceleration of a high velocity electron beam in a highly evacuated atmosphere. In the case of Synchrotron radiation, electrons are spiralled in the circular magnetic field of a particle accelerator. Where the electron beam is redirected by bending magnets (or similar apparatus) a bright beam of radiation is produced at a tangent to the circle. Synchrotron radiation has a very high photon density and can therefore be collimated and mono-chromated into a parallel beam of a single wavelength while maintaining sufficient flux for imaging (Wildenschild *et al.* 2002). In laboratory-based systems, electrons are accelerated

towards a metal (typically tungsten) target where deceleration produces the X-ray beam. The resultant beam is the product of two processes; firstly, 'Bremsstrahlung' radiation (German for 'breaking') is produced by deceleration of the electrons and yields a wide range of beam energies. The target itself attenuates the low energy portion of the beam. Secondly, electrons in the target material are knocked out by the incoming electron beam and emit a 'characteristic' wavelength of X-ray energy as electrons fall from a higher excitation state to the K-shell. Consequently, combined spectrum of X-rays is polychromatic in nature (Cnudde 2005; Wildenschild *et al.* 2002). Laboratory systems have a low X-ray yield (~1-1.5% X-ray, ~99% heat energy) and produce a polychromatic divergent X-ray beam. The initial voltage applied to the heated filament to produce the electron beam (typically in the kV range) determines the velocity of the electrons in the beam and corresponds to the wavelength of X-rays produced (higher kV produces higher energy (shorter wavelength) X-rays). The amperage applied to the filament corresponds to the number of electrons in the electron beam and subsequently the number of photons (or flux) of X-rays produced.

2.3.3 Interaction with sample

As X-rays pass through an object, some interact with the material attenuating the beam of X-rays. The emergent beam is the result of the cumulative attenuation of the materials in the sample. Lambert-Beer's law describes this relationship for a monochromatic X-ray beam (Mooney *et al.* 2012; Taina *et al.* 2008; Wildenschild *et al.* 2002). The attenuation of X-rays is predominantly caused by the absorption and scattering of X-rays. Photoelectric absorption (dominant for X-rays below 100keV) is where the X-ray photon energy is entirely absorbed by atomic electrons in the sample, ejecting the so-called photoelectron. This effect is relative to the atomic number of the sample. Crompton scattering becomes dominant for X-rays above 100keV in energy (Mees *et al.* 2003). It occurs where the incident X-ray photons interact with electrons, producing incomplete absorption of the photon, producing scattered lower energy photons. Crompton scattering is proportional to the electron density of the sample. The product of Crompton scattering and photoelectric absorption for any one path through the sample provides the attenuation values observed by the detector (Mees *et al.* 2003; Wildenschild *et al.* 2002). In this way the different materials can produce

similar attenuation values. This can be circumvented with dual energy scanning. For further information please refer to Wildenschild *et al.* (2002).

2.3.4 Detection and reconstruction

Modern digital X-ray detectors take advantage of the capacity of X-rays to ionise fluorescent compounds. A high-resolution scintillator is typically placed in-front of a visible light Charge Coupled Device effectively converting X-ray radiation into visible light and then electronic signals (Wildenschild *et al.* 2002). The technology for X-ray detectors has progressed rapidly with many sizes, pixel densities and various forms of scintillation. This results in a wide gamut of detectors with differing resolutions, sensitivities, achievable contrast and acquisition times but these will not be discussed here.

In both laboratory based and synchrotron CT facilities the sample is rotated between the source and detector, while in medical facilities the source and detector rotate around the sample (Mooney *et al.* 2012). Radiographs are acquired from a number of equidistant angles (typically requiring more than $(\pi/2)$ x number of pixels representing the sample diameter) as the sample is rotated through a complete revolution. The resulting projections are used to calculate the average attenuation for each voxel in the sample (Wildenschild *et al.* 2002). This is a computationally intensive process and a number of algorithms have been developed to calculate the tomographs (largely dependent on the characteristics of the beam –cone or collimated) however, most laboratory reconstructions are based on filtered back projection (e.g. Feldcamp *et al.* (1984)). Due to the difficulties in observing 3 dimensions simultaneously, tomographs are typically represented by a series of grey scale 2D thin sections that are termed 'slices' (Mooney *et al.* 2012). The orientation of these slices is arbitrary and can be adjusted easily. One of the fundamental challenges of CT is that the process discretises the sample (which is spatially continuous) into discrete and averaged units, the size of which is determined by the resolution of the system. This means that abrupt phase boundaries in the sample are reduced to gradual and indistinct edges and is commonly referred to as the 'partial volume effect'. This and other limitations of the technique will be discussed in greater detail below.

2.4 Visualisation and characterisation of biotic soil characteristics

2.5.6 Application of phase contrast systems in soil research

2.6 Conclusion

Phosphorus continues to be one of the dominant macronutrient deficiencies impacting the productive capacity of global agriculture. Compounded by the non-renewable nature of the primary ameliorant (rock phosphate products) and increasing demand for

agricultural products by a burgeoning global population, significant improvements in PUE are necessary. The highly reactive nature of P renders it immobile and distributes it heterogeneously in soil. Plants have adapted to this common environmental feature, demonstrating root system plasticity with both localised and global root system architectural responses to enhance nutrient capture from patches of P. These responses by nature improve the uptake of P from local patches and represent a prevalent plant adaption that could be enhanced to improve fertiliser use efficiency from banded applications of P. Despite the potential importance of these RSA traits to improve fertiliser use efficiency, there is a dearth of information regarding the spatial specificity of the response and its regulation. This is largely due to the limitations of methodologies that enable high spatial resolution of root architectural traits.

Selection of crop variants with improved RSA or localised responses requires a spatially referenced technique, capable of identifying root system distribution and traits from within soil or soil-like media. Given the complex chemical, physical and microbial interactions present in soil, coupled with its electron dense and opaque nature, a technique that can image through soil would be preferable for producing field relevant results. X-ray CT is perhaps the most likely method and has been identified as such for some time. Recent advancements in instrument design and computer technologies have circumvented some of the previous limitations of the technique, bringing it to the precipice of practical implementation in root system studies. The spatial and non-destructive nature of X-ray CT provides an ideal method for analysing the localised morphological responses of the root system to a highly immobile resource such as P.

There is substantial work required to develop X-ray CT into a technique capable of rapid high-throughput analysis of root systems. As yet there is no established robust segmentation method capable of automatically extracting root systems from tomographs. Once a suitable methodology has been established, the spatial distribution of the localised proliferation response can be quantified. Given the high spatial precision of the root system response under artificial conditions (e.g. solution culture) it is expected that the response in the soil medium will be comparably localised. Establishment of such a method will not only allow screening for possible

genetic variation in RSA, but also allow possible trigger conditions and regulation mechanisms to be tested in a realistic edaphic environment. The following chapters will detail the development of X-ray CT and processing methods for root system analysis and apply the technique to understanding the architectural adaptions to wheat root systems.

Chapter 3 : Experimental Optimisation

The technological parameters used to build and operate laboratory CT systems have significant influence on the quality and characteristics of the resulting imagery. Identifying optimal settings is a dynamic process with alterations in a single parameter influencing the ideal value for many of the others. The optimal parameters for any one scan are highly dependent on the sample (size, density and shape) and the purpose of the scans. For example, some settings will provide good contrast between similarly attenuating substances, where other settings will provide sharper phase boundaries between phases with disparate attenuation coefficients. This chapter will seek to identify and quantify the influence some of the major adjustable parameters have on image acquisition as well as justify the parameters used in the following experimentation. I will also discuss strategies to reduce the impact of common imaging artefacts with particular relevance to the GE Phoenix V|tome|xs system used for these studies.

3.1 The University of New England X-ray Micro CT scanner

The UNE Micro-CT scanner is the V|tome|xs and was built by General Electric Phoenix in 2010 (Figure 3.1 -Left). It has two 'serviceable' and interchangeable X-ray sources (Figure 3.1 -Right). The first (GE XS 240D), a 240kV (320 W) 'direct' source in which an electron beam is accelerated onto a tungsten target and X-rays are reflected from the 4μm focal spot (pictured at the top of Figure 3.1 -Right). The target is water-cooled and the X-rays generated pass through a beryllium window to form a polychromatic, divergent cone beam. The second source (GE XS180NF) is a 180kV, 20W tube with a transmission target (pictured at the bottom of Figure 3.1 -Right). In this tube, the electron beam can be selectively focused to 4, 2, 1.5 and 1μm spot sizes onto a thin tungsten or molybdenum (exchangeable) target. The X-rays are emitted from the reverse side of the target making it possible to move a small sample much closer to the source. While limited to lower energies, this tube is capable of achieving higher resolution images of small samples. Large or highly attenuating samples are generally scanned using the direct 240kV tube, as a wider range of energies can be used without damage to the target.

Figure 3.1| (Left) The University of New England V|tomex|s Micro CT cabinet manufactured in 2010 by General Electric Phoenix. (Right) The V|tomex|s interchangeable X-ray sources (pictured in yellow) with the 'direct' tube in position (top most tube) picture captured during a scan of 28 day old wheal plant in white PVC tube, mounted in grey PVC mounting on the CNC manipulator.

The detector is 512 x 512 pixel amorphous-silicon diode array with Lanex® scintillation foil. The thin Gadox scintillator and relatively 'large' pixel size allow fast image acquisition times (up to 7 fps) with low noise. It is a 16- bit detector with overall dimensions 204.8mm x 204.8 mm (pixel size 400µm x 400µm) allowing a maximum sample size of 120mm diameter to be scanned at ~230µm voxel size. The system has a maximum resolution of approx. 2µm voxel size. In its current configuration, the distance between the source and detector is fixed and as such different levels of magnification can be achieved by altering the sample to source distance. The sample manipulator is a high precision 5-axis motorised Computer Numeric Control (CNC) stage. The system is designed for rapidly scanning a diverse range of sample types and resolutions with streamlined data handling to reconstruct volumes using a GPU computing cluster. Reconstruction time approx. 30 sec (for a 512 x 512 x 512 voxel volume based on 1250 projections).

3.2 Sample Size and resolution

One of the major limitations in the application of X-ray CT to soil science is the physical constraints on the range of achievable resolutions (Heeraman *et al.* 1997; Taina *et al.* 2008). Given the magnitude of heterogeneity observed in soil, field applicability requires large sample sizes, yet small-scale features govern functionality, hence very high resolution is required. This is especially true for root studies as large pot sizes are required for optimal plant growth, yet the finest fraction of the root system makes the largest contribution to function (Hargreaves *et al.* 2009; Mooney *et al.* 2012). Spatial resolution in CT scans is not given by the voxel dimensions but is the level of features that can be resolved or distinguished. It is commonly defined as the minimum separation distance required to distinguish two objects as separate (Wildenschild *et al.* 2002). It is therefore determined by factors that effect the voxel size and the noise in the image, such as the X-ray source type and spot size, magnification, signal to noise ratio and the detector size, density and sensitivity (Wildenschild *et al.* 2002). In general, the spatial resolution is considered to be at least 2-4 times the voxel size (Kaestner *et al.* 2006).

In laboratory cone-beam systems, voxel size is determined by the magnification factor and the detector size and pixel density. Magnification is relative to the source to sample distance and the propagation distance between the sample and the detector. The closer the sample to the source and the longer the propagation distance the greater magnification is achieved. The size of the detector determines how much magnification can be achieved as the projection must fit across the detector (Cnudde 2005). The pixel density (or the size and number of the pixels) on the detector determines how many units the sample is discretised into. The larger the number of pixels in the detector array, the more segments the projection is divided into, resulting in higher resolution tomographs upon reconstruction. Image resolution and contrast sensitivity are inextricably linked. Each pixel on higher resolution detectors represent a smaller collection area and therefore require higher flux (photon density) or longer integration times to achieve sufficiently high counting statistics (Wildenschild *et al.* 2002).

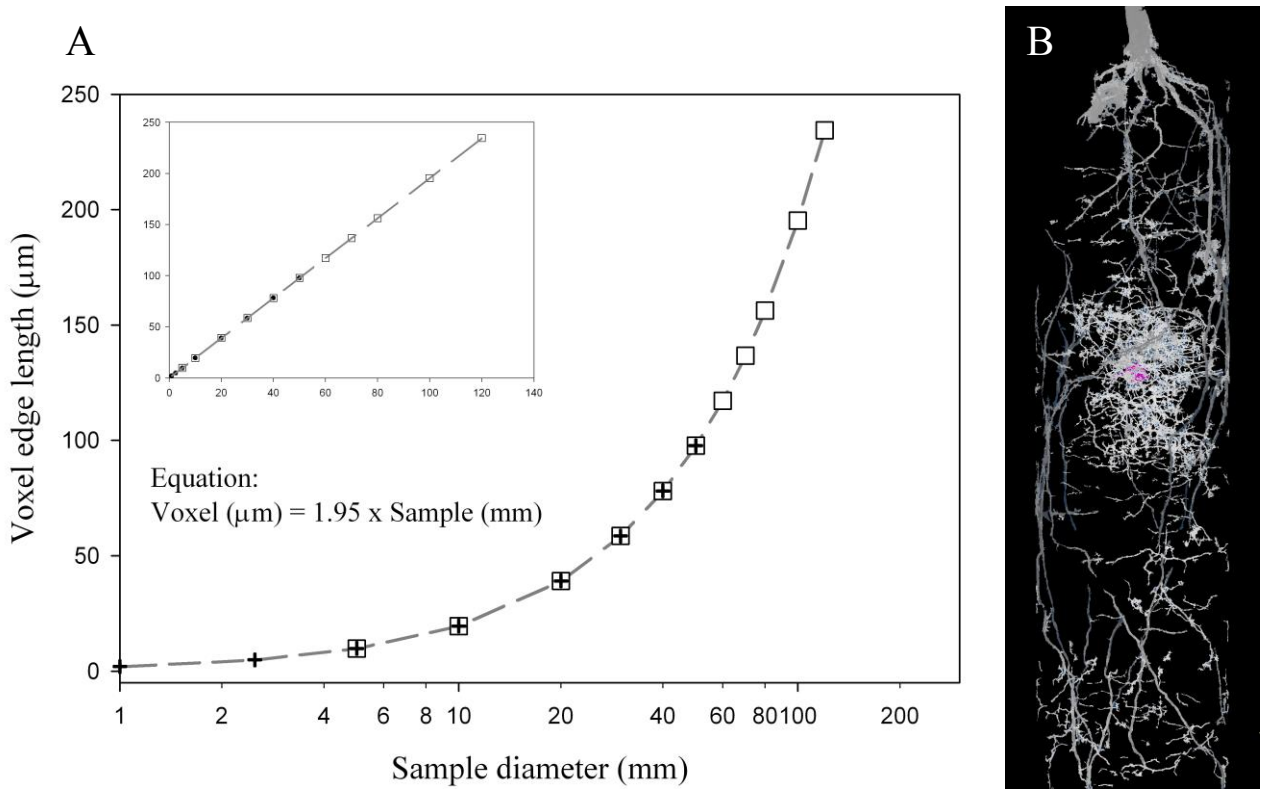

Figure 3.2| (A) There is a linear relationship between the sample diameter and smallest possible isotropic voxel side-length. Inset is using linear axis, while the log-linear axis highlights the possible range of the different sources types - 'Transmission' tube (crosses), 'Direct' tube (squares). (B) 3D tomographic representation of Triticale root system (white) 20DAS in response to Di-Ammonium Phosphate granule (pink).

With a constant detector, source and propagation distance, as in laboratory systems, there is a rigid relationship between the sample diameter and the achievable resolution (Figure 3.2A). The GE Phoenix V|tome|xs in its current configuration has a 512 x 512 pixel detector array with 0.4mm x 0.4mm pixel size (overall detector size 204.8 mm). Assuming that adequate sample penetration is possible within the energy capabilities of the tube, this configuration limits the largest sample to 120mm diameter (corresponding voxel size 235µm). The 'Direct' X-ray source has a spot size of 4µm limiting its achievable resolution to approx. 10µm (5mm sample diameter). The 'transmission' source is capable of producing spot sizes of 4, 2, 1.5 and 1µm which allows voxel sizes down to ~2µm. However, at higher resolutions (and smaller spot sizes) the total energy settings possible are restricted as target damage occurs when high energy is concentrated into a tightly focused beam. As a result the maximum sample diameter is approx. 50mm (97µm voxel size) with the samples to <1mm

(~2μm voxel size) scannable at low range. The smallest voxel size achievable for a given sample (assuming all of the sample must be scanned) is represented in Figure 3.2A and given by:

$$Voxel\ size\ \mu m = \frac{Sample\ diameter\ (\mu m)}{Number\ of\ pixels} = 1.95 \times Sample\ diameter\ (mm)$$

Where the number of pixels is 512 in the current configuration. The voxel size decreases (higher resolution) as the diameter of the sample decreases with the absolute maximum resolution determined when the sample contacts the source (Tippkotter *et al.* 2009). In traditional CT, the sample must be kept within the field of view (Cnudde 2005), however, recently algorithms have been developed for Region of Interest (ROI) scans where a subsample of the object can be scanned at a higher resolution (Carminati *et al.* 2009). The same relationship between diameter and resolution holds true for this method but there is an associated loss in image quality.

In a small pilot study, 6 polyvinyl chloride (PVC) tubes with 3 pot diameters (30, 65 and 100mm) were filled with vertosol soil that had been dried and crushed to <2mm aggregate size. A single di-ammonium phosphate (DAP) granule was placed 50mm below the surface and two triticale seeds were planted at a depth of 15mm. Following germination the plants were grown for 20 days under temperate glasshouse conditions. The tubes were scanned at the maximal resolution for the respective pot sizes (67, 127 and 195 μm) with energy settings appropriate to the sample. For Figure 3.2B the scan parameters used for the direct tube source were 180kV, 200μA with a 0.5 mm Cu attenuation filter. The projections were the average of 3 images captured after an integration time of 200ms and 1000 projections were recorded in the full revolution. The complete volume was the result of 4 vertically adjacent scans with the total scan time taking 45 mins. By comparing the quality and resolution of the scans mentioned above, it was determined that the 30mm diameter PVC pots (Figure 3.2) were most appropriate of the pots tested at they allowed the resolution of roots greater than 140μm (voxel size ~68μm) which notably contribute significantly to the proliferation response. The local proliferation response to a DAP granule was observed at this scale confirming the ability to detect root morphological adaptations.

Later experiments confirmed that an average 3% of the measured root length (using WinRhizo) had a diameter below 140µm and was therefore undetectable at the spatial resolution achievable using the 30mm pots.

To improve the time taken to change samples and ensure that the sample is well centred for maximal resolution, sample mounts were manufactured from PVC plastic (Figure 3.3). The mounts ensured that the tubes (250mm high x 30mm diameter -extruded PVC) were easily placed in the self-centring 3-jaw manipulator chuck. Previously, when the base of the pot was not cut precisely perpendicular to the sides or soil particles obscured the pot seating against the chuck, the top of the pot rotated off-centre. Small deviations caused the pot to pass outside the field of view and data was therefore not captured. Correction of this problem was either by 'trial and error' and time intensive or involved reducing the resolution of all scans to ensure the sample remained within the field of view. The sample mounts improved the repeatability and speed of sample mounting in the CT manipulator chuck.

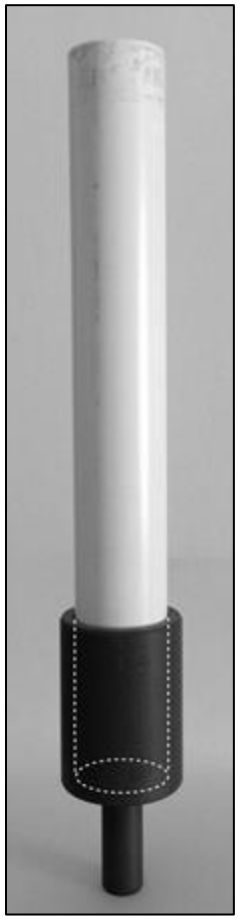

Figure 3.3| Poly-Vinyl Chloride pot (white) with Grey PVC sample mount.

3.3 Energy settings

3.3.1 Voltage (kV) and Amperage (µA)

The most appropriate energy settings for any sample are highly dependent on that samples cumulative attenuation and have a large bearing on the quality and contrast of the resulting imagery. In general, energy settings are chosen to provide adequate signal to noise ratio with scan time being the common trade off (Cnudde 2005). One of the first parameters to select is the kV. This is similar to but not the same as keV used in synchrotron apparatus. Where keV represents the energy of a single wavelength, in laboratory systems, a voltage (kV) potential is applied to filament producing a beam of electrons, which are accelerated into the target. The higher the voltage applied, the higher the average energy of the polychromatic beam produced. In this sense, keV and kV are proportional but not congruent. The kV required is generally proportional to the density of the material. Higher density materials have a

higher attenuation coefficient and require higher energy photons to penetrate the sample. If high kV parameters are used for low-density materials, the object becomes transparent and the contrast between phases in the material is negligible. The converse is also true, if low kV is used on high-density objects, there is insufficient penetration for adequate counting statistics. The signal to noise ratio decreases meaning the contribution of electrical noise to the image is relatively greater (Cnudde 2005; Heeraman *et al.* 1997; Wildenschild *et al.* 2002). The amperage (typically μA, sometimes mA in medical scanners) applied to the tube represents the flow of electrons across the filament; the greater the μA, the larger the number of electrons accelerated and the higher the intensity, brightness or flux of the X-ray beam generated (Cnudde 2005). In this capacity the μA parameter also determines the signal to noise ratio where a low μA would yield inadequate counting statistics, while extreme μA would lead to detector saturation and a decrease in contrast. It is difficult to specify clear guidelines in setting these parameters and it can depend on the purpose of the analysis. It is however clear that the kV and μA selected influences the spectrum and flux of the X-ray beam generated and has implications for the quality of the images acquired.

For the following studies, a matrix of settings were trialled to determine those most appropriate for the experimental setup. The optimal parameters were determined using a real-time grey scale histogram from the detector (corrected for offset and gain), therefore data at inappropriate settings was not recorded. Firstly, appropriate penetration was determined (by adjusting kV), then flux (μA) and exposure interval were adjusted to utilise the maximal dynamic range of the detector while maintaining practical scan times. Having treatments of equivalent composition, consistent settings were applied to all replicates.

3.3.2 Acquisition time

A further parameter that influences the energy settings selected is the acquisition or integration time. A low signal to noise ratio can be improved by increasing the sampling time for each image (effectively improving the sample size or magnitude of counting statistics) (Cnudde 2005; Wildenschild *et al.* 2002). This can have the advantage of improving image quality where sub-optimal energy settings are used due to tube constraints (e.g. energy limitations, overheating and target damage) but it also increases scan time dramatically. Where excessive exposure time is implemented it can also lead to detector saturation, in which case the energy parameters (or integration time) should be adjusted down accordingly (Cnudde 2005; Wildenschild *et al.* 2002).

3.3.3 Attenuating filters

Where highly attenuating objects are scanned, there is often a large discrepancy between the total energy of penetrating radiation and 'free rays'. This phenomenon causes significant beam hardening artefacts (further discussed in section 3.6.2) and low contrast. One way to compensate is to pre- or post-harden the X-ray beam using an attenuating copper, tin, brass or aluminium filter (Cnudde 2005; Wildenschild *et al.* 2002). The filter is placed before or after the object (for pre- and post-hardening respectively) and absorbs the low energy fraction of the spectrum. This reduces the discrepancy between free and attenuated X-rays and makes the beam 'more mono-chromatic' in nature. The best way to avoid this problem is to use a mono-chromatic source but synchrotrons are often limited to approx. 50keV in energy and therefore the size and density of the scanned samples is limited (Wildenschild *et al.* 2002). Filters reduce the range of energies transmitted to the detector (by removing the low energy fraction) and therefore, reduce the spread of grey scale values observed within a substance. To demonstrate the effect of filtering the incident beam, a dry ferrosol soil was placed in a 30mm PVC tube and scanned with no filter, one and two 0.125mm Cu filters. Other scan parameters were 180kV, 120 μA, voxel size was 68.7 μm, exposure time 200ms, 1250 projections in fast scan mode using the 240kV direct tube. The grey values for a uniform subsection of the PVC tube was sampled in the same location for each pot. The histogram was then corrected to align the peak values which were influenced by beam hardening (beam hardening biased the peak values of

No Cu>1Cu>2Cu filters). Filtering the beam produces peaks with a lower variance in uniform substances (Figure 3.4). It was also apparent that a single Cu filter had a comparable effect to the two Cu filters (Figure 3.4).

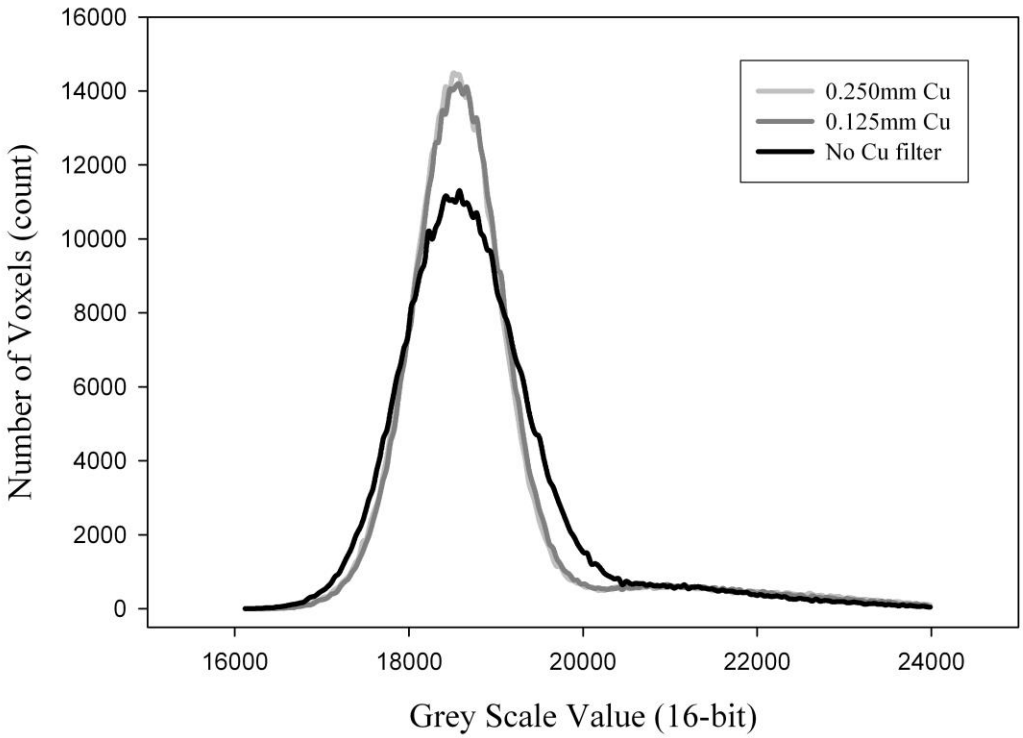

Figure 3.4| Histogram of the observed grey-scale (16-bit) values for a consistent section of PVC pot when scanned with no x-ray beam filtering (black), 0.125mm (dark grey) and 0.25mm Cu attenuation filters (light grey). The histogram peak was aligned to compensate for greater beam hardening effects with the no-filter and 0.125mm filter samples, which translated the histogram positively along the x-axis.

Using filters to reduce the range of grey scale values observed can increase the separation of phases- particularly between low and highly attenuating substances, but also reduces the contrast observed between similarly low attenuating substances (such as organic matter and roots). Therefore, the following experiments used a single Cu filter on the incident beam (copper foil 0.125mm thick) to image root systems as this provided the best compromise for reduced beam hardening artefacts, improved definition between roots and soil while maintaining adequate contrast between pores and roots.

3.4 Image contrast

Image contrast has been identified as another major restriction to the development of X-ray CT for soil science (Taina *et al.* 2008). Contrast refers to how well features can be distinguished from their background and is quantified by the equation:

$$\text{Contrast} = \frac{(Af - Ab)}{Ab}$$

Where Af is the attenuation of the feature and Ab the attenuation of the background (Wildenschild *et al.* 2002). Soil is extremely heterogeneous and produces a wide range of grey values when imaged. Hence it is difficult to isolate features from such a variable background. Contrast is specific to the sample and dependent on the spectrum of X-rays produced, the use of filters and the method for acquiring images (e.g. integration time). One of the largest impediments to root research using X-ray CT is the ability to segment the root system from other phases. Soil and air phases can be well delineated however water, organic matter and roots all attenuate X-rays to a similar extent midway between the soil and air phases making segmentation challenging (Taina *et al.* 2008). Parameters that allow greater contrast between similarly attenuating low absorption phases are preferable for root research.

While controlled by the previously discussed factors (i.e. kV, μA and filters), maximal contrast is achieved by spreading the range of attenuation values observed as much as possible across the dynamic range of the detector (Cnudde 2005). The dynamic range of the detector lies in the region above the electronic noise of the CCD and below the point of saturation. In many modern systems the response is approximately linear within this range. Multiple energy flat field (gain) calibrations can be used to correct for any non-linearity but it was deemed unnecessary for the research contained in this thesis. In general, lower kV, higher μA and minimal attenuation filters produce better contrast between the air, organic matter and soil components but sample penetration is still necessary (Heeraman *et al.* 1997; Wildenschild *et al.* 2002). As with energy optimisation, the conditions to produce the greatest contrast were determined by running through a matrix of settings and observing the real time detector histogram (data not presented).

In addition to the aforementioned parameters, the target material used in X-ray generation can alter the spectrum of X-rays produced, with consequences for contrast.

Tungsten targets are commonly used in laboratory CT tubes as they produce a sharply defined X-ray emission peak (small range of wavelengths) and because tungsten has a very high melting point and is less susceptible to degradation. Alternatively, molybdenum can be used, particularly in low energy tubes. Molybdenum has a lower melting point than tungsten and cannot withstand high energies but produces a broader spectrum of X-rays when compared with tungsten (Mooney *et al.* 2012). For low attenuation substances this can provide additional contrast. Molybdenum targets have less relevance for large, highly attenuating soil cores.

In soil physical research using CT with soil, water and air phases, dopants (e.g. KI, NaI or $CaBr_2$) have been used to increase phase contrast (Carlson 2006; Taina *et al.* 2008). However, with more modern detectors and increased dynamic range dopants are less necessary (Mees *et al.* 2003; Mooney 2002; Tippkotter *et al.* 2009). The use of dopants is also inappropriate where phytotoxic effects or changes in solution behaviour (e.g. altered surface tension) may confound results.

3.5 Scan Time

In general, many of the CT soil studies have been limited to small experiments with low replication (Mooney *et al.* 2012). This is, in part, due to the previously long acquisition times limiting the number of scans to <10 scans per day (Gregory *et al.* 2009). Hence, Hargreaves *et al.* (2009) suggested that root studies using the technique will be limited to small, low throughput studies for the next 5 years. Improvements in detector sensitivity coupled with more efficient and higher energy X-ray sources are resulting in faster scan times. In addition to the advances in hardware, the advent of constant rotation CT has produced substantial gains in scan time with reports of 4 to 20min scans (Flavel *et al.* 2012; Tracy *et al.* 2012). Whilst conventional CT stops the sample at every projection angle and then acquires the image (or averaged images) constant rotation CT acquires a single image projection (no image averaging) while the sample is slowly moving. The advantage of the fast scan protocol was quantified by timing the duration of a series of scans with increasing numbers of projections. The data presented (Figure 3.5) is the result of 200ms integration time where the standard CT protocol averaged 3 images and

discarded one at each projection, while the constant rotation CT recorded a single image at each projection angle. Constant rotation CT has significant benefits for scan speed (Figure 3.5) but does reduce image quality when using comparable projection angles.

Losses in image quality are the result of both image blurring (as the object is moving when the images are acquired) and the absence of multiple image averaging. In conventional CT, each projection is often the average of a number of images. Increasing the number of images averaged at each projection angle improves the signal to noise ratio (Cnudde 2005) with limited gains above 4 images (using the current system). Constant rotation CT records a single image at each projection angle. Increasing the number of projections can improve the image quality but proportionally increases scan and reconstruction time (Cnudde 2005). Current technology allows for highly hardware optimised, fast reconstructions, such that increasing projection number does not have a significant effect on processing time.

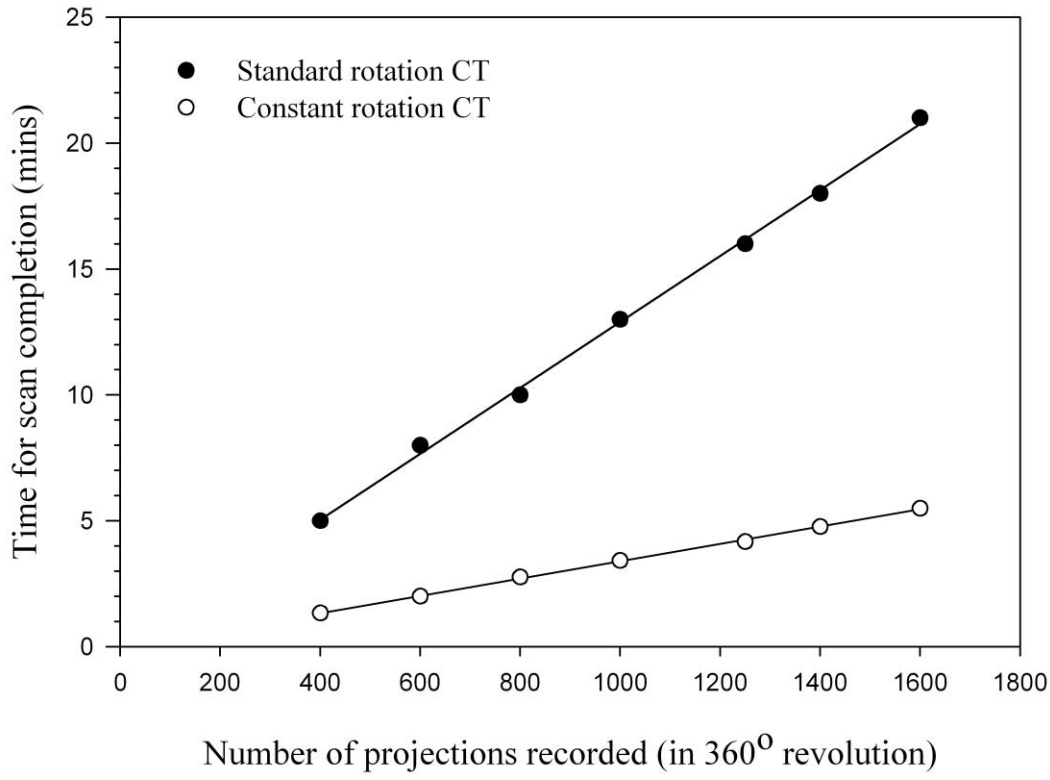

Figure 3.5| Demonstrating the relationship between the scan duration and the number of projections acquired in a 360 degree rotation. Solid circles indicate standard CT where 3 images were averaged at each projection angle and a single image was discarded between steps. Open circles represent constant rotation CT where a single image is acquired at each projection step and the sample rotation is not halted at each step.

For constant rotation CT, increasing the number of projections can compensate for the lack of image averaging at each step with relatively little effect on scan time (Figure 3.5). In general the number of projections required for adequate quality CT is given by:

$$minimum\ projection\ number\ = \frac{\pi}{2} \times\ pixel\ width$$

Where the pixel width represents the number of pixels the sample covers on the detector in the horizontal plane (or perpendicular to the axis of rotation). Further increases in projection number above this value increase the signal strength, reducing the variability observed within a homogeneous substance. To determine the optimal number of projections for later experimentation, a <2mm ground dry ferrosol was placed in a 30mm PVC tube and mounted on the CNC manipulator. A series of scans were acquired using 400, 600, 800, 1000, 1250, 1400 and 1600 projection angles in a 360° revolution. The remainder of the scan parameters (180kV, 120μA, 0.125mm Cu filter, 200ms integration time, 68.7μm voxel size and fast scan protocol with the Direct X-ray source) remained constant. Following reconstruction, the standard deviation of grey values in a consistent section of the PVC and for a transect through the soil medium was calculated for each scan. The resultant data (Figure 3.6) indicated a decrease in variance with increasing projection angles. There is a diminishing return where further increases in projection angles (and scan time) do not significantly improve the image quality (signal to noise). An optimum value can be obtained which is specific to the density of the sample, resolution, the energy parameters used and the time available for scanning. The studies reported in this thesis used 1250 projections (step size 0.288°) to provide optimal signal strength (Figure 3.6) in reasonable scan times.

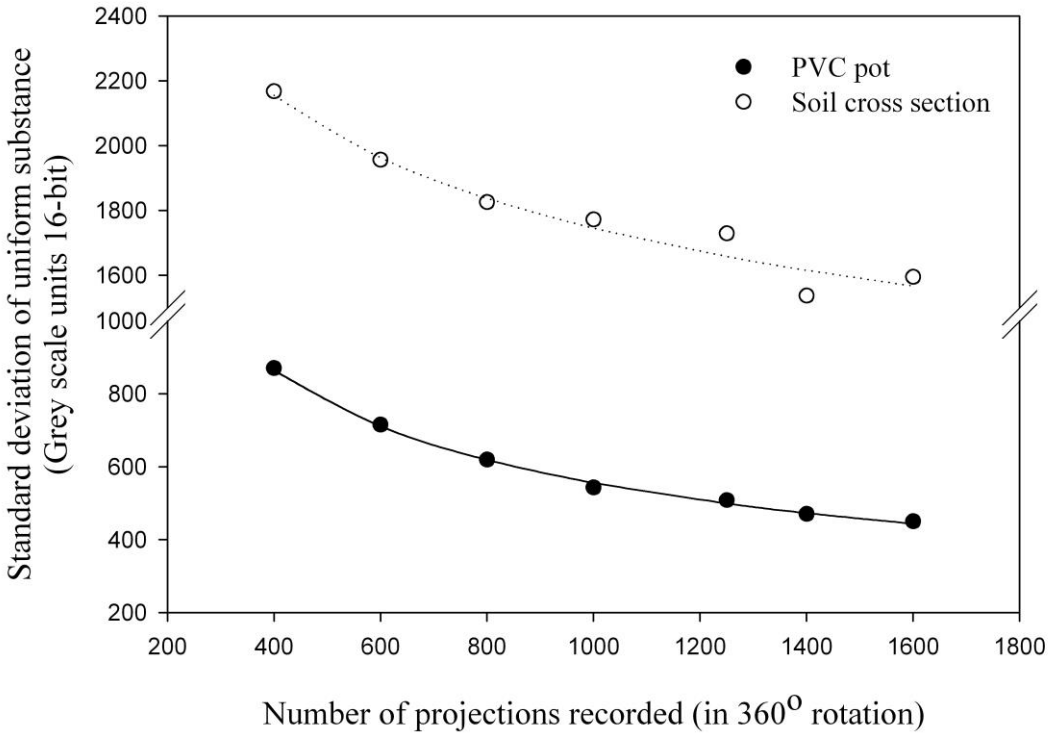

Figure 3.6| Increasing the number of projections recorded using constant rotation CT protocol, increases the signal to noise ratio as expressed by decreasing standard deviations of two observation substances in soil scans. The standard deviation of grey values observed for a consistent location of PVC (solid points) and a soil transect (open circles) revealed a decrease in variance with increasing projections. 1250 projections represented a compromise between scan time and image quality.

As technology continues to develop scan times are becoming faster and the capacity for data generation continues to accelerate. The major limitation to high throughput phenotyping using X-ray CT is data processing. To a certain extent the use of CT for soil pore space analysis has become rapid and standardised, but the challenges associated with root system segmentation is now the rate-limiting step for high throughput root phenotyping. This will be discussed in further detail in the following chapter.

3.6 Artefacts

There are a variety of subtle factors in the acquisition of CT images that can produce imaging artefacts. The main effects are beam-hardening, ring and star artefacts and they reduce the sensitivity of subsequent analysis or introduce a source of noise in the data. With methodological procedures these effects can be minimised during acquisition and reconstruction. Intensity variation is a more insidious artefact that is difficult to identify and correct, however precautions during acquisition can limit its significance.

3.6.1 Ring artefacts

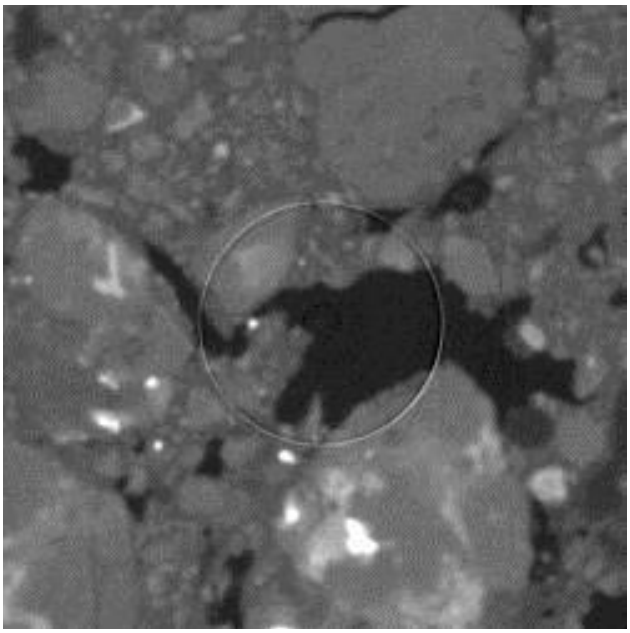

Figure 3.7| An example of a ring artefact, caused by a defective pixel during image acquisition. With the current UNE equipment, this can be corrected during or post image acquisition.

Ring artefacts appear as full or partial circles superimposed on the image centred on the rotation axis of the scan (Figure 3.7). They are caused by individual pixels or pixel clumps consistently registering false information during the scan (Cnudde 2005). They can be caused by differential sensitivity of the pixels in the detector, defects in the CCD sensor or from cosmic or scattered X-rays causing anomalous bright pixels (Mooney *et al.* 2012; Wildenschild *et al.* 2002). One response capable of removing the artefact has been to shift the detector during image acquisition. This means that insensitive or defective pixels do not contribute to the same region of the scan consistently and their influence is 'diluted' by functional pixels (Mooney *et al.* 2012). This is a very effective strategy but means that the sample cannot be projected onto the entire detector and therefore comes at a cost to the achievable resolution. A second method uses a pixel mask to identify and exclude data from defective pixels on the detector. During acquisition, the value for the missing pixels is interpolated from the surrounding values. While the number of

defective pixels remains low, this is an effective strategy for reducing ring artefacts and does not reduce the field of view. This strategy was used in the following studies.

The above techniques refer to reducing ring artefacts caused by unresponsive or defective pixels. This does not alter the effects of scattered or cosmic radiation and cannot remove artefacts following acquisition. Where anomalous signals are present in acquired images, single pixels can be identified, masked and interpolated prior to reconstruction. Alternately, ring artefact signals are present in the sinogram as a vertical line and could be identified automatically and removed in the reconstruction process (Cnudde 2005).

3.6.2 Beam hardening

Beam hardening is one of the most prevalent artefacts produced by polychromatic X-ray sources (Cnudde 2005). It occurs particularly in dense samples where the lower energy X-rays in the spectrum are preferentially attenuated by the sample. As the beam passes through the object, the lower energy X-rays are preferentially absorbed and the beam is 'hardened' leaving only higher energy X-rays which are not as easily attenuated by the sample (Mooney *et al.* 2012). This means that shorter ray paths attenuate proportionately greater X-ray energy per unit of path length than longer ray paths. The result produces scans that appear to be more dense (higher attenuation values) on the outside of the sample than the inside (Figure 3.8) even when the object is uniformly dense (Ketcham *et al.* 2011).

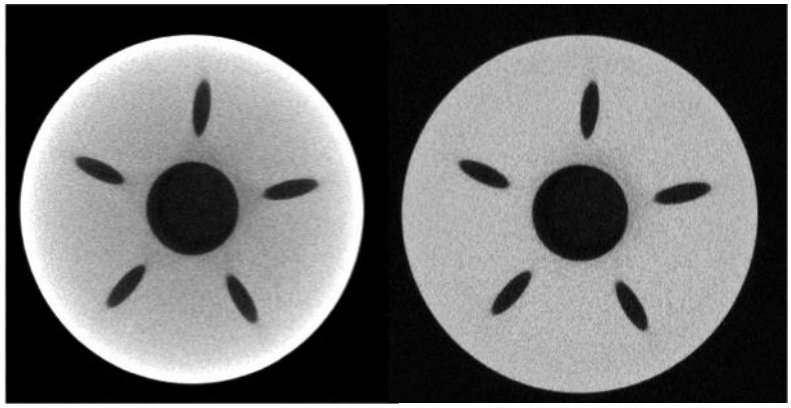

Figure 3.8| An example of beam hardening artefact as observed in an internal combustion fuel injector tip (Image from (Phoenix 2009)). (Left) a single transverse slice of the tip without the post reconstruction beam hardening correction; (Right) same scan with beam hardening correction.

Decreasing the size and density of the sample can reduce the beam-hardening artefact (Petrovic *et al.* 1982). However, this is not an ideal outcome for plant studies given the preference for large samples that represent field conditions. Similarly, the artefact can be completely avoided when using a mono-chromatic X-ray source but energy restrictions, sample size and access can be inhibitory at synchrotron facilities (Mooney *et al.* 2012; Wildenschild *et al.* 2002).

The most effective solution is therefore to use laboratory based equipment and reduce the effect as much as possible during acquisition and correct residual effects digitally during the reconstruction process. Just as monochromatic radiation does not produce beam hardening artefacts, reducing the range of X-ray wavelengths present in the incident beam will reduce the influence of the artefact. This can be achieved by using attenuating filters (e.g. Cu, Sn, Al or Brass foils), which 'pre-harden' the beam forming a lower boundary on the radiation spectrum produced (Cnudde 2005; Mooney *et al.* 2012; Wildenschild *et al.* 2002). In the same way 'post hardening' (where the filter is placed between the sample and the detector) can also be effective in reducing the low energy X-rays progressing to the detector. As filtering the beam significantly reduces the photon density at the detector, there is often need to increase the energy parameters to compensate and ensure adequate signal. The main disadvantage as it pertains to root studies is the loss of contrast associated with using attenuating filters. As such it is recommended that a low-attenuating filter be used in combination with digital compensation during reconstruction.

The GE phoenix X-ray proprietary reconstruction software (Datosx reconstruction) uses a beam hardening correction (BHC) index to alter the range of grey scale values observed at the boundaries of the scanned object. This function, when selected correctly, should ensure that voxels representing similarly attenuating substances will have equivalent grey values despite their position in the object. A single scan of the ferrosol and PVC pot previously described (acquisition settings: 180kV, 120μA, 0.125mm Cu filter, 200ms integration time, 1250 projections, 68.7μm voxel size and fast scan protocol with the Direct X-ray source) was repeatedly reconstructed with a

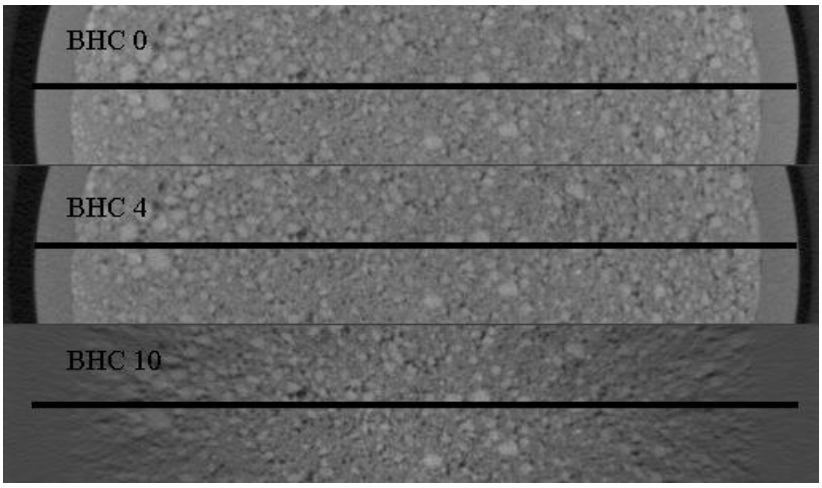

Figure 3.9| A single scan of a Ferrosol soil in PVC tube was reconstructed using beam hardening correction (BHC) indices of 0,2,4,6,8 and 10 (0,4 and 10 presented) and grey values along a transect (black line) were recorded to quantify beam hardening. See Figure 3.10

series of beam hardening correction index settings BHC0, 2, 4, 6, 8 and 10. A transect of the pots was taken at the same point in each pot (beam hardening reconstructions 0,4 and 10 in Figure 3.9). A parabolic function was fitted to the transect data (Figure 3.10) to determine whether pixels at the perimeter of the scan tended to have higher or lower grey values. Where higher edge grey values were present the trend line exhibited a minima (beam hardening artefact) as displayed by BHC 0 Figure 3.10. By contrast, where edge grey values were than those in the centre of the pot, a maxima was produced indicating overcorrection using the beam hardening correction module. This is most clearly displayed by higher BHC values such as 8 and 10 in Figure 3.10. A flat curve fitted to the transect data indicates the ideal BHC index which represents similar substances with comparable grey values. There is a small upward trend in the outermost voxels observed in the transect where no BHC was used (Figure 3.10) indicating that the edges of the image attenuated more X-rays than the centre (beam hardening observed). Overcorrection was also observed for values BHC 6 (maxima present) and greater indicating that the ideal value for the BHC index was 2-4. This factor is highly dependent on the sample density, the energy and filter configuration used. For the present experimental conditions, Beam Hardening Correction index 4 was used as it provided one of the 'flattest' transects (Figure 3.10).

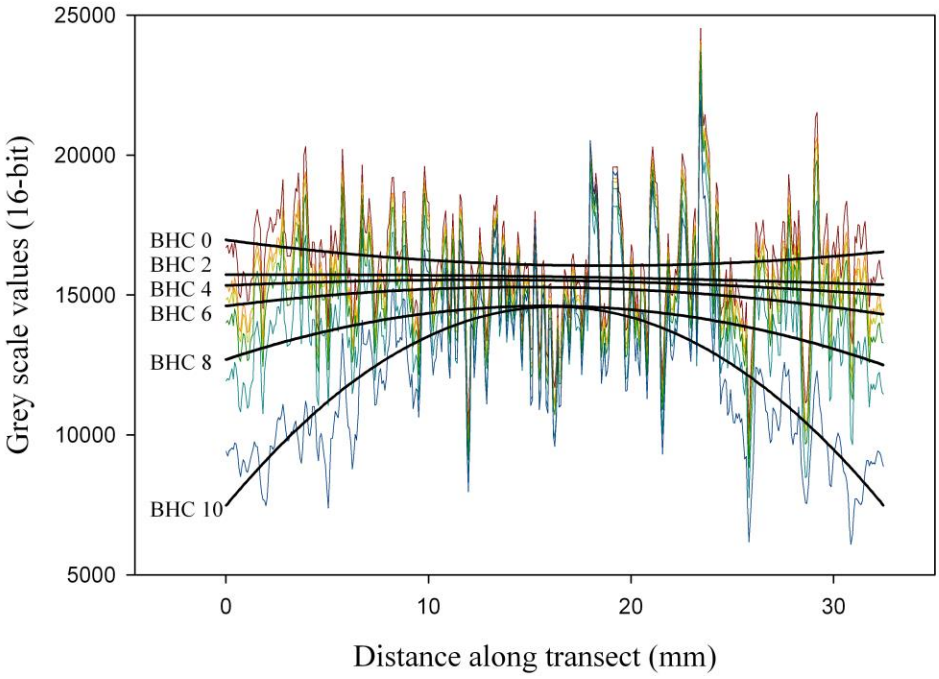

Figure 3.10| Grey values (16-bit) were observed along a transect Figure 3.9 of the same scan reconstructed with a series of Beam Hardening Correction indices (0,2,4,6,8 and 10). The grey values were plotted (spectrum red to dark blue representing index 0-10 respectively) and a parabolic function was fitted to indicate the upward or downward trend of the grey values at the outside perimeter of the scan. Upward trends indicate beam hardening, downward trends indicate over-correction. BHC 2-4 was observed to be most appropriate for the present experimental parameters.

3.6.3 Star artefacts

Star artefacts (sometimes referred to as 'streaking' or 'flaring') occur when very dense objects in the scan 'starve' the surrounding material of X-rays. Upon reconstruction this causes the surrounding material to have either higher or lower than actual attenuation values (Mooney *et al.* 2012). As in the case below (Figure 3.11) they can also be caused by scattered secondary radiation (Cnudde 2005). These effects can be minimised with post sample attenuating filters, or by increasing the kV to improve sample penetration, but as discussed these methods reduce contrast.

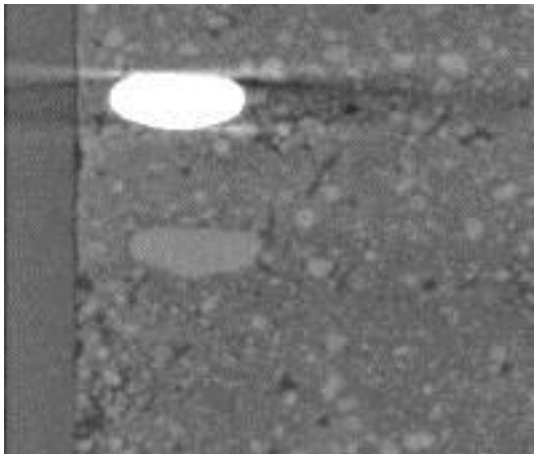

Figure 3.11| Example of dense, strongly attenuating soda-lime glass bead (top white bead) causing X-ray starvation around the bead. In comparison, The grey bead below composed of borosilicate glass attenuates X-rays to a similar extent to soil producing no start artefact.

Depending on the soil type, dense particles that produce star artefacts are rare and the artefact is minimal. However, the studies reported in this thesis used glass beads to provide spatial reference points. Dense soda-lime glass beads produced large star artefacts, whereas borosilicate glass beads had similar attenuation values to the surrounding soil. In this case it would be preferable to use the borosilicate glass beads where X-ray penetration is adequate and no star artefacts are produced.

3.6.4 X-ray intensity variation

Figure 3.12| Small depressions in Tungsten target caused by high energy electron beam causes 'pitting' or small depressions in the target surface. This degradation produces a lower intensity X-ray beam.

Intensity variation is an artefact caused by changes in the 'brightness' or flux of the X-ray beam during the scan. It is an insidious artefact as it can be hard to detect unless the projections are carefully inspected and compared. Intensity variation increases the noise of the scan, reducing the contrast between phases, but otherwise the images look satisfactory. Flux variation can be caused by generator instability, improper field strength controls (electron beam centring), heat generation on the target and target degradation (Mooney *et al.* 2012). Perhaps the most common (assuming a well functioning apparatus) is degradation of the target. The target is the site of conversion of accelerated electrons into X-rays. The typical yield of laboratory X-ray sources is 1-1.5% (X-rays generated for electrical energy input) with the remainder producing heat on the target. The high temperatures and high velocity electrons in a highly focused beam (<4µm spot size) commonly cause 'pitting' in the polished surface (Figure 3.12). As 'pits' form, a greater proportion of the X-rays generated are absorbed by the target material itself, reducing the photon flux from the source. The inclusion of cooling systems for the target has generally improved the target stability. However in the current system, the relatively large distance from the surface to the heat exchange, combined with the high rate of heat generation mean that target damage remains commonplace. Using lower energy tube settings where possible can reduce this damage as can pausing between scans to allow the coolant system to dissipate some of the heat from the target.

3.7 Conclusion

Ascertaining the 'optimal' tomographic acquisition parameters employed for experimentation is highly dependent on the sample characteristics, the x-ray machine used and the objective of the study. Whether formally recorded or otherwise, it is necessary to perform experimentation to determine whether the most appropriate settings have been employed. Resolution and contrast are commonly perceived as the principle limiting characteristics in X-ray CT soil studies. Settings and experimental design that optimise these characteristics are preferable. However, the resolution and contrast of the resulting tomographs are in dynamic equilibrium with capturing practical sample sizes, in reasonable scan times, at appropriate energy ranges (or radiation exposure) with minimal artefacts. Compromise is therefore commonplace but the predominant objective must be to achieve appropriate image quality for the desired post processing analysis. Recent technological developments have relaxed the limitations to the rate and size of image acquisition, however the rate limiting step has generally now become post processing, an exercise readily complicated by suboptimal image capture parameters. The above chapter represents the procedures and steps taken to quantify and determine the most appropriate acquisition settings for the following experimental studies.

Chapter 4 : Image Processing Challenges

X-ray CT provides a non-destructive and spatially referenced digital representation of the samples scanned. This makes it possible to measure 3D and temporal characteristics of the sample that would otherwise be difficult or impossible. Quantification is achieved using 'image-processing' techniques, which perform spatially adapted (often matrix) mathematical operations on the data. There are a plethora of algorithms commonly used to filter, identify, separate (segment) and analyse features in a volume, the specific method appropriate is highly dependent on the original data and the desired 3D measurements relevant to the study.

Substantial improvements in CT technology have enabled high rates of acquisition and reconstruction which were once very limiting (Gregory *et al.* 2009; Mooney *et al.* 2012). Currently, the major limitation to applying CT to plant root phenomics is the image processing step, specifically the development and application of algorithms to segment root material. There has been significant work to solve the problem, however to date, no highly successful or robust methods have been proposed that are capable of identifying and segmenting the root system from the soil/pore network (Mairhofer *et al.* 2012; Mooney *et al.* 2012). Software for the efficient handling and processing of CT data is essential in progressing the science and allowing 3D root architecture to be efficiently and rapidly measured.

As previously discussed, resolution and pot size has placed a severe restriction on utilising X-ray CT for root morphological studies. To extend the soil volume captured, multiple vertically adjoining scans of a narrow pot can be acquired, achieving high-resolution images of a larger rooting volume. The 'stitching' process however, requires grey value correction and image registration or concatenation to produce high quality, seamless transitions between scans. Having produced a seamless and large volume, a segmentation protocol is necessary to isolate the root system from the image. This procedure remains a significant problem. There is a dearth of available software for this highly specific and complex task. X-ray CT distinguishes materials on the basis of their differential attenuation of X-rays,

however, it is very common for many portions of the edaphic environment to produce similar attenuation coefficients. As a result, grey scale values alone are insufficient to segment the root system from all other soil phases. Morphological filters based on shape or 3D continuity provide an opportunity to isolate the root system. Following segmentation it is necessary to extract root system architectural information from the 3D structure. This also is a task requiring software development. While several algorithms have been produced for analysing other 3D objects, there is few capable of extracting the specific root system characteristics that are descriptive of root function.

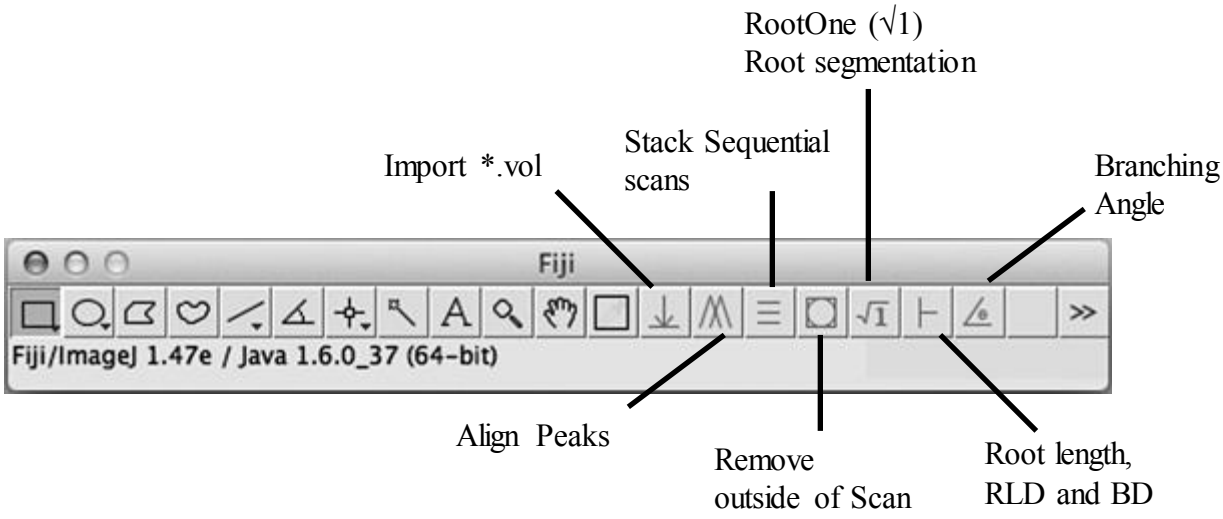

Figure 4.1| Screen shot of the Image J macro toolbar- 7 custom made icons (grey and annotated) were designed to streamline image handling processes making more automatic while remaining adaptable to different applications. *'Import *.vol'* enables the direct import of the proprietary Phoenix volume files into Image J. *'Align peaks'* identifies the first major peak of the grey value histogram and shifts the histogram to a defined standard value. *'Stack sequential scans'* concatenates vertically adjoining scans to create a single, seamless volume. *'Remove outside'* removes the erroneous region at the perimeter of the scan. *'RootOne'* attempts to segment the root system from volumetric scan data. *'Root Length, RLD and BD'* skeletonizes and calculates root architectural details (root length, rool length density and branching density) from a segmented image. *'Branching Angle'* facilitates the manual calculating of branching angle from 3D data.

In an effort to overcome these challenges, the following chapter outlines the experimental process and development of an Image J -FIJI (Schindelin *et al.* 2012) toolbar (Figure 4.1 Code presented in Appendix 1) for improving the speed, handling of images and segmentation of root systems from CT scans. The toolbar is written in the Image J macro language and has been discretised into steps (Figure 4.1) but can be combined for greater automation. However, when the code is concatenated it is

highly specific to the application and scan parameters (e.g. Figure 4.2 Step D, code presented in Appendix 2). The toolbar format offers greater flexibility to the user. The development of the toolbar and the image processing performed has been concurrent with the experimentation described in the following chapters. As such reference will be made to the subsequent chapters when describing methods or data that are more thoroughly described therein.

Figure 4.2 graphically represents the steps in the development of the above toolbar (Figure 4.1) and the RootOne segmentation algorithm. The initial stage (Figure 4.2 Step A) represents a pilot study and experimental optimisation phase of the project providing an opportunity to identify challenges and present visual confirmation of the potential of the technique as largely described in Chapter 4 (Figure 4.3 A). The second stage (Figure 4.2 Step B) was a replicated trial incorporating strategies to improve scanning efficiency and validate the technique for measuring root system attributes (see Chapter 5). Image processing at this point remained manual and is described in greater detail in the following chapter. Stage C (Figure 4.2) represents a study exploring morphological root responses to localised P supply (see Chapter 6). While image processing and segmentation was predominantly carried out manually, the experimental setup was further optimised and empirical root system measures were automated improving the processing time. The final two stages (Figure 4.2 Step D and E) represent an attempt to incorporate the observations made during manual segmentation to automate the handling and segmentation process. Step D represents the use of an automated segmentation tool to extract the root system for faster 'cleaning' using the manual method. Step E includes further refinement to the segmentation algorithm, with more automated filters. These stages are accompanied by a loss in segmentation quality, that is an increase in misclassified voxels (particularly at the edges of the scan) (Figure 4.3), however also represent a significant increase in the processing efficiency. The coding associated with Stages D and E (the development of a macro and toolbar respectively) are included in Appendix 2 and Appendix 1

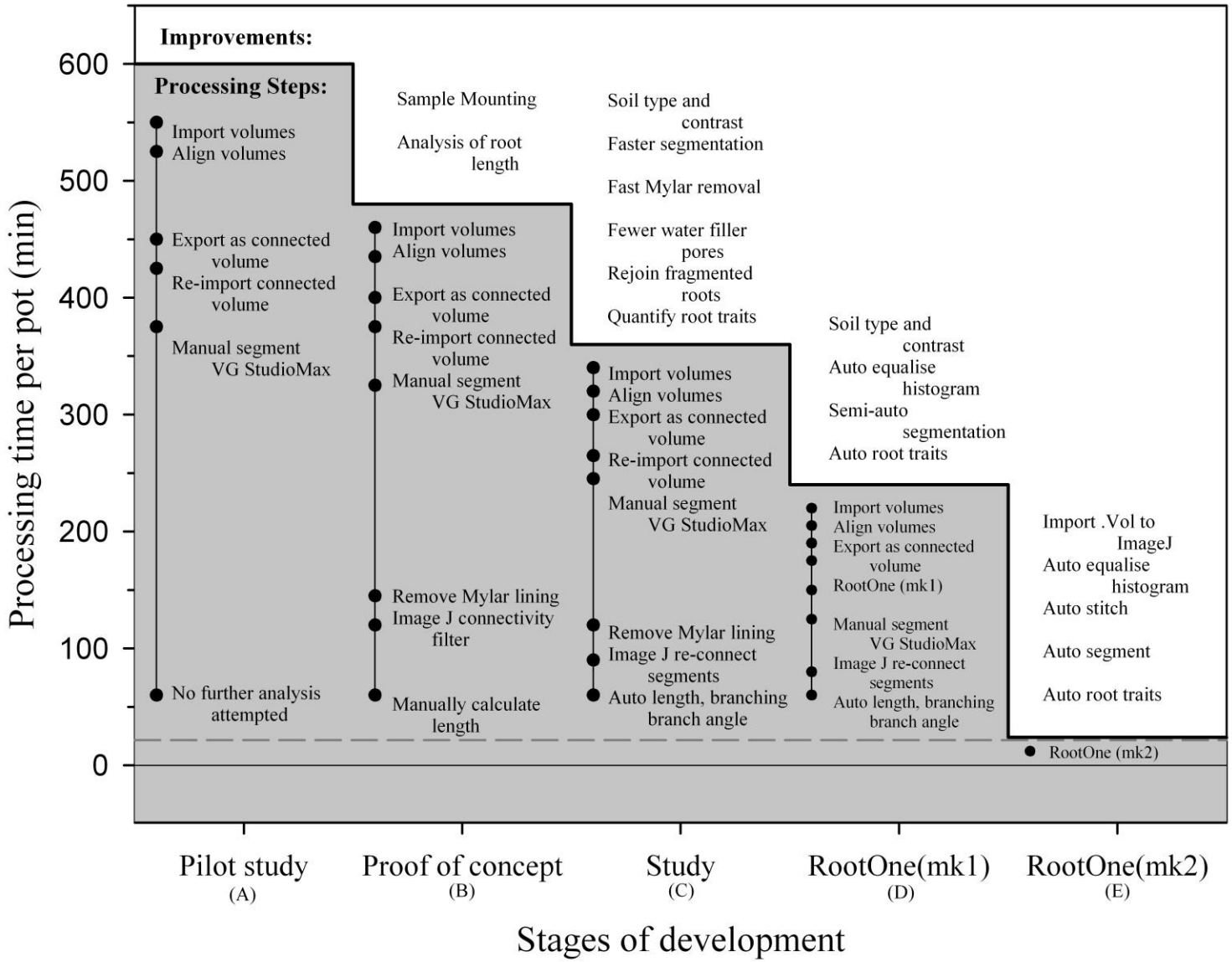

Figure 4.2| Development process for Image J macro toolbar. An estimate of the time (solid black line) required for processing a single sample at each step of the developmental process. The tasks under the line (shaded) represent the general tasks carried out. Items above the line indicate the improvements made to the experimental setup or automation of image processing. The time required to scan a sample (21.5 mins -broken grey line) refers to three vertically adjoining scans requiring 4min:10s each, with time for sample mounting, calibration and reconstruction. An example of the segmentation output for developmental steps (A-E) are presented with corresponding alphabetical labels in Figure 4.3 (A-E).

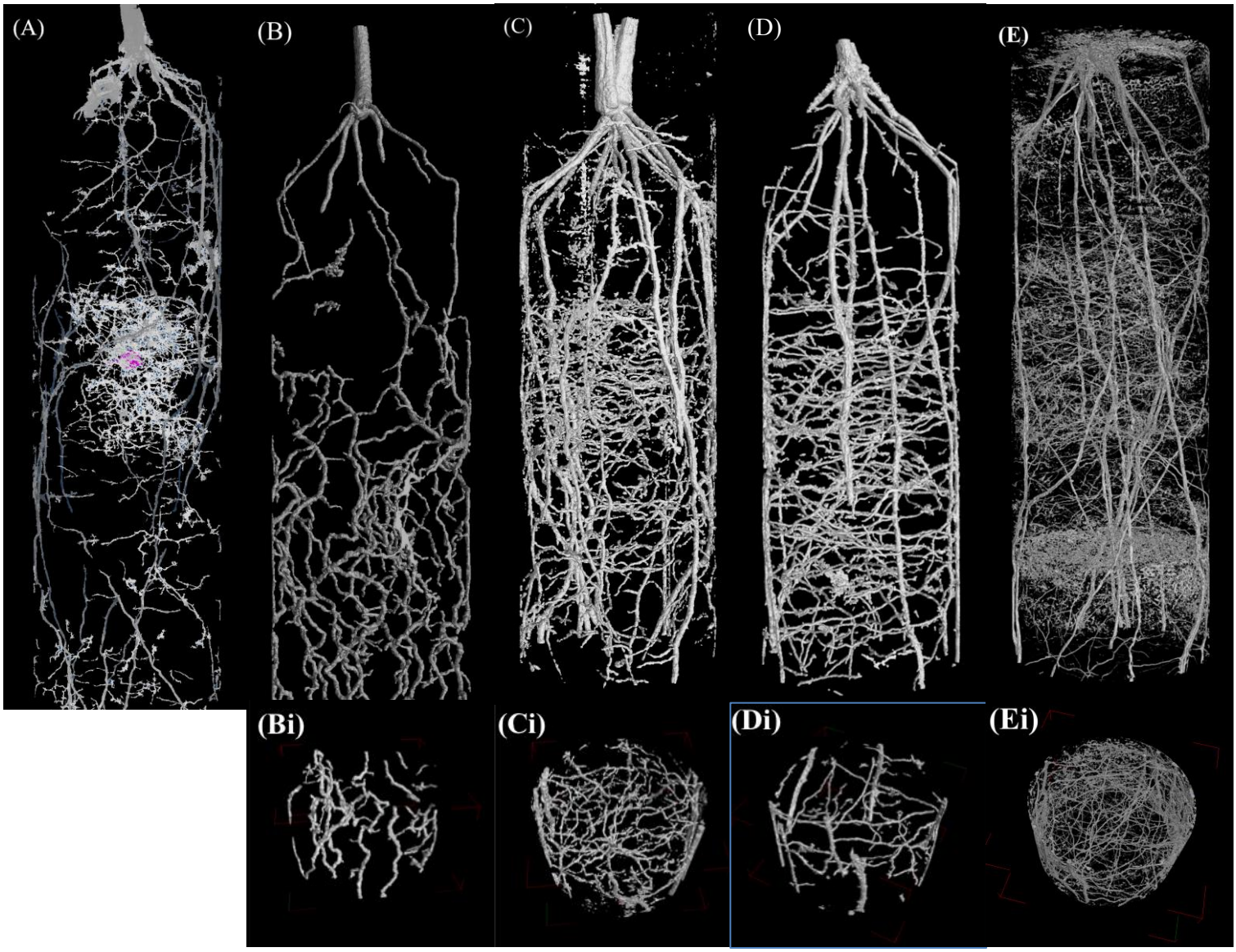

Figure 4.3| Example of segmentation output from each developmental step represented in Figure 4.2 (A-E) with corresponding character labels (A-E). (A) 4 vertically adjoined scans of a triticale root system 20 DAS responding to DAP granule (centre). (B) 4 vertically adjoining scans of wheat root system 28 DAS. (C) 3 vertically adjoining scans of wheat root system a 28 DAS in response to a banded P treatment (centre). (D) 3 vertically adjoining scans of wheat root system 28 DAS in response to a steep P gradient. (E) 3 vertically adjoining scans of wheat root system 28 DAS in response to uniform P distribution using automated segmentation. Images (Bi-Ei) represent a 250 slice subsection from the centre of the image (corresponding to images labelled B-E respectively) displaying the root segmentation through the centre of the pot. Automated segmentation (E and Ei) display the greater presence of noise, particularly at the edge of the pot. Earlier segmentation attempts (A and B) are characterised by roots with 'missing segments', which is improved through C and D. Method E, while automatic is prone to noise (cloudy structures) particularly at the bottom of the pot where structure the soil structure varies.

4.1 Registration and stitching laterally adjoining scans

One of the key limitations in studies using plants in small soil volumes is that roots rapidly encounter the edge of the pot, confounding plant physiological responses and curtailing the maximum growth period (Passioura 2002). To achieve functionally relevant scan resolution while maintaining field and plant relevant sample sizes,

multiple adjoining scans of a small diameter cylinder can be taken to allow a larger soil volume to be imaged at high resolution. This method allows a much larger root system to be analysed and the observation of more mature root system traits. Many studies have been conducted on seedlings 0-16 DAS (Gregory *et al.* 2003; Jenneson *et al.* 2003; Perret *et al.* 2007; Tracy *et al.* 2011; Tracy *et al.* 2012), however the extension of the scanned area down a pot allows more mature plants (e.g. 30 DAS) to be observed (Flavel *et al.* 2012). Imaging the pot in vertically adjoining scans increases the scan time and creates some challenges for data processing. All of the scans must be imported into the same program (with sufficient computer system resources/strategies to accommodate the data) and aligned (or stitched) to form a continuous volume. A further challenge to this process are the small fluctuations in X-ray generation or sample composition that can influence the grey scale values assigned to each attenuating material. This can produce inconsistent grey scale values and must be corrected in the stitching process. Each of these steps is outlined below.

4.1.1 Direct import of volume files

There are many reconstruction software packages available to produce tomographs, however the most efficient platform with features specifically optimised for the GE Phoenix V|tomex|s CT scanner is that provided with the scanner. The GE *Datos|x Reconstruction* package is optimised for use with a GPU cluster and reconstructs 512 x 512 x 512 tomographs in ~30 sec. This software is based on Feldkamp filtered back-projection method for cone based CT (Feldcamp *et al.* 1984) and writes the tomograph data to hard disk in a custom raw file format (for details see Appendix 3). The GE system is designed to open the tomographs using the VG StudioMax software from whence it can be exported into standard formats (e.g. a stack of .tiff slices). This process is helpful where data is to be directly visualised using VG StudioMax, however less efficient when data requires further analysis in another program. One of the major improvements in the RootOne development process (Figure 4.2 Step E) was the inclusion of a macro to directly import the *.vol file into Image J (Figure 4.1). This circumvents the time intensive step of importing tomographs into VG StudioMax only to be exported (as a *.tiff stack) and then imported into Image J for further processing. The structure of the *.vol file necessitates some prior knowledge about the file before importing, therefore the

macro reads information from the *.vgl file produced simultaneously by the GE reconstruction software.

4.1.2 Align histograms of adjoining scans

Small variations in the content of CT scans (e.g. the presence of higher attenuating particles) and minor drifts in the X-ray beam intensity (see 3.6.4) can cause subtle changes in the grey-scale values assigned to similar substances between sequential scans (Figure 4.4 A and C). When stacking vertically adjacent tomographs, these variations can produce non-uniform grey values, meaning that homogeneous substances can have multiple grey values or different substances could have similar grey values (Figure 4.4 D). In practise, this variance makes segmentation attempts difficult and causes uncertainty in the portion of the scan being isolated based on grey values.

Histogram shifts are generally not as significant as those presented in Figure 4.4 but remain a significant limitation to segmentation when not properly corrected. Early development of an appropriate processing procedure (Figure 4.2 Steps A-C) involved reconstructing into 32-bit float format and manually determining a consistent range of values common to all of the scans to be stitched together. Reconstruction into 32-bit format results in less bias from the presence of highly attenuating compounds in the scan as the larger grey value range makes the scale 'less relative' and 'more absolute'. This is because there are more unique values in the 32-bit depth range ($4.295_{x10}{}^{9}$ unique values) as compared to the 16 or 8-bit depth ranges (65536 and 256 unique values respectively). In these early processing steps, scans were imported into VG StudioMax using the predetermined range of grey values reducing the bit-depth from 32-bit to 16-bit. This is sometimes referred to as the 'window' method (Bouckaert 2012) and can provide greater contrast than would otherwise be achievable when the scan is directly reconstructed into a lower bit-depth. This manual method provided similar histograms, however some variance was occasionally observed.

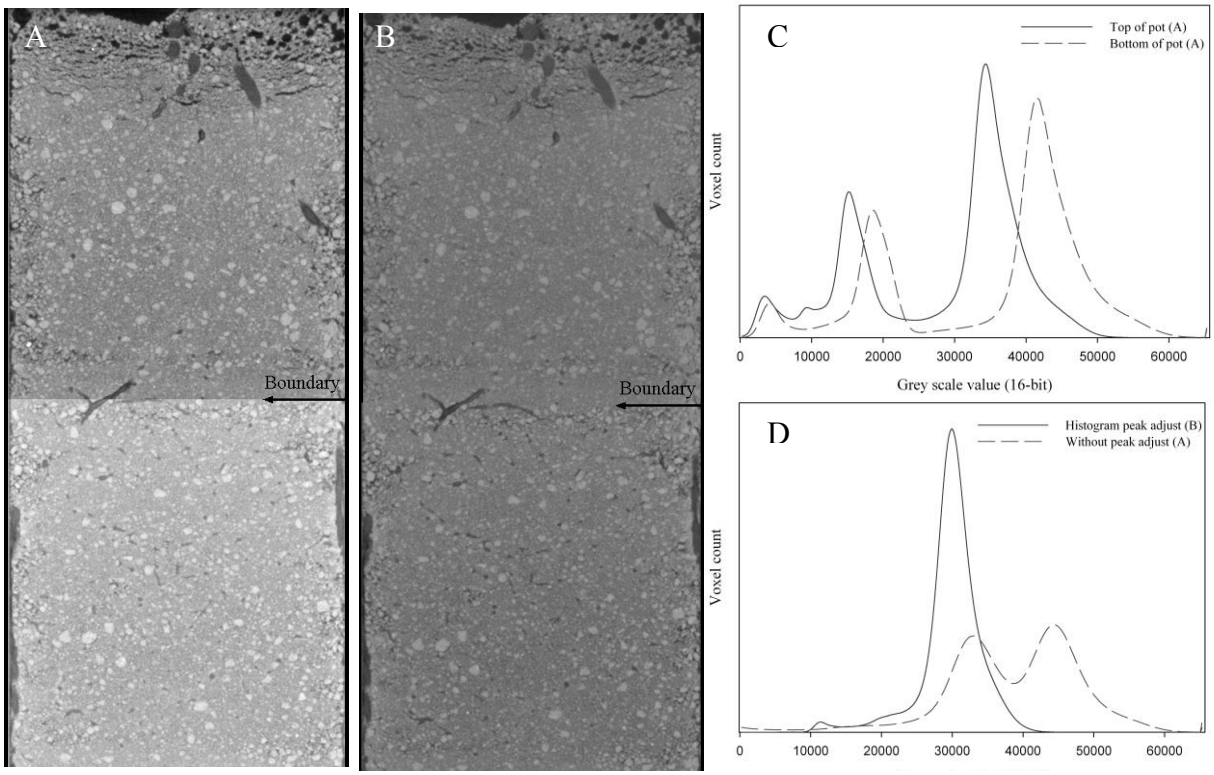

Figure 4.4| Influence of drifting grey values in individual scans on final combined volume grey value continuity. (A) A single sample scanned in two parts (consistent scan parameters) with subtle compositional changes causing different grey values to be assigned. When digitally 'stitched' together, the resulting volume produces discontinuous grey values. (B) The same sample having applied the '*Align Peaks*' method to produce uniform grey scale assignments across the two volumes. (C) Grey scale histograms of the individual top and bottom scans of [A] displaying the shift in grey value assignments and the relative similarity of the histograms. (D) The grey value histogram of the stitched images. Histogram for [A] has a bimodal soil peaks and clear overlap between the soil peak (top) and the root peak (bottom). Histogram for [B] has a single soil peak and lower grey values more uniquely represent root and air respectively.

Later developments (Figure 4.2 Steps D and E) used a customised peak matching method (Figure 4.1). This method identifies the largest peak of the histogram (commonly the soil peak in these examples) and aligns these to a coincident grey value set by the user. This method provided significantly more consistent grey values between scans (Figure 4.4 B), was simple, computationally efficient and automatic. The peak matching method is not suited to all applications as it assumes that the variance observed in the histogram is consistent between scans. For the experimentation presented in this thesis, this was the case but in circumstances where the variance of a substance's attenuation values change (e.g. where there is inconsistent sample diameter) this method is less applicable. In such cases, histogram equalisation (for uni-modal data) and contrast enhanced adaptive histogram equalisation (for multi-modal data) are more appropriate but may increase computational demands (Zuiderveld 1994).

4.1.3 'Stitching'- merging adjacent scans

'Stitching' scans together produces a continuous and seamless volume from multiple adjacent scans (Figure 4.4 B). When acquiring the scans it is necessary to ensure there is a small region of overlap at the boundary to confirm the entire sample is captured and to provide reference data for stitching. This can be achieved by shifting the sample a calculated distance for sequential scans using the CNC manipulator. At the resolutions commonly achieved with μ-CT, CNC backlash (i.e. mechanical inaccuracy) can be observable. To reduce backlash, the sample should be shifted in the same direction for sequential scans (i.e. always start with the top of the sample and move downward or vice versa). When this is practised and assuming that the rotational axis is consistent during the vertical translation, a consistent shift distance can be achieved between scans and stitching can occur by simply removing duplicate slices and concatenating stacks. This is perhaps the simplest method for stitching and has computational benefits but is less adaptive than more automated methods and does require some user input.

Automated methods, such as those already available in Image J (Preibisch *et al.* 2009) commonly use Fourier transforms to identify common regions and combine volumes. These methods are very effective on highly heterogeneous data, containing unique structures but less successful where there are limited distinctive features. Soil is simultaneously heterogeneous and homogeneously 'noisy' depending on the scale of measurement, which makes automated stitching methods somewhat less robust in soil samples.

For these reasons the somewhat less complex procedure of removing duplicate slices and concatenating stacks was implemented for subsequent experimentation. The method was at first performed manually in VG StudioMax using the 'Transformation' toolbar (Figure 4.2 Steps A-D) but was then automated for the final step in RootOne development (Figure 4.1 and Figure 4.2 Step E). This improvement represents a significant time advantage. The result is a seamless transition between scans (Figure 4.4 B see marked boundary) and any sub voxel variance that may occur in the physical or digital stitching of this method is considered insignificant in

comparison to the variance in both the root system and segmentation algorithms used to extract the root system from scans.

4.1.4 Exclude un-usable data

The 'exclude outside' function (Figure 4.1) simply removes the data that is outside of the field of view. While tomographs are generally reconstructed as a rectangular prism with a maximum size (in voxels/pixels) equal to the detector width x detector width x detector height, the maximum accurate data is represented by a cylinder with radius equal to the pixel width and height to the detector height (in pixels). The voxels outside the cylinder are reconstructed based on an incomplete number of projections as the object passes outside of the field of view at some points during the scan. As a result the computed tomography numbers (CTNs) are calculated based on an incomplete dataset and are therefore erroneous. If the object fits wholly within the field of view, the region outside the cylinder is simply an artefact of the reconstruction process. This region typically consists of a non-descript textured grey region represented by a uni-modal peak on any single tomograph slice (i.e. Figure 4.5 Aiii). However, where a cone beam source is used, artefacts associated with non-uniform penetration distance at the top and bottom of the scan can create a secondary peak on the histogram when the whole volume is surveyed (e.g. Figure 4.5 Aii). The artefact peak or peaks occupy the same region of the grey scale as the 'root' and as a result can create challenges for processes that depend on histogram functions (such as peak fitting etc.). The 'exclude outside' function, simply creates a user defined region to further process and the remainder of the volume outside of this cylinder (the grey region of Figure 4.5 B) is written to a value of 0 to produce an image similar to Figure 4.5 C. This is a common operation when processing tomographs (Perret *et al.* 2007). This rapid step improves the efficiency (less data) of later processes and reduces processing errors.

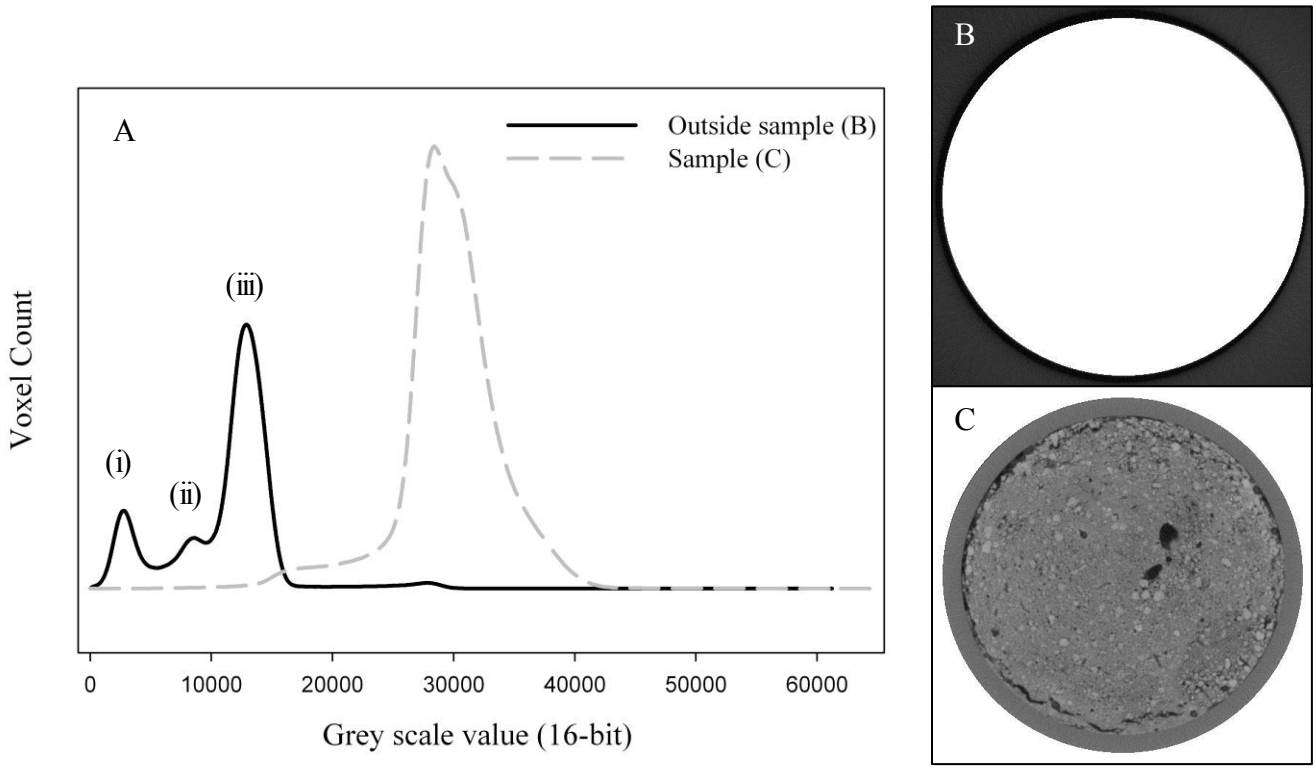

Figure 4.5| Exclude outside function. (A) The histograms of the excluded 'outside' or extrapolated region of the scan [B] and the sample [C]. (i) Denotes the peak associated with air outside the sample but inside the reliable scan region and indicates where pore space will represented on the sample histogram if greater pore space was present in this image. (ii) and (iii) denote the distribution of grey values calculated for the region outside the sample and reflect extrapolated noise. The reason for the bi-modal distribution is small cone shaped region at the top a bottom of the scan which remains outside the field of view for small portion of the scan time (due to 'cone' X-ray beam geometry). The region (ii) has fewer observational projections and therefore appears 'darker' on average. (B) and (C) represent the excluded and sample regions respectively at a single slice. Note: the *'exclude outside'* function replaces the excluded values with '0' and would ordinarily be represented by black rather than white.

4.2 Segmenting root systems

The most significant limitation to the use of X-ray CT for observing root development, distribution and morphological characteristics is the difficulty in isolating and identifying roots from tomographs. Despite the 30-year history of using X-ray CT for root studies, a standard and robust root segmentation algorithm has yet to be proposed. Many different methods have been suggested ranging from simple thresholding to bi-level or adaptive thresholding, morphological and tracking algorithms. Many of these have been recently reviewed by Mooney *et al.* (2012) and Mairhofer *et al.* (2012) and will not be extensively discussed here. The predominant hurdle is that roots and organic material attenuate x-rays at an intermediate rate between that of air and soil (Figure 4.6). Particularly with polychromatic sources, the

range of grey scale values observed for different phases often overlaps. This is due to both the partial volume effect and the overlap in x-ray attenuation of different substances in the sample (Heeraman *et al.* 1997; Mooney *et al.* 2012). As such, boundaries and the pixels that represent each phase can be hard to distinguish.

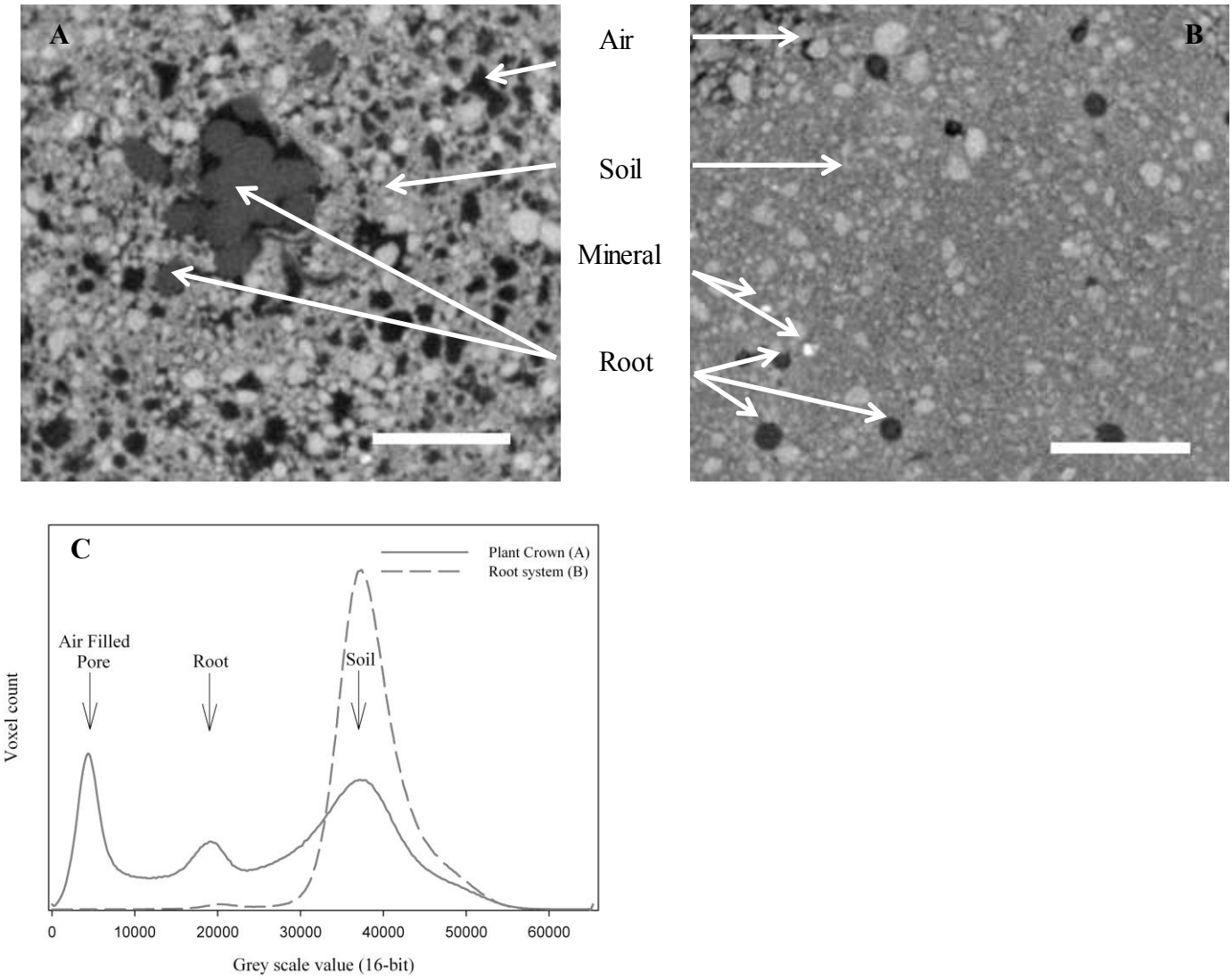

Figure 4.6| Demonstrating the similarity of grey values observed between phases. (A) Single slice transecting the crown of wheat plant. The high presence of organic material in the slice accentuates the peak observed in the histogram for that slice [C-solid line]. (B) Single slice ~4mm below the surface transecting roots at that depth. The relatively lower abundance of root and air phases through this slice reduces the presence of peaks in the histogram [C-broken line]. (C) Histogram of slice (A) and (B) represented by solid and broken lines respectively. Peak phases are indicated with considerable overlap in grey values, particularly where there is higher phase abundance (A). Scale bars 5mm.

4.2.1 Partial volume effects

The partial volume effect (PVE also termed the volume averaging effect) is perhaps the most fundamental challenge associated with CT image processing. It occurs when more than one phase is present in the point source region representing a single voxel. The CTN or grey scale value assigned to a voxel is relative to the average attenuation of the voxel contents. Where a voxel is partially occupied by air and by soil, the resultant attenuation value is partway between that of the soil and the air, relative to the proportion of each in the voxel (Figure 4.7). Notably, the average attenuation of air and soil produces a similar attenuation range to root tissue (Heeraman *et al.* 1997; Ketcham *et al.* 2011). This is the process of discretising a spatially continuous sample into a limited number of voxels. The result of this method of imaging is that all phase boundaries are blurred or poorly defined (Ketcham *et al.* 2011; Mooney *et al.* 2012).

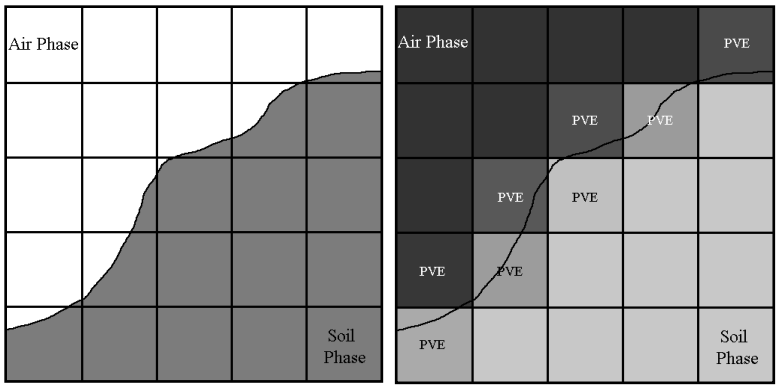

Figure 4.7| Diagrammatic representation of the Partial Volume Effect. (Left) represents a region of 3D space partially occupied by air (white) and by soil substrate (grey). When the region is divided into discrete voxels (black lines and Right), the attenuation coefficient for a voxel is given by the average attenuation of the contents of that voxel (affected voxels marked 'PVE'). This produces ill-defined phase boundaries and 'soil/air' voxels that

Understandably, the influence of the PVE is relative to the resolution. Where resolution is low (large voxel size) the likelihood of that voxel representing more than one material is high and conversely as resolution increases, the influence of the PVE is reduced (Cnudde 2005). The PVE dictates that the smallest object able to be observed must therefore be at least as big as two voxels in its smallest dimension (assuming detector noise is negligible). As is the case for roots, the root diameter must be greater than 2 times the voxel size to be detectable (Bouckaert 2012). A feature which has until recently limited the application of CT to root studies to small pots or course root systems.

The PVE causes significant difficulties in the segmentation of root systems (Flavel *et al.* 2012; Gregory *et al.* 2003; Heeraman *et al.* 1997; Kaestner *et al.* 2006; Tracy *et*

al. 2010). Where global or bi-level thresholding and mixed modelling is performed, PVE voxels are regularly misclassified as 'root' (Mooney *et al.* 2012; Taina *et al.* 2008; Tracy *et al.* 2011). In 'tracking' type approaches, including level-sets methodology, the PVE can cause 'breakouts' where the algorithm includes the PVE shell around connected soil aggregates as 'root' in the segmentation (Mairhofer *et al.* 2012). One approach to reduce the impact of the PVE is to use soil with finer pore-space than the resolution of the scans (Gregory *et al.* 2003). This technique also reduces the voxels that contain appreciable air and reduces the PVE. While care should be taken not to impose artificial physical and chemical constraints (anaerobic conditions, high bulk density etc) to the root system, a finer textured soil can provide greater contrast between the roots and the supporting medium. This approach was adopted in the following methodology as early attempts (Figure 4.2 Step B) used 0.5-1mm sand fractions, followed by whole Ferrosol (Isbell 2012) soils in later experiments (Figure 4.2 Step D and E). This method improved the efficacy of automatic segmentation algorithms appreciably.

4.2.2 Overlapping histogram

In addition to blurred phase boundaries caused by the PVE, the distinction between substances can be hampered when different combinations of mass density and atomic composition compensate to produce similar attenuation coefficients. Since a material's linear attenuation coefficient is determined by the sum of the Crompton scattering and photoelectric absorption, different substances can be represented by similar grey values (Wildenschild *et al.* 2002). A substance with high mass density (and low atomic weight) can produce similar values to a substance with heavy elemental composition (and low mass density). While possible at wide extremes of elemental composition and mass density, in soils this feature can be hard to distinguish from the PVE. However, much more common in typical soils are non-root substances with similar atomic composition and density. These include water filled pores, organic matter assemblages or artificial compounds such as plastics and carbon based polymers (Elyeznasni *et al.* 2012; Flavel *et al.* 2012; Mairhofer *et al.* 2012; Mooney *et al.* 2012).

Dual energy scanning can be used to differentiate between similarly attenuating substances by providing different incident beam energy and a corresponding variation in attenuation coefficients. The combination of the two images can help differentiate the similarly attenuating substances (Wildenschild *et al.* 2002). Best results are achieved with monochromatic synchrotron sources, however this method requires synchrotron access and the twice as many scans with high CNC manipulator repeatability or image registration (Wildenschild *et al.* 2002). As such this does not appear to be a viable alternative for high throughput applications.

The presence of 'non-root' substances in the 'root' portion of the grey scale spectrum is the major cause of simple segmentation method failure and is the fundamental limitation for digital root extraction (Figure 4.8.). Segmentation algorithms based on the isolation of roots from grey scale values alone will invariably include large fractions of misclassified voxels (Mairhofer *et al.* 2012; Taina *et al.* 2008). As a result, many authors have used thresholding methods as a starting point followed by morphological filters to remove some of the misclassified voxels (Mooney *et al.* 2012).

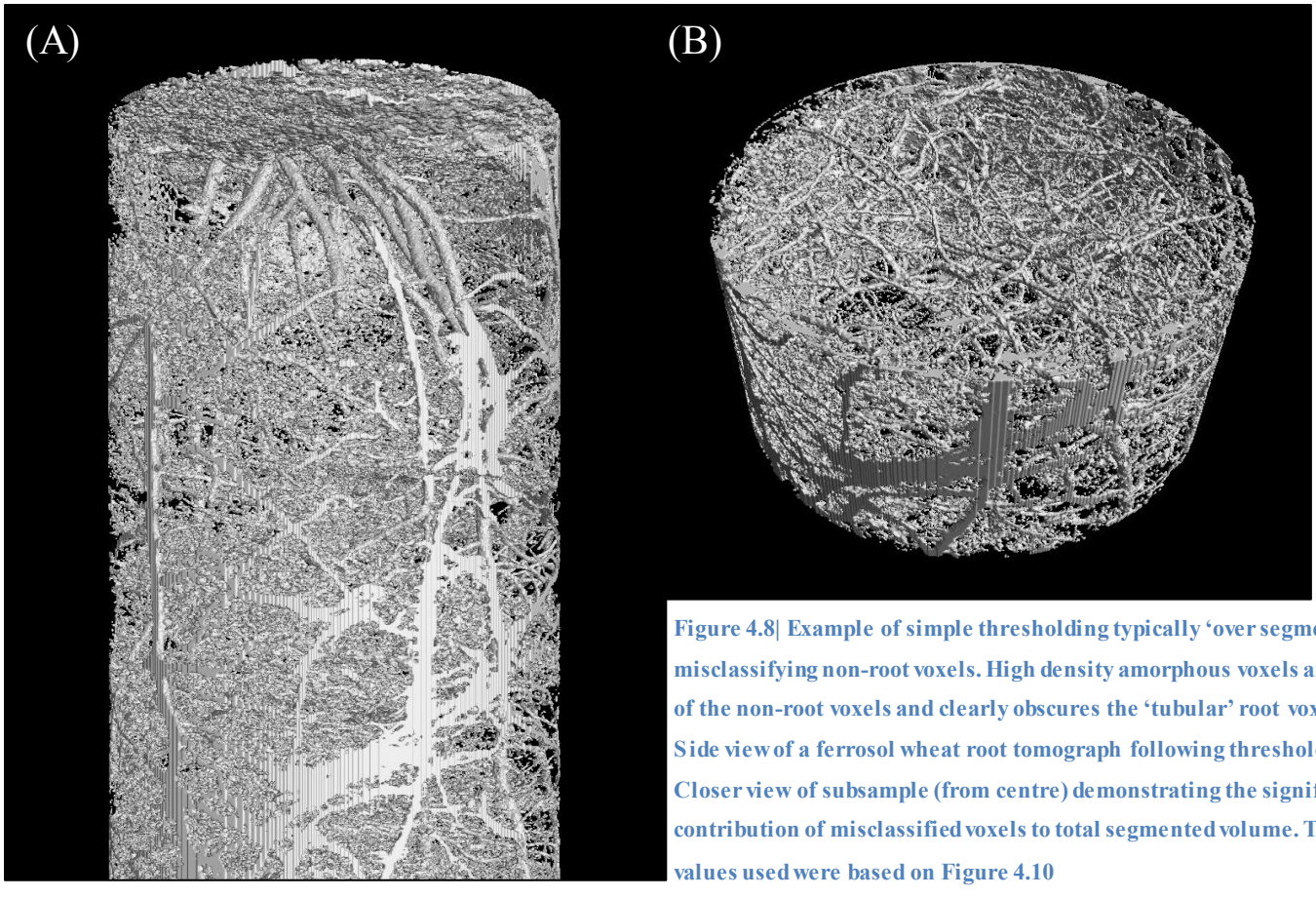

Figure 4.8| Example of simple thresholding typically 'over segmenting' or misclassifying non-root voxels. High density amorphous voxels are typical of the non-root voxels and clearly obscures the 'tubular' root voxels (A) Side view of a ferrosol wheat root tomograph following thresholding. (B) Closer view of subsample (from centre) demonstrating the significant contribution of misclassified voxels to total segmented volume. Threshold values used were based on Figure 4.10

4.2.3 Root segmentation: the development of RootOne

Initial analysis of the CT images confirmed that simple thresholding techniques were insufficient to segment root systems and were prone to misclassifying PVE voxels as 'root' (Figure 4.8). Due in part to the dearth of specialised root segmentation software, the early developmental stages (Figure 4.2 Steps A-D) relied heavily on user dependent local adaptive thresholding methods. Using the 'Region Growing' tool in Volume Graphics VGStudioMax 2.0, roots were identified by their grey values, shape and the continuity between adjacent slices. The 'Region Growing' tool was used to isolate the connected roots in the surrounding slices until voxels above a pre-defined threshold were encountered indicating the root boundary. The threshold values used were relatively consistent, but particularly where roots contacted large pores or similarly attenuating substances (e.g. Mylar® pot lining) 'break-outs' were observed where the pot, pores or PVE voxels could be included in the segmentation. In these situations the user reduced the threshold value below the point of 'breakout'. This often decreased how far the algorithm could 'track' the root in the adjacent slices but also reduced the misclassification of non-root voxels and improved the quality of the resulting data. This process was performed sequentially in two planes (viewing the slices in a top to bottom – viewing YX approach (Figure 4.9 left), followed by a side to side – viewing ZX direction (Figure 4.9 right)) to maximise the chance of root interception. It was considered unnecessary to perform the process on the third plane (the other sided to side plane – viewing ZY Figure 4.9 right) as the process was time intensive and there were very few additional roots observed in this direction.

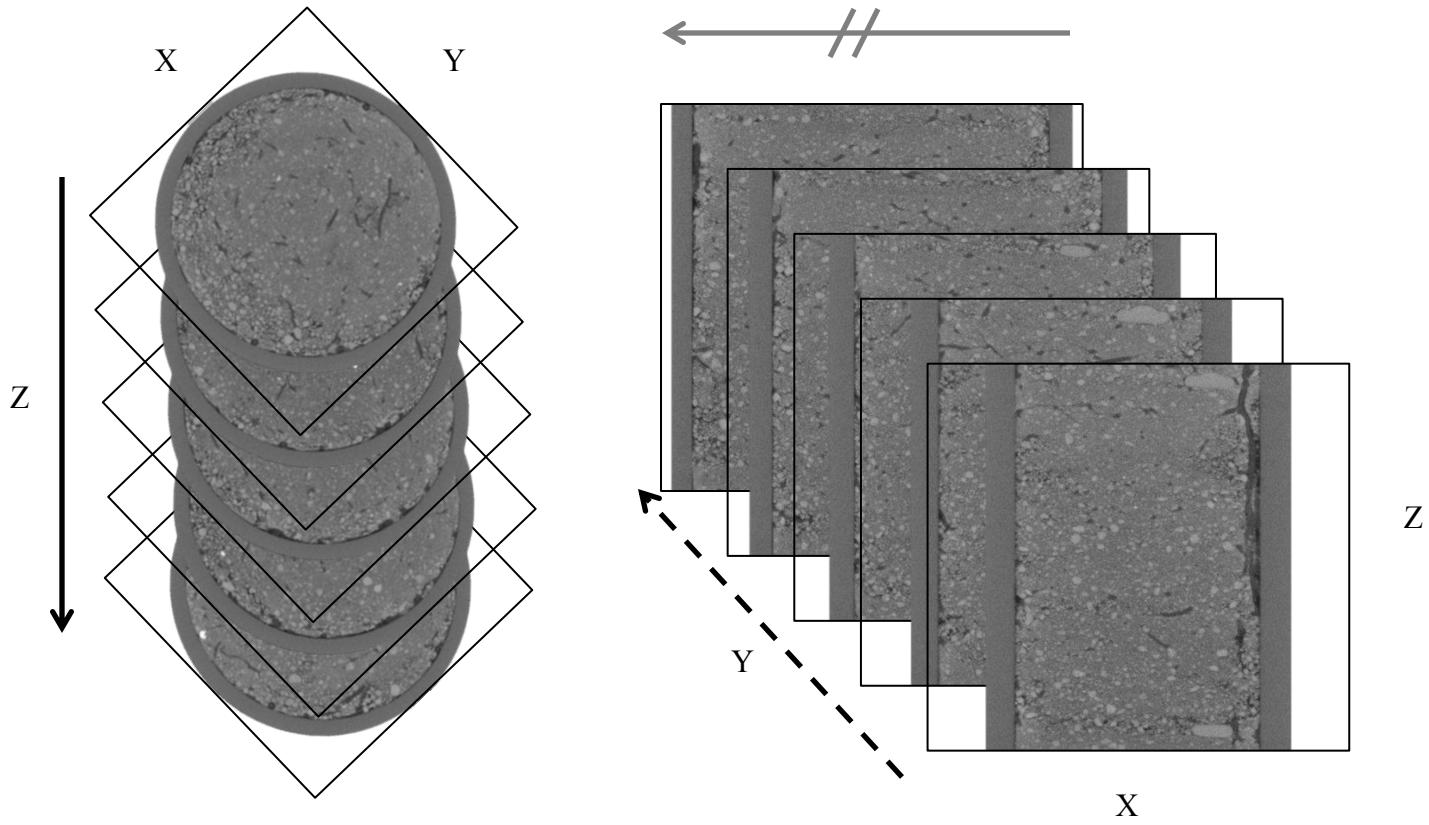

Figure 4.9| Manual segmentation procedure scans through a series of sequential slices manually identifying the tubular and continuous structures with lower grey values than the background soil. (Left) The primary approach is to view the XY plane and traverse though the volume, slice by slice in the Z direction (solid arrow -top to bottom). (Right) The second step is to then view the XZ plane and traverse through each slice in the Y direction (broken arrow -side to side). It was not deemed necessary to repeat in the X direction by viewing the ZY plane as few additional roots were identified in manner.

Due to the considerable time investment required for the manual segmentation method (Flavel *et al.* 2012), a more automated process was sought to increase processing capacity. The features that were used to identify the root manually (i.e. grey values, shape and connectivity between slices) provided the basis for initial segmentation algorithms. As described by Mairhofer *et al.* (2012), there are two dominant approaches to segmenting the root system from tomographs; the 'top down' and the 'bottom up' approach. The first describes methods that specifically select the root system voxels from the rest, and the later refers to protocols that use various filters to sequentially exclude all non-root components from tomographs. The later was selected as a starting point due the large range of existing algorithms that have not been applied to this challenge and which afford opportunity to rapidly develop a satisfactory processing method. In addition, there are fundamental limitations to existing 'top down' approaches, which will be discussed below.

The ‘bottom up’ methods often use some form of thresholding protocol based on grey scale values as an initial step. For the reasons previously discussed and widely reported, grey values alone were insufficient for segmentation and resulted in significant misclassification of non-root voxels. There have been several approaches to the general thresholding procedure including simple thresholding (Gregory *et al.* 2003), bi-level thresholding (Lontoc-Roy *et al.* 2006; Perret *et al.* 2007) or probability based per voxel classification using mixture modelling or similar statistical methods (Jassogne 2008; Tracy *et al.* 2011; Tracy *et al.* 2010). However, all have reported deficiencies of these methods alone or have provided algorithms for further filtering to improve output quality (Mairhofer *et al.* 2012; Mooney 2002). Binary threshold data (albeit susceptible to noise, PVE and incorrectly identifying similarly attenuating substances) provides an entry point into the plethora of implemented geometric filters for binary data. It should be noted that this ‘bottom up’ approach is susceptible to cumulative errors (Mairhofer *et al.* 2012) and consequently the cleanest results are often generated by the least possible operations.

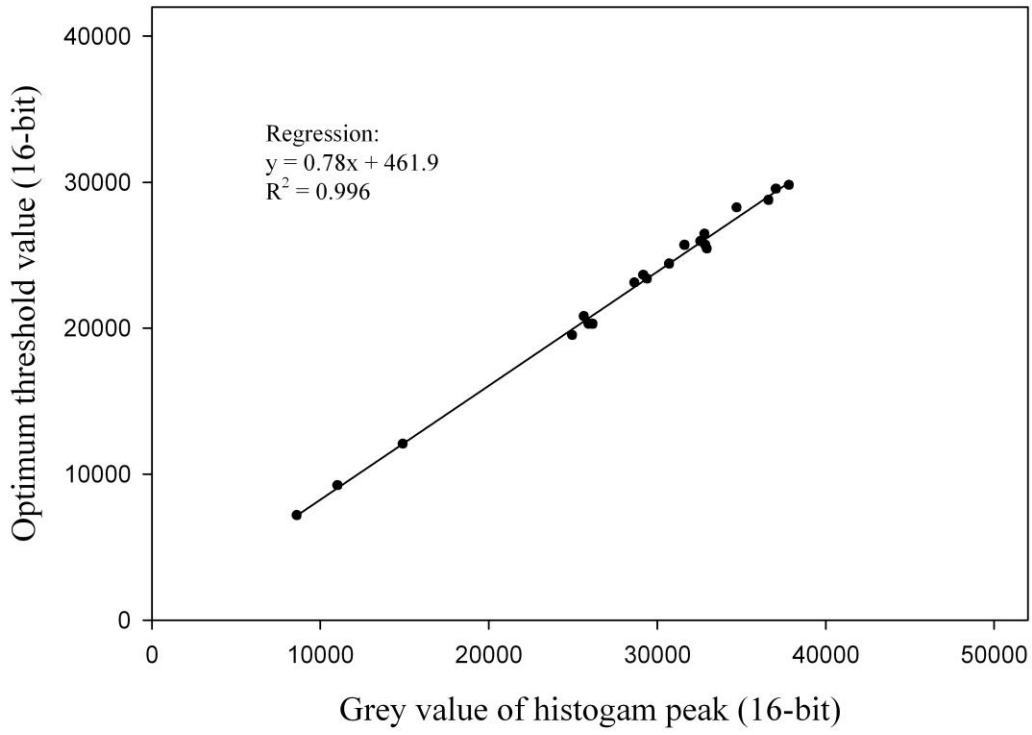

Figure 4.10| Calibration of the most appropriate threshold value relative to the peak value identified by Image J macro. Optimum threshold values were manually determined to segment all of the root system while minimising misclassification of non-root voxels. The strong relationship ($R^2 = 0.996$) indicates the consistent shape (variance) of the histogram despite fluctuations in peak value caused by sample composition.

The selection of the voxels that fall within the 'root' portion of grey values provides an appropriate starting point in developing an automated method, with a heavy reliance on post-thresholding morphological filters. It was necessary to find an automatic approach to identify the most appropriate threshold value, which would isolate the root voxels with as little other voxels as possible. Given the uniformity typically observed for the scan histograms within a consistent experimental design, it was expected that the ideal threshold value would be closely correlated to dominant histogram features, such as the mode (peak attenuation) grey value of the soil. To test this, 20 replicates of a Ferrosol soil (Isbell 2012) were placed in 30mm diameter PVC pots (260mm high) in which wheat was grown for 28 days. The root zone was scanned using the GE-Phoenix V|tome|xs with an isotropic voxel side length of 68.6μm with previously determined optimal X-ray tube parameters (180kV, 120μA, 0.125 mm Cu Filter, 1250 projections using constant rotation CT method, 200ms aquisition time). The tomographs were reconstructed with 16-bit depth and following import into Image J, the mode of 'soil' grey values (the highest peak of the histogram) was identified automatically using a custom built macro (Appendix 4). The most appropriate threshold value for isolating 'root' voxels was manually determined using the Image J "Threshold" tool (with "Over /Under" and "Stack histogram" settings). Figure 4.10 indicates a strong (R^2 =0.996) relationship between the soil mode grey value and the ideal threshold. This relationship suggests that despite the variance observed in the mode grey value (caused by different scan contents), the histogram is uniform relative to that peak value. The relationship is described by:

$$y = 0.78x + 461.9$$

Where y is the ideal upper threshold value for segmenting roots and x is the mode of the soil grey value. This relationship provides a mechanism for predicting the ideal upper threshold value based on a rapid and easily measurable histogram feature. This method was implemented in Step D and E (Figure 4.2) in the RootOne design process. For Step D in particular, the histograms of tomographs were aligned to a common value. Consequently, the mode of the 'soil' fraction was constant for all samples the ideal threshold value was also constant and could be 'hard coded' to

reduce computational demands. This value will be specific to each experimental design and will require calibration.

Following thresholding, morphological filters are commonly used to remove misclassified voxels (Kaestner *et al.* 2008). Inspired by the 'shape' parameter from the manual segmentation process and the method proposed by Pierret *et al.* (1999a), a shape filter based on the 'Analyse Particles' Image J menu was trialled to identify roots on the basis of their conformity to circular or cylindrical properties. This attempt was unsuccessful due in part to the comparable geometry of connected pore space. In addition, much of the root length is contributed by roots approaching the detection limit (~2 voxel diameter) and as such are often represented by as little as 4 voxels in transverse section. As a result, the circularity of such features is often obscured by small contributions of noise, PVE or orientation. This observation is consistent with the findings noted by Pierret *et al.* (1999a) using a similar technique.

The connectivity and the continuity of roots between slices (also observed during manual segmentation) is a commonly exploited characteristic to distinguish roots from pore space and other edaphic features. There are numerous derivations of morphological filters (Mooney *et al.* 2012) ranging from flood fill, restricted dilation or region growing to more complex methods such as level sets (Flavel *et al.* 2012; Jassogne 2008; Kaestner *et al.* 2006; Lontoc-Roy *et al.* 2006; Mairhofer *et al.* 2012; Perret *et al.* 2007; Tracy *et al.* 2011; Tracy *et al.* 2012). Most of these methods are reviewed in greater detail by (Mooney *et al.* 2012) and will not be explicitly reviewed here. In general the connectivity algorithms are susceptible to the presence of nearby pore space or PVE around roots producing 'breakouts'. In this instance, the algorithm expands into areas of similar attenuation and misclassifies these non-root voxels (Perret *et al.* 2007) (e.g. Figure 4.11 D). A further problem is that connectivity algorithms fail to detect root fragments that are disconnected from the seed (Mooney *et al.* 2012; Perret *et al.* 2007). In an effort to remove the large amount of small-disconnected voxels present in the Step B (Figure 4.2) a connectivity filter was used (employing the Image J- FIJI native "Find connected regions" plug-in). This process involved isolating the largest connected regions and manually determining whether the fragments represented roots. The process successfully cleaned the images however did increase the variance observed between the CT and conventional root

washing methods (see Chapter 5 for more details). In most of the literature above, connectivity algorithms are used following thresholding (either probability or grey value based) to filter the result and reduce voxel misclassification. The relative success of these methods are highly sample dependent and can vary substantially.

In some instances connectivity algorithms are applied in a "top down" approach where the root system is specifically identified from the remainder of the scan. Recently, the program RooTrak (Mairhofer *et al.* 2012) was released (open source) and is an implementation of the level set and JS divergence protocol which 'tracks' the root through sequential stacks based on root connectivity. RooTrak was trialled for its possible application to the current experimental setup. A small subsection (slices 320-480) of the scans described above (Section 4.2.3) was analysed, first using manual local adaptive threshold segmentation in VG StudioMax 2.0 (Figure 4.11 A) and then using RooTrak (Figure 4.11 B-D). A matrix of settings were evaluated using 21 combinations of '*Curvilinear*' (values 0.15, 0.2 and 0.25) and *'Similarity'* parameters (values 0.15, 0.2, 0.25, 0.26, 0.27, 0.28, 0.29 and 0.3), three of which are displayed (Figure 4.11). Thirteen common seed points were used in all cases to initiate the tracking algorithm. The novel algorithm is robust and effective for the segmentation of large primary roots but is less efficient at isolating branches. Since the algorithm progresses in a down wards trajectory, the current implementation is not able to follow branches that trend upward at any point. In addition the algorithm is sensitive to the input parameters. When the 'Similarity' parameter (related to grey value tolerance) is increased to improve detection of branches, 'breakouts' are common (Figure 4.11 D).

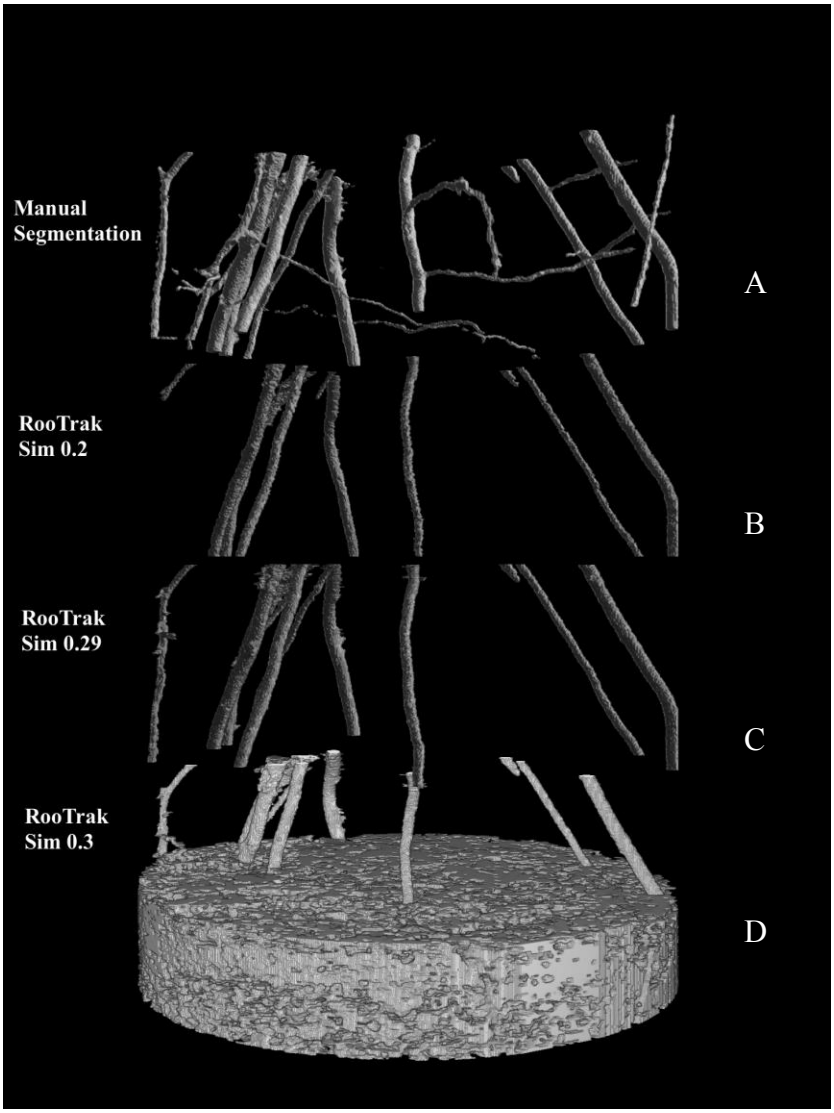

Figure 4.11| Trial of available automatic segmentation program RooTrak. (A) Manual segmentation method comparable to Step C Figure 4.2 using Adaptive local thresholding. (B,C,D) RooTrak method (based on level sets) using 15 identical seed points. (B,C,D) Represent three examples of RooTrak setting tested. The 'Curvilinear' parameter was set to 0.2, while the similarity (grey value threshold) parameter was set to 0.2, 0.29 and 0.3 respectivly. The large mass in (D) represents the algorithm 'breaking out' of the root system into the partial volume effect and soil matrix. The lack of branches segmented RooTrak represents a fundamental limitation of the method in its current stage of development.

The 'tubeness' algorithms also exploit the longitudinal nature of the root system to identify roots. Originally proposed by Sato *et al.* (1998) and soon after improved by Frangi *et al.* (1998), the method was developed for use in medicine for segmenting blood vessels from medical imagery. The algorithm uses the eigenvalues of a 3D Hessian matrix to produce an index of 'vessel likelihood'. Both of the techniques have been implemented into Image J- FIJI as 'Tubeness' and 'Frangi Vesselness' plugins respectively. The algorithms were trialled for implementation in automated method, producing comparable images in the tested datasets. The Frangi *et al.* (1998) implementation required approximately 4 times greater processing time (16.5 min compared to 4 min) as compared to the Sato *et al.* (1998) method when processing the same 1297 slice binary threshold stack. Therefore, the latter was adopted for the first phase of RootOne methodology (Figure 4.2 Step D) and was the only filter used

following thresholding. Recently Schulz *et al.* (2012) have included the Frangi *et al.* (1998) method in a comparable segmentation algorithm designed to isolate root structures from MRI imagery.

The presence of small-disconnected regions identified by the 'Tubeness' plugin and the representation of large primary roots as hollow tubelike vessels created complications for extracting root morphological data (particularly by skeletonization -discussed in Section 4.3). In an effort to improve the quality of the images segmented by this process, additional filtering steps were included in the final developmental stage (Figure 4.2 Step E). First, the values from the 'Tubeness' algorithm were scaled from 1-11 in 32-bit format. These were multiplied with the inverted original grey values of the threshold, which had been similarly scaled (value range 1-11 in 32-bit format). Higher attenuation pores (predominantly PVE voxels) were therefore assigned a lower grey value. The resulting image provided an index of values that conformed to the Sato *et al.* (1998) 'tubeness' conditions and biased any pore space that was extracted (by the 'tubeness' algorithm) with lower values by including the inverted tomograph grey scale values. In an effort to further remove the smaller connected pore space, a 3D distance transform of the original threshold volume was created. The "Distance Transform 3D" plug-in for Image J-FIJI is an implementation of the method proposed by Borgefors (1996) and assigns a value to each voxel relative to the shortest distance to a 'non-root' voxel. This process attributes lower values to thin, small and disconnected pore space. When this index is scaled as before (range 1-11, 32-bit depth) and multiplied with the previous composite image, the result is a volume with a continuum of grey values. In this image higher values represent tube-like structures with thicker or continuous morphology that have moderate x-ray attenuation coefficients (Figure 4.3 E and Ei). A simple thresholding procedure is then able to remove the bulk of the pore space producing cleaner images with solid filled roots for appropriate morphological analysis.

Segmentation of root volumes from X-ray CT imagery remains a difficult proposition (Mooney *et al.* 2012). The overlap in attenuation coefficients produced by similar substances (e.g. organic matter), the PVE, coupled with the discontinuous reality of the scanned root system (as a result of resolution limitations) and the morphological

similarities between roots and connected pore space limit the capacity of automated programs to consistently extract root systems from soil tomographs. In the tradition of many previous approaches the above methodology seeks to exclude all 'non-root' components from tomographs using a series of 'filters' to produce a 3D representation of the root system. Despite the challenges with segmentation protocol, progress is apparent with recent releases of segmentation programs (Mairhofer *et al.* 2012; Tracy *et al.* 2011) and improvements in acquisition and processing technology making image quality and complex algorithms more practical. For some time segmentation of root systems has provided the primary restriction to using tomography for root studies. As the pressure on this hurdle eases, the focus is shifting to develop the next step in the process, extracting useful root system morphological parameters.

4.3 Extract root system morphological features

Despite a substantial history of root zone analysis using X-ray CT (Mooney *et al.* 2012), only recently have technological developments enabled large and complex root systems to be captured. Understandably, the development of programs capable of analysing rooting structures for morphological characteristics has lagged somewhat behind the remainder of the technology. The rising interest in a range of phenotyping platforms has encouraged the development of software capable of extracting significant 3D morphology traits from root systems grown in transparent media (Clark *et al.* 2011; Iyer-Pascuzzi *et al.* 2010). Recently Clark *et al.* (2011) published the development of RootReader3D software for such an application which calculates 27 different root traits of varying physiological relevance. However, at the time of writing this software is not yet publically available. Perret *et al.* (2007) presented some of the first examples of simple morphological analysis of root systems from CT imagery, describing the early branching, root length and tortuosity of young chickpea (*Cicer arietinum* L.) seedlings. Since then more complex root systems have been captured using 3D techniques however the analysis performed on such imagery often falls short of the potential that the 3D platform affords.

Frequently, image-processing techniques developed for other applications are implemented for root morphological analysis as a proxy for direct root architectural measurement. In some situations this is appropriate, however there are many examples where an available method is reported with relatively little meaning and where traditional root system measures would be more appropriate. For example, convex hull measurements are commonly reported (Clark *et al.* 2011; Mairhofer *et al.* 2012; Tracy *et al.* 2012) as a proxy soil volume explored when an approach commonly applied in root system modelling such as root zone dilation (Lynch *et al.* 1997; Rubio *et al.* 2001) would provide a more direct and realistic measure. In a similar fashion, 'centroid' values (approximating the centre of mass of the root system) have been used to indicate the differences in average root distribution (Tracy *et al.* 2012). Here root length density would provide a more direct descriptor of root distribution and would remain unbiased by the high presence of voxels at the crown of the plant. In a similar fashion, root volume has been used as a proxy for root length, however, the variance reported in volume measures when compared to destructive quantification is substantial (Tracy *et al.* 2011). This is unsurprising as the measurement of root diameters from CT scans is highly inaccurate (Mooney *et al.* 2012) while the root diameter is less than 15 voxels (Cnudde 2005). This is the result of the PVE and subsequent grey scale gradient produced at phase boundaries. Therefore, given the significant contribution of root diameter to root volume, large variation is to be expected in root volume measures for fine roots. For the application of X-ray CT to root system phenotyping, root system traits with a physiological basis should be the target of direct measurement such as root length (distribution and extension rates), branching (number and spatial distribution), growth angles, root system widths and depths (where not constrained by the pot) amongst many others.

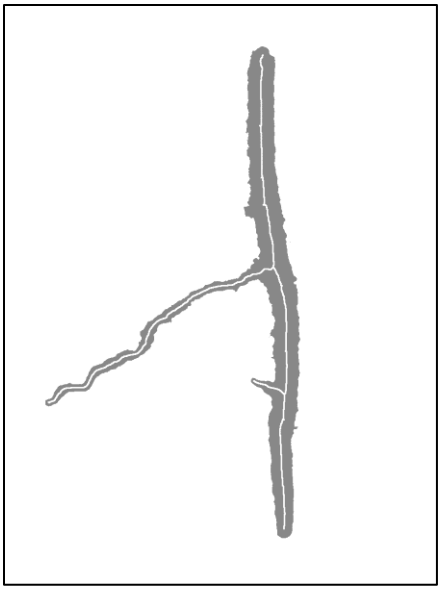

Figure 4.12| Skeletonize function in 2D. The skeletonise function (Lee *et al.* 1994) sequentially removes exterior layers of the 'root' until the centroid (white) is identified. Voxel counting of the centroid line can provide accurate information about root length and tortuosity.

Root length was originally targeted as a highly descriptive and verifiable root morphological trait that was reflective of conventional root methods and useful for characterising root system architecture. When applied to segmented root volumes, skeletonising algorithms remove sequential exterior layers of 'root' voxels until the centroid of the root is identified (Figure 4.12). With the voxel size calibrated, voxel counting can be used to determine the length of roots or root branches (Lontoc-Roy *et al.* 2006). In the initial stages of development (Figure 4.2 Step B) the native Image J-FIJI plug-in "Skeletonize (2D/3D)" and "Analyze Skeleton (2D/3D)" (an implementation of Lee *et al.* (1994)) were used to generate a list of all branch lengths in the root volume. These branch lengths represented the skeletonised length along the root path between two branches, or in terminal branches between the branch and the tip of the root. In the initial stages of development total root length was determined by summing the "Analyze Skeleton (2D/3D)" output. The strong correlation to destructive measures discussed in Section 5.4.2 and again in Section 6.3 confirm the validity of the skeletonise function for root length measurement.

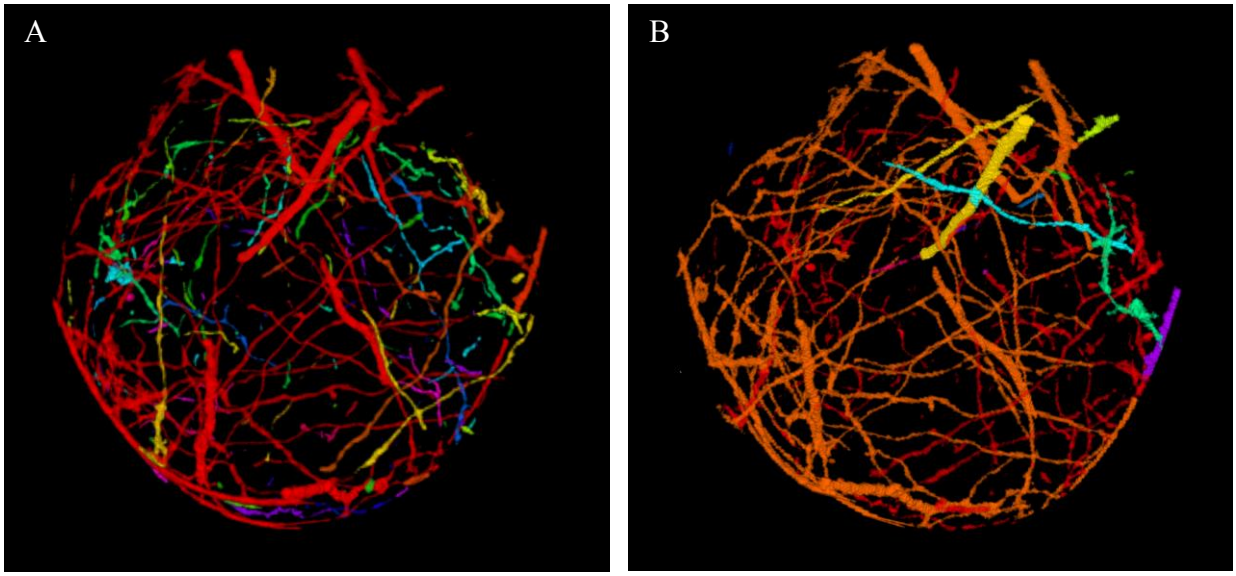

Figure 4.13| Number of connected regions before (A) and after (B) a two iteration dilation operation to re-join disconnected volumes. Unique colours represent disconnected volumes, where a greater number of colours present (A) indicates a greater number of disconnected regions. The above segmented root volume represents ~20mm removed from the mid section of a scanned pot with high root density. The dilation operation reconnected isolated fragments reducing the number of root fragments from 286 to 181.

In later stages of development (Figure 4.2 Steps C-E), an automated macro was developed to measure length, root length density, branching and branching density (Figure 4.1). This macro first uses a dilation operation to re-join disconnected root fragments that are separated by less that 2 voxels, in a similar fashion to the method proposed by Kaestner *et al.* (2006). During the segmentation process, small discontinuities in roots can become present due to star artefacts or sub-perfect segmentation algorithms. In the interest of maintaining root architectural integrity, a dilation operation can re-connect roots that are separated by 2 voxels or less. This significantly reduces the number of root fragments present in images. For example, a 3D dilation operation (2 iterations) reduced the number of small root fragments in a small sub-sample from the centre of a pot by 32% (Figure 4.13). Following dilation the root volume is skeletonised using the Lee *et al.* (1994) protocol and root centroid voxels are counted in a slice by slice manner. From this data the total root length and root length density data can be calculated. The "Analyze skeleton" function is then used to classify skeleton voxels with 1, 2 and 3 nearest neighbours, relating to tips, root length and root branch sites respectively (See Figure 6.2). The branching density can then be generated in a similar fashion. While for the purposes of the following experimentation, root length density and branching density data are calculated in a slice-by-slice (top down) manner, there is significant potential to generate 3D density maps at any scale. In this manner the spatial distribution of root architectural characteristics length and branching can be measured at high resolution. This has been demonstrated in Chapter 6.

The 3D nature of CT analysis not only enables the spatial distribution of root system traits to be analysed, but presents a almost unique opportunity to measure architectural features such as branching or growth angles. There is very little empirical evidence available for characteristics such as branching angles *in situ* due to the constraints of the soil medium. Measuring these characteristics without the use of 3D imaging if possible, is often laborious, destructive or requires 'artificial' media (Hargreaves *et al.* 2009). Due to the difficulties in directly measuring these characteristics, they are regularly modelled and, if altered, have been shown to significantly affect the nutritional resources available to the plant (Ge *et al.* 2000). The final macro in the toolbar (Figure 4.1) has been designed to extract branching angle data from tomographs. The method superimposes the skeletonised information

(with branching points labelled) onto the root volume stack (Figure 4.14). The user is able to scan through the images and with three 'clicks' can identify the main root, vertex (branch point) and branch direction. The macro then records the angle between the three voxels. The resultant angle (between the bottom of the root and the downstream side of the parent) was selected as the standard measure as this is the angle commonly used in root system branch angle modelling (Ge *et al.* 2000; Lynch *et al.* 1997).

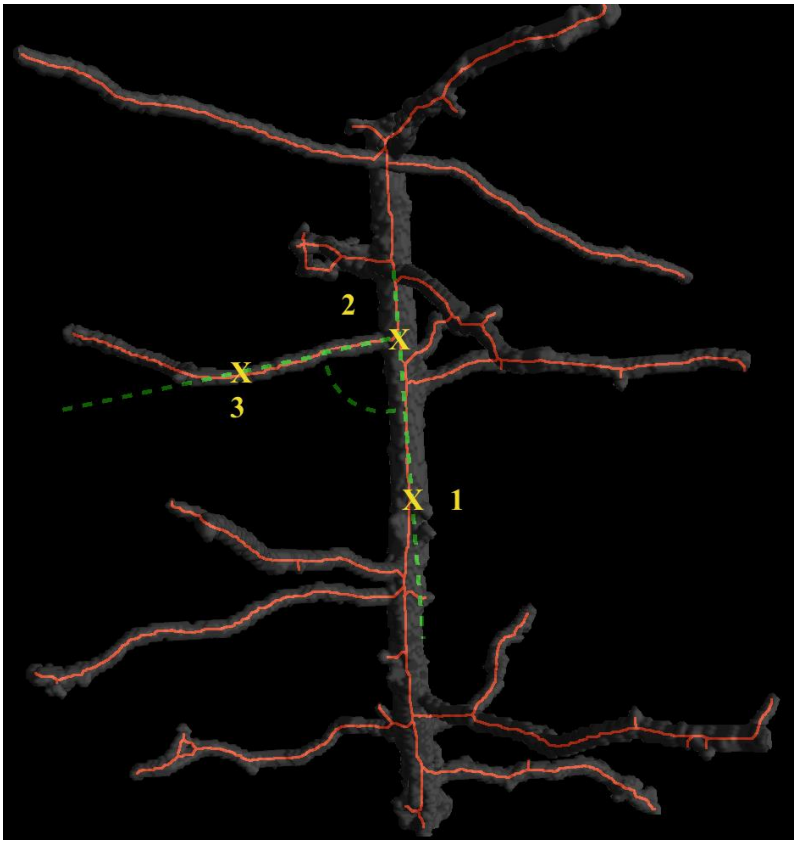

Figure 4.14| Three dimensional visualisation of the root branching angle tool. Root branch angle can be measured using thee points; along the parent root (1), at the branch vertex (2) and along the branch root (3). 3D root skeleton (red) is superimposed on the root segmentation (grey) and the angle calculated is indicated in green (broken line).

4.4 Conclusion

Technological development in X-ray CT instrumentation and computer processing has eased the historical pressure at the image acquisition stage of *in situ* root phenomics. Present systems are increasingly able to acquire images rapidly, at sufficient resolution and in adequate soil volumes to make phenomic or root morphological studies practical. The handling of the data created by high throughput systems has now become the rate-limiting step. The first challenge is in efficiently importing, correcting data for small acquisition fluctuations and combining scans to produce a continuous volume. With particular relevance for the UNE Micro-CT scanner (V|tome|xs), an image processing toolbar capable of rapidly importing, correcting grey values and stitching volumes together has been produced. This extends the plant sizes and soil volumes that can be scanned at high resolution by allowing multiple adjoining scans to be combined.

The second and perhaps greatest challenge lies in extracting the root system structure from a complex soil medium. The dense and porous nature of soil produces a range of attenuation values when scanned, some of which occur in the same value range as the root system. The PVE in particular, limits the utilisation of grey values alone to remove the root system from its surrounds. The challenges of removing roots from a pore and PVE voxel network that have similar grey values, shape and connectivity to the root system are formidable. While manual segmentation has yielded clean root volumes, highly correlated to destructive methods, the process is extremely laborious. During manual segmentation, three main characteristics were used to identify roots and proposed as possible characteristics to target in automation. Namely grey value, shape and root continuity between slices. Grey values and continuity characteristics have been exploited as part of a morphological filter to remove the non-root voxels from an initial thresholding operation. The 'RootOne' algorithm presented above has provided a cleaner segmentation result than is achievable with simpler thresholding methods and is automatic and rapid. The method includes the novel application of the 'tubeness' algorithm, originally designed to isolate blood vessels from medical scans. This helps preserve the integrity of fine roots that are often inadvertently discarded during segmentation. To date no highly robust segmentation program has been

proposed that is capable of identifying complex and fine root systems from X-ray CT scans. The current 'RootOne' method is no exception with some noise still clearly evident, however the algorithm is automated, rapid and capable of delivering basic root spatial distributions.

There is also a dearth of analysis packages capable of extracting useful RSA attributes from segmented volumes. In the absence of specifically relevant measures there have been several indirect measurements proposed. It is however, crucial to maintain a strong and direct relevance between the root system measurements recorded and root function. The toolbar outlined above includes methods to calculate root length, root length density and branching density (on a per slice basis) as well as branching angles. These measures have direct relevance to the uptake and efficiency of the root system in acquiring spatially heterogeneous nutrients such as P.

The development of a rapid and accurate method for the handling and analysis of large 3D root volumes represents significant progress in the technique. While further software development may be necessary, X-ray CT provides significant potential as a root phenotyping method to characterise root morphological responses to the edaphic environment.

Chapter 5 : Non-Destructive quantification of cereal roots in soil using high resolution x-ray tomography

The work contained in this chapter has been published in the *Journal of Experimental Botany*.

Flavel, R., Guppy, C., Tighe, M., Watt, M., McNeill, A., Young, I. (2012) Non-destructive quantification of cereal roots in soil using high-resolution X-ray tomography. *Journal of Experimental Botany* 63: 2503-2511

Chapter 6 : Quantifying *in situ* root plasticity and architecture in soil: phosphorus fertiliser responses

The work contained in this chapter was prepared for and has been submitted to *Nature* in the form of a *Letter*.

Flavel, R., Guppy, C., Watt, M., Tighe, M., Young, I.M (Submitted) Measuring plasticity in soil: sensitivity of roots to nutrient patches. *Nature*

Chapter 7 : General Discussion

Phosphorus nutrition continues to be one of the dominant limitations to global agricultural productivity. The continuing population growth, requirement for fertiliser grown products (Ingram *et al.* 2012) and the currently low use efficiency of many but particularly P fertilisers (~ 30%) (Manske *et al.* 2000; Vance *et al.* 2003) all support the call for greater nutrient acquisition efficiency in crop plants (Lynch 2007). As a highly immobile nutrient, P is typically heterogeneously distributed in the soil profile. In response to this phenomena, many plant species have adapted mechanisms for both local (Hodge 2004) and global (Bonser *et al.* 1996) root architectural adaption to improve P uptake efficiency. Similar responses have been observed with N however, the energetic advantage associated with morphological adaption for a nutrient both transient in location and time is questionable (Hodge 2004). While there has been significant work exploring the cellular and hormonal control mechanisms regulating the localised proliferation response (Linkohr *et al.* 2002; Malamy 2005; Ticconi *et al.* 2004), there remains significant question over the edaphic conditions required to trigger such a response (Robinson 2005).

The dearth of information available regarding the trigger conditions, the spatial specificity and the rate and magnitude of proliferation responses is largely due to the methodological challenges associated with measuring spatial and temporal root fluxes. Further complications arise when trying to replicate the complex chemical and physical characteristics commonly exhibited in the edaphic environment. With such challenges, it is logical that X-ray CT would be rapidly identified as a useful tool for imaging root systems *in situ* (Mooney *et al.* 2012). The spatially referenced and non-destructive nature of CT is highly valuable for quantifying the architectural characteristics of root systems that are otherwise difficult or impossible to attain (Hargreaves *et al.* 2009; Lontoc-Roy *et al.* 2006; Perret *et al.* 2007; Tracy *et al.* 2011) as well as changes through time (Tracy *et al.* 2011). Despite considerable interest in the technology, there are as yet no robust or standardised methods capable of automatically extracting root volumes cleanly from tomographs. One reason for the lack of consistency in research methods is the vast range of CT apparatus, experimental designs and soil types and conditions used in these experiments.

The optimal CT parameters and experimental design for any one circumstance are highly dependent on the experimental aims, the sample and the apparatus used to acquire images. As such it is difficult to define uniform settings or to produce tomographs of a standard quality for uniform post processing. Instead the 'optimal' parameters for a specific application must be determined by balancing a large number of dynamically related factors often producing a unique combination for a particular purpose. The process can be directed toward achieving the highest quality image with greatest contrast and use of the dynamic range as is possible. However, the resolution and contrast of the resulting tomographs are in dynamic equilibrium with capturing practical sample sizes, in reasonable scan times, at appropriate energy ranges (or radiation exposure) with minimal artefacts. More specific detail of the settings used and justification is presented in Chapter 4. The target should remain high quality tomographs, which have direct implication for the ease of post processing and quality of the output data.

The ideal of a rapid and robust phenotyping system for in situ screening of root systems (based on X-ray CT) is still early it in its development. Historically curtailed by the low throughput, low resolution technology previously available, there has been little demand for segmentation algorithms capable of digitally extracting root systems from tomographs. Advancing technologies and increased focus on the edaphic interactions are now placing pressure on methodology to quickly evaluate the 'hidden half' (Waisel *et al.* 1996) of the plant. At this stage in the technological development, three main computational challenges slow rapid post processing; rapidly combining multiple scans to increase the field of view, segmentation of the root system from tomographs and analysing the tomographs to produce pertinent root architectural information highly correlated to root function.

Resolution and sample size restrictions can be somewhat reduced by combining sequential scans of the pot. This process has been optimised for the present system allowing rapid import, correction for minor grey value fluctuations and 'stitching' adjacent scans into a seamless transition with the use of an Image J toolbar (Figure 4.1).

Imaging root systems using X-ray CT has substantial potential, but as with any method has corresponding limitations. Constraints to the detection and segmentation of the root system represent two major sources of error introduced when using the technique. At its most fundamental level X-ray CT uses the average attenuation of X-rays to image a 3D sample. This function invariably limits its applications to samples where the feature of interest is at least 2-3 times larger than the resolution in its smallest dimension. When imaging root systems, the fraction of the root system that can be detected by X-ray CT is therefore limited by the resolution of the scan. If not recognised as an assumption in the analysis, this can represent a major bias during interpretation. In many respects this function is not unique to X-ray CT. The same can be said of standard root analysis techniques such as root washing, where the finest fraction of the root system is often underrepresented depending on the size of the sieves used (Gregory 2006). This is an important consideration given the proportionally greater contribution of fine roots to root system function. In the data presented, roots with an average diameter of greater than 250 μm and 200μm for Chapters 5 and 6 respectively were segmented and analysed. Conventional measurements of the root system indicated that the young wheat plants had roots down to 140μm in diameter. This discrepancy could explain some of the lack of response observed to the P band in Chapter 5. Despite the current imaging limitations to observe the finest fraction of the root system, the rate of technological improvement in detector dynamic range, sensitivity and resolution would indicate that this might be possible in the near future.

Segmentation of the voxels representing 'roots' from the remainder of the volume remains a difficult proposition. In part this is because grey values typical of the root system are also commonly assigned to non-root voxels with a) part soil, part air composition or b) substances that have coincident attenuation coefficients as the root (e.g. plastics, water or organic matter). The challenges are simply that grey value alone does not acceptably distinguish the root system from other material and thus requires morphological filters, which help to distinguish the root system by its 'shape'. A method for manually segmenting the root system from tomographs to produce high quality images is detailed in Chapter 4. This method is also used in Chapters 5 and 6 correlating well with conventional destructive measures for root

length (Figure 5.4 and Figure 6.1). Notably, the same gradient is recorded with both methods, indicating a systematic underestimation of root length by approximately 8%. This is consistent with other work using similar techniques on much smaller root systems (Gregory *et al.* 2003; Perret *et al.* 2007). It addition a method is documented for an automatic and rapid algorithm which sequentially removes the non-root voxels from an originally over-segmented image. While somewhat noisier than manual segmentation, the technique is rapid and automatic allowing more coarse measures such as spatial distribution of RLD to be quantified.

A final challenge in image processing is the lack of standardised packages or measures to characterise root architectural traits from segmented volumes. Presented in the Image J toolbar (Figure 4.1) is a simple protocol for automatically calculating root length, root length density and branching density (on a per slice basis) from segmented volumes. With some user input the branching angles can also be calculated. In the further development of RSA analysis protocol, it is crucial to maintain a strong and direct relevance between the root system measurements measured and root function. These measures have direct relevance to the uptake and efficiency of the root system in acquiring spatially heterogeneous nutrients such as P. It is expected that these simple per slice measures could easily be converted into 3D RLD or branching density maps, providing more information of nutrient uptake or root system response to point source nutrient additions such as granular fertilisers.

Chapter 5 represents a methodological study with three primary objectives. First was to determine the whether high resolution X-ray CT had the capacity to accurately measure root length as compared to the conventional method using root washing, a flat bed scanner and WinRhizo. As discussed above the comparison indicated a systematic underestimation and a strong positive correlation. During the course of the experimentation the plants were exposed to a series of 5 separate scan dates, with any one part of the pot exposed to a cumulative total of 21 mins radiation over an 18day period. Comparison with un-scanned treatments confirmed that there was no detectable damage to the root system in any of the architectural parameters measured. The final objective was to evaluate the suitability of the technique for high throughput root system studies. It was concluded that the scan time required for each sample was sufficiently rapid to make replicated and even small screening

experiments plausible, however the time taken for manual image segmentation was prohibitive. As a result investigations into automated or semi-automated segmentation methods was stimulated. In addition to the stated aims, the lack of root system response to P additions indicated water management and soil texture required review. Using light textured soils (90% sand 10% ferrosol soil w/w) with moisture controlled using a tension table in tall pots, resulted in water filled pores at the base and a dry surface. In subsequent trials, pure ferrosol soil was used as the moisture release curve exhibited less significant extremes at the top and bottom of the pot and the soil provided greater contrast against the root.

Having implemented improvements in the experimental design and automated RSA analysis from segmented volumes, Chapter 6 describes an experiment exploring wheat root plasticity or ability to respond to banded P. The architectural mechanism for the enabling the plasticity was also explored. After 28 days wheat roots exposed to a moderate concentration of P (~8.5μM P) in a band exhibited a three-fold increase in RLD and two-fold increase in branching density. Subsequent analysis of the spatial distribution of branching and root length indicated that branching density increased highly specifically to the region of available P (within 0.068mm of band boundaries) while branching density increased 2mm below the top of the band but continued past the lower boundary of the band. It is therefore likely that the branching response is up-regulated at the site of available P (highly localised), and that branches initiated in this region extend rapidly but are not down-regulated as specifically as the branching response. Root length measures also correlated well with conventional root length methods. The variance observed in Chapter 6 is significantly lower than that observed in Chapter 5 as reflected in the R^2 values (0.68 and 0.96 for Chapter 5 and 6 respectively). This is due connectivity filter used in the prior experiment to remove water filled pores from the final segmented volume. This filter also had the effect of removing disconnected root fragments.

In contrast to the stark plasticity exhibited by branching and root length densities, branching angle did not exhibit any global or localised plasticity in response to P nutrition. Despite the lack of response in this genotype, the precedent for variable growth angle response to P nutrition demonstrated by Bonser *et al.* (1996) in

common bean suggest that further inquiry should be made into other wheat genotypes. Root growth angle is also an important factor in root system modelling and highly influences the volume of soil explored, inter-root competition and P uptake (Ge *et al.* 2000). The CT technique demonstrated here provided an ideal method to conduct surveys for genetic variance and to quantify commonly observed branching angles for which empirical evidence is largely unavailable.

7.1 Further Research

This project has advanced our understanding of the spatial scale at which wheat root morphological adaptions to heterogeneous P supply occur *in situ* and has identified the root architectural mechanism for this response. This thesis demonstrated the potential usefulness of X-ray CT for the study and understanding of the root architectural plasticity as well as identified the lack of development in automated segmentation methods that has limited high throughput root system analysis using this technique. However, given the current capacity of X-ray systems for rapid scanning, some further development of segmentation software will drastically improve the capacity to study root architecture regulation mechanisms and the variation in root morphological adaptions.

In particular, the highly spatially specific nature of the root proliferation response to banded P demonstrated in Chapter 6, suggests a tightly regulated control mechanism. The trigger conditions required to stimulate this response remain a mystery and could provide indicators as to the regulation mechanism. Current suggestions include a critical threshold cytosolic P concentration, a tipping point change in external P concentrations (critical gradient) or suggest that higher a regulation mechanism exists to ensure that root growth is proportional to the concentration of available P (Jackson *et al.* 1989; Robinson 2005). X-ray CT provides an ideal platform to test these hypotheses with a capacity to spatially determine the point of morphological response in 3 dimensional space.

A further point of inquiry is the timing of the proliferation response and at what rate root length density increases around a fertiliser granule. This has implications for the

efficiency and uptake of granulated P fertiliser applications as well as early season plant nutrition. Time sequence studies could also ascertain the rate of lateral branch extension, providing information about whether the control of extension rates is related to P concentration, as is branching density.

With global pressure increasing for enhanced agricultural productivity and the availability and cost of fertiliser products set to reduce grower access, it is clear that improving crop species nutrient acquisition efficiency is a key target for future breading. Root system architecture has a significant influence on the resources available to the plant (Lynch 2007). X-ray CT provides a tool capable of rapidly and non-destructively quantifying root architectural responses to edaphic conditions and therefore has value for both mechanistic studies and in the field of genetic improvement through phenomics.

References

Al-Ghazi Y, Muller B, Pinloche S, Tranbarger T, Nacry P, Rossignol M, Tardieu F, Doumas P (2003) Temporal responses of *Arabidopsis* root architecture to phosphate starvation: evidence for the involvement of auxin signalling. *Plant, Cell and Environment* **26**, 1052-1066.

Amin M, Chorley R, Richards K, Bachel B, Hall L, Carpenter T (1993) Spatial and temporal mapping of water in soil by magnetic resonance imaging. *Hydrological Processes* **7**, 279-286.

Anderson S, Hopmans J (1992) 'Tomography of soil-water-root processes.' (Soil Science Society of America: Madison, Wisconsin, USA)

Aravena J, Berli M, Ghezzehei T, Tyler S (2011) Effects of root induced compaction on rhizosphere hydraulic properties- X-ray microtomography imaging and numerical simulations. *Environmental Science and Technology* **45**, 425-431.

Aylmore LAG (1993) Use of computer-assisted tomography in studying water movement around plant roots. *Advances in Agronomy* **39**, 1-54.

Bates T, Lynch J (2001) Root hairs confer a competitive advantage under low phosphorus availability. *Plant and Soil* **236**, 243-250.

Bengough A, Bransby M, Hans J, McKenna S, Roberts T, Valentine T (2006) Root responses to soil physical conditions; growth dynamics from field to cell. *Journal of Experimental Botany* **57**(2), 437 -447.

Bonser A, Lynch J, Snapp S (1996) Effect of phosphorus deficiency on growth angle of basal roots in Phaseolus vulgaris. *New Phytologist* **132**, 281-288.

Borch K, Bouma T, Lynch J, Brown K (1999) Ethylene: a regulator of root architectural responses to soil phosphorus availability. *Plant, Cell and Environment* **22**, 425-431.

Borgefors G (1996) On digtal distance transforms in three dimensions. *Computer Vision and Image Understanding* **64**, 368-376.

Bouckaert L (2012) Dependency of organic matter decomposition on soil pore network structure as revealed by X-ray micro CT. Ghent University, Belgium,

Breiman L, Friedman J, Olshen R, Stone C (1984) 'Classification and Regression Trees.' (Wadsworth)

Bumb B, Baanante C (1996) The role of fertiliser in sustaining food security and protecting the environment to 2020. In 'Food, Agriculture, and the Environment

Discussion Paper 17.' (International Food Policy Research Institute: Washington, D.C. USA)

Burkitt L, Moody P, Gourley C, Hannah M (2002) A simple phosphorus buffering index for Australian soils. *Australian Journal of Soil Research* **40**, 497-513.

Caldwell M, Dudley L, Lilieholm B (1992) Soil solution phosphate, root uptake kinetics and nutrient acquisition: implications for patchy soil environment. *Oecologia* **89**, 305-309.

Capowiez Y, Pierret A, Daniel O, Monestiez P, Kretzschmar A (1998) 3D skeleton reconstructions of natural earthworm burrow systems using CAT scan images of soil cores. *Biology of Fertile Soils* **27**, 51-59.

Capowiez Y, Pierret A, Moran C (2003) Characterisation of the three-dimentional structure of earthworm burrow systems using images analysis and mathematical morphology. *Biology of Fertile Soils* **38**, 301-310.

Carlson W (2006) Three-dimensional imaging of earth and planetary materials. *Earth and Planetary Science Letters* **249**, 133-147.

Carminati A, Vetterlein D, Weller U, Vogel H, Oswald S (2009) When roots loose contact. *Vadose Zone Journal* **8**, 805-809.

Clark R, MacCurdy R, Jung J, Shaff J, McCouch S, Aneshansley D, Kochian L (2011) Three-dimentional root phenotyping with a novel imaging software platform. *Plant Physiology* **156**, 455-465.

Cnudde V (2005) 'Exploring the potential of X-ray tomography as a new non-destructive research tool inconservation studies of natural building stones.' (Ghent University: Ghent)

Colwell J (1963) The estimation of phosphorus fertiliser requirements of wheat in southern New South Wales by soil analysis. *Australian Journal of Experimental Agriculture and Animal Husbandary* **3**, 190-198.

Cordell D, Drangert J, White S (2009) The story of phosphorus: global food security and food for thought. *Global Environmental Change* **19**, 292-305.

Crawford J, Deacon L, Grinev D, Harris J, Ritz K, Singh B, Young I (2012) Microbial diversity affects self-organization of the soil-microbe system with consequences for function. *Journal of the Royal Society Interface* **9**, 1302-1310.

Culligan K, Wildenschild D, Christensen B, Gray W, Rivers M, Tompson A (2004) Interfacial area measurements for unsaturated flow through a porus medium. *Water Resources Research* **40**, W12413.

De Smet I, Signora L, Beeckman T, Inze D, Foyer C, Zhang H (2003) An abscisic acid-sensitive checkpoint in lateral root development of Arabidopsis. *the Plant Journal* **33**, 543-555.

Desnos T (2008) Root branching responses to phosphate and nitrate. *Current Opinion in Plant Biology* **11**, 82-87.

Dhondt S, Vanhaeren H, Van Loo D, Cnudde V, Inze D (2010) Plant structure visualisation by high resolution X-ray computed tomography. *Trends in Plant Science* **15**, 419-422.

Drew M (1975) Comparison of th effects of a localised supply of phosphate, nitrate, ammonium and potassium on the growth of the seminal root system, and the shoot, in Barley. *New Phytologist* **75**, 479-490.

Elyeznasni N, Sellami F, Pot P, Benoit P, Vieuble-Gonod L, Young I, Peth S (2012) Exploration of soil micromorphology to identify coarse-sized OM assemblages in X-ray Ct images of undisturbed cultivated soil cores. *Geoderma* **179-180**, 38-45.

Feeney D, Crawford J, Daniell T, Hallett P, Nunan N, Ritz K, Rivers M, Young I (2006) Three-dimensional microorganization of the soil-root-microbe system. *Microbial Ecology* **52**, 151-158.

Feldcamp L, Davis L, Kress J (1984) Practical cone-beam algorithm. *Journal of the Optical Society of America A-optics Image Science and Vision* **1**, 1984.

Fitter A (1987) An architectural approach to the comparative ecology of plant root systems. *New Phytologist* **106**, 61-77.

Flavel R, Guppy C, Tighe M, Watt M, McNeill A, Young I (2012) Non-destructive quantification of cereal roots in soil using high-resolution X-ray tomography. *Journal of Experimental Botany* **63**, 2503-2511.

Frangi A, Niessen W, Vincken K, Viergever M (1998) Multiscale vessel enhancement filtering. In 'Medical Image Computing and Computer-Assisted Intervention. Vol. 1496.' (Eds W Wells, A Colchester and S Delp) pp. 130-137. (Springer Verlag: Berlin, Germany)

Gahoonia T, Care D, Nielsen N (1997) Root hairs and phosphorus acquisition of wheat and barley cultivars. *Plant and Soil* **191**, 118-188.

Gahoonia T, Nielsen N (1998) Direct evidence on participation of root hairs in phoshorus (^{32}P) uptake from soil. *Plant and Soil* **198**, 147-152.

Gahoonia T, Nielsen N (2004) Root traits as tools for creating phosphorus efficient crop varieties. *Plant and Soil* **260**, 47-57.

Gahoonia T, Nielsen N, Joshi P, Jahoor A (2001) A root hairless barley mutant for elucidating genetic of root hairs and phosphorus uptake. *Plant and Soil* **235**, 211-219.

Gahoonia T, Nielsen N, Lyshede O (1999) Phosphorus (P) acquisition of cereal cultivars in the field at three levels of P fertilisation. *Plant and Soil* **211**, 269-281.

Ge Z, Rubio G, Lynch J (2000) The importance of root gravitropism for inter-root competition and phosphorus acquisition efficiency: results from a geometric simulation model. *Plant and soil* **218**, 159-171.

Godel B, Barnes S, Barnes S, Maier W (2010) Platinum ore in three dimensions: insights from high resolution X-ray computed tomography. *Geological Society of America* **38**, 1127-1130.

Grabarnik P, Pages L, Bengough A (1998) Geometrical properties of simulated maize root systems: consequences for length density and intersection density. *Plant and Soil* **200**, 157-167.

Grant C, Bittman S, Montreal M, Plenchette C, Morel C (2005) Soil fertiliser phophorus: effects on plant P supply and mycorrhizal development. *Canadian Journal of Plant Science* **85**, 3-14.

Grant C, Flaten D, Tomasiewicz D, Sheppard S (2001) The importance of early season phosphorus nutrition. *Canadian Journal of Plant Science* **81**, 211-224.

Greco M, Bell M, Spooner-Hart R, Holford P (2006) X-ray computerized tomography as a new method for monitoring Amegilla holmesi nest structures, nesting behaviour, and adult female activity. *Entomologia Experimentalis et Applicata* **120**, 71-76.

Gregory P (2006) 'Plant Roots: Growth, activity and interaction with soils.' (Blackwell Publishing Ltd: Oxford)

Gregory P, Bengough A, Grinev D, Schmidt H, Thomas WTB, Wojciechowski T, Young IM (2009) Root phenomics of crops -opportunities and challenges. *Functional Plant Biology* **36**, 992-929.

Gregory P, Hinsinger P (1999) New approaches to studying chemical and physical changes in the rhizosphere: an overview. *Plant and Soil* **211**, 1-9.

Gregory P, Hutchison D, Read D, Jenneson P, Gilboy W, Morton E (2003) Non-invasive imaging of roots with high resolution X-ray micro-tomography. *Plant and Soil* **255**, 351-359.

Grossman J, Rice K (2012) Evolution of root plasticity responses to variation in soil nutrient distribution and concentration. *Evolutionary Applications* **5**, 850-857.

Gutierrez-Boem F, Thomas G (1999) Phosphorus nutrition and water deficits in field-grown soybeans. *Plant and Soil* **207**, 87-96.

Gyaneshwar P, Naresh Kumar G, Parekh L, Poole P (2002) Role of soil microorganisms in improving P nutrition of plants. *Plant and Soil* **245**, 83-93.

Hadfield J (2010) MCMC methods for multi-response generalised linear mixed models: the MCMCglmm R package. *Journal of Statistics Software* **33**, 1-22.

Hainsworth J, Aylmore LAG (1983) The use of computer-assisted tomography to determine spatial distribution of soil water content. *Australian Journal of Soil Research* **21**, 435-443.

Hainsworth J, Aylmore LAG (1989) Non-uniform soil water extraction by plant roots. *Plant and Soil* **113**, 121-124.

Hamza M, Anderson S, Aylmore LAG (2001) Studies of soil water drawdowns by singe radish roots at decreasing soil water content using computer-assisted tomography. *Australian Journal of Soil Research* **39**, 1387-1396.

Hamza M, Aylmore LAG (1992) Soil solute concentration and water uptake by single lupin and radish plant roots. *Plant and Soil* **145**, 187-196.

Hapca S, Wang Z, Otten W, Wilson C, Baveye P (2011) Automated statistical method to align 2D chemical maps with 3D X-ray computed micro-tomographic images of soils. *Geoderma* **164**, 146-154.

Hargreaves C, Gregory P, Bengough A (2009) Measuring root traits in barley (Hordeum vulgare ssp. vulgare and ssp. spontaneum) seedlings using gel chambers, soil sacs and X-ray microtomography. *Plant and Soil* **316**, 285-297.

Haynes R, Mokolobate M (2001) Amelioration of Al toxicity and P deficiency in acid soils by additions of organic residues: a critical review of the phenomenon and mechanisms involved. *Nutrient Cycling in Agroecosystems* **59**, 47-63.

He Y, Zhu Y, Smith S, Smith F (2002) Interacion between soil moisture content and phosphorus supply in spring wheat plants grown in pot culture. *Journal of Plant Nutrition* **25**, 913-925.

Heeraman D, Hopmans J, Clausnitzer V (1997) Three dimensional imaging of plant roots in situ with X-ray computed tomography. *Plant and Soil* **189**, 167-179.

Henry A, Chaves N, Kleinman P, Lynch J (2010) Will nutrient-efficient genotypes mine the soil? Effects of genetic differences in root architecture in common bean (Phaseolus vulgaris L.) on soil phosphorus depletion in a low-input agro-ecosystem in Central America. *Field Crops Research* **115**, 67-78.

Ho M, McCannon B, Lynch J (2004) Optimization modeling of plant root architecture for water and phosphorus acquisition. *Journal of Theoretical Biology* **226**, 331-340.

Ho M, Rosas J, Brown K, Lynch J (2005) Root architectural tradeoffs for water and phosphorus acquisition. *Functional Plant Biology* **32**(737-748).

Hodge A (2004) The plastic plant: root responses to heterogeneous supplies of nutrients. *New Phytologist* **162**, 9-24.

Horst W, Kamh M, Jibrin J, Chude V (2001) Agronomic measures for increasing P availability to crops. *Plant and Soil* **237**, 211-223.

Hounsfield G (1973) Computed transverse axial scanning (tomography). Part I. Description of system. *British Journal of radiology* **46**, 1016-1022.

Hutchings M, John E (2004) The effects of environmental heterogeneity on root growth and root/shoot partitioning. *Annals of Botany* **94**, 1-8.

Ingram P, Zhu J, Shariff A, Davis I, Benfey P, Elich T (2012) High-throughput imaging and analysis of root system architecture in Brachypodium distachyon under differential nutrient availability. *Philosphical Transactions of the Royal Society Biological Sciences* **367**, 1559-1569.

Isbell R (2012) 'The Australian soil classification: Revised edition.' (CSIRO Publishing: Collingwood, Vic.)

Iyer-Pascuzzi A, Symonova O, Mileyko Y, Hao Y, Belcher H, Harer J, Weitz J, Benfey P (2010) Imaging and analysis platform for automatic phenotyping and trait ranking of plant root systems. *Plant Physiology* **152**, 1148-1157.

Jackson R, Caldwell M (1989) The timing and degree of root proliferation in fertile-soil microsites for three cold-desert perennials. *Oecologia* **81**, 149-153.

Jackson R, Caldwell M (1996) Integrating resource heterogeneity and plant plasticity: modelling nitrate and phosphate uptake in a patchy soil environment. *Journal of Ecology* **84**, 891-903.

Jacobson A, Dousset A, Andreux F, Baveye P (2007) Electron microprobe and synchrotron X-ray fluorescence mapping of the heterogeneous distribution of copper in high-copper vinyard soils. *Environmental Science and Technology* **41**, 6343-6349.

Jassogne L (2008) Characterisation of porosity and root growth in a sodic texture-contrast soil. University of Western Australia, Perth

Jenneson P, Gilboy W, Morton E, Gregory P (2003) An X-ray micro-tomography system optimised for the low dose study of living organisms. *Applied Radiation and Isotopes* **58**, 177-181.

Joschko M, Muller P, Kotzke K, Dohring W, Larink O (1993) Earthworm burrow system development assessed by means of X-ray computed tomography. *Geoderma* **56**, 209-221.

Kaestner A, Lehmann E, Stampanoni M (2008) Imaging and image processing in porus media research. *Advances in Water Resources* **31**, 1174-1187.

Kaestner A, Schneeneli M, Graf F (2006) Visualizing three-dimensional root networks using computed tomography. *Geoderma* **136**, 459-469.

Karthikeyan A, Varadarajan D, Jain A, Held M, Carpita N, Raghothama K (2007) Phosphate starvation responses are mediated by sugar signaling in Arabidopsis *Planta* **225**, 907-918.

Ketcham R, Carlson W (2011) Acquisition, optimisation and interpretation of X-ray computed tomographic imagery: applications to the geosciences. *Computers and Geosciences* **27**, 381-400.

Kitchen M, Lewis R, *et al.* (2005) Phase contrast X-ray imaging of mice and rabbit lungs: a comparative study. *The British Journal of Radiology* **78**, 1018-1027.

Koebernick N (2011) In-situ obeservation of root-growth by x-ray tomography-relationship between root and water distribution during a drying cycle. In 'Rhizosphere3 International Conference. ' Ed. H Lambers): Perth, Australia)

Kopittke P, Menzies N (2004) Control of nutrient solutions for studies at high pH. *Plant and Soil* **266**, 343-354.

Langmaack M, Schrader S, Rapp-Bernhardt U, Kotzke K (1999) Quantitative analysis of earthworm burrow systems with respect to biological soil-structure regeneration after soil compaction. *Biology of Fertile Soils* **28**, 219-229.

Langmaack M, Schrader S, Rapp-Bernhardt U, Kotzke K (2002) Soil structure rehabilitation of arable soil degraded by compaction. *Geoderma* **105**, 141-152.

Lee T-C, Kashyap RL, Chu C-N (1994) Building skeleton models via 3-D medial surface/axis thinning algorithms. *CVGIP: Graph. Models Image Process.* **56**(6), 462-478.

Lewis R, Yagi N, *et al.* (2005) Dynamic imaging of the lungs using x-ray phase contrast. *Physics In Medicine and Biology* **50**, 5031-5040.

Linkohr B, Williamson L, Fitter A, Ottoline Leyser H (2002) Nitrate and phosphate availability and distribution have different effects on root system architecture of *Arabidopsis*. *The Plant Journal* **29**, 751-760.

Lombi E, McLaughlin M, Johnston C, Armstrong R, Holloway R (2004) Mobility, solubility and lability of fluid and granular forms of P fertiliser in calcareous and non-calcareous soils under laboratory conditions. *Plant and Soil* **269**, 25-34.

Lontoc-Roy M, Dutilleul P, Prasher S, Han L, Brouillet T, Smith D (2006) Advances in the acquisition and analysis of CT scan data to isolate a crop root system from the soils medium and quantify root system complexity in 3-D space. *Geoderma* **137**, 231-241.

Lopez-Bucio J, Cruz-Ramirez A, Herrera-Estrella L (2003) The role of nutrient availability in regulating root architecture. *Current Opinion in Plant Biology* **6**, 280-287.

Lopez-Bucio J, Hernandez-Abreu E, Sanchez-Calderon L, Nieto-Jacobo M, Simpson J, Herrera-Estrella L (2002) Phosphate availability alters architecture and causes changes in hormone sensitivity in the Arabidopsis root system. *Plant Physiology* **129**, 244-256.

Lynch J (1995) Root architecture and plant productivity. *Plant Physiology* **109**, 7-13.

Lynch J (2005) Root architecture and nutrient acquisition. In 'Nutrient acquisition by plants- an ecological perspective. Vol. 181.' Ed. H BrassiriRad). (Springer-Verlag: Heidelberg Berlin, Germany)

Lynch J (2007) Roots of the second green revolution. *Australian Journal of Botany* **55**, 495-512.

Lynch J, Brown K (2001) Topsoil foraging - an architectural adaption of plants to low phosphorus availability. *Plant and Soil* **237**, 225-237.

Lynch J, Ho M (2005) Rhizoeconomics: carbon costs of phosphorus acquisition. *Plant and Soil* **269**, 45-56.

Lynch J, Nielsen K, Davis R, Jablokow A (1997) SimRoot: modeling and visualisation of root systems. *Plant and Soil* **188**, 139-151.

Ma Q, Rengel Z (2008) Phosphorus aquisition and wheat growth are influenced by shoot phosphorus status and soil phosphorus distribution in a split-root system. *Journal of Plant Nutrition and Soil Science* **171**, 266-271.

Ma Q, Rengel Z, Bowden J (2007) Heterogeneous distribution of phosphrus and potassium in soil influences wheat growth and nutrient uptake. *Plant and Soil* **291**, 301-309.

Ma Q, Rengel Z, Rose T (2009) The effectiveness of deep placement of fertilisers is determined by crop species and edaphic conditions in Mediterranean-type environments:a review. *Australian Journal of Soil Research* **47**, 19-32.

MacFall J, Johnson G, Kramer P (1991) Comparative water uptake by roots of different ages in seedlings of loblolly pine (Pinus taeda L.). *New Phytologist* **119**, 551-560.

Mairhofer S, Zappala S, Tracy S, Sturrock C, Bennett M, Mooney S, Pridmore T (2012) RooTrak: Automated recovery of three-dimentional plant root architecture in soil from x-ray computed tomography images using visual tracking. *Plant Physiology* **158**, 561-569.

Malamy J (2005) Intrinsic and environmental response pathways that regulate root system architecture. *Plant, Cell and Environment* **28**, 67-77.

Mann C (1999) Crop scientists seek a new revolution. *Science* **283**, 310-314.

Manske G, Oritz-Monasterio J, Van Ginkel M, Gonzalez R, Rajaram S, Molina E, Vlek P (2000) Traits associated with improved P-uptake efficiency in CIMMYT's semidwarf spring bread wheat grown on an acid Andisol in Mexico. *Plant and Soil* **221**, 189-204.

McNeill A, Kolesik P (2004) X-ray CT investigations of intact soil cores with and without living crop roots. In 'SuperSoil 2004: 3rd Australian New Zealand Soils Conferance. ' University of Sydney, Australia)

Mees F, Swennen R, Van Geet M, Jacobs P (2003) 'Applications of X-ray computed tomography in the geosciences.' (Geological Society, London, Special Publications)

Menzies N, Guppy C (2000) In-situ soil solution extraction with polyacrylonitrile hollow-fibers. *Communications in Soil Science and Plant Analysis* **31**, 1875-1886.

Moody P, Bolland M (2005) Phosphorus. In 'Soil Analysis: an interpretation manual.' (Eds K Peverill, L Sparrow and D Reuter). (CSIRO Publishing: Collingwood, Victoria, Australia)

Mooney S (2002) Three-dimentional visualisation and quantification of soil macroporosity and water flow patterns using computed tomography`. *Soil Use and Management* **18**, 142-151.

Mooney S, Pridmore T, Helliwell J, Bennett M (2012) Developing X-ray computed tomography to non-invasively image 3-D root systems architecture in soil. *Plant and Soil* **352**, 1-22.

Moradi A, Carminati A, Vetterlein D, Vontobel P, Lehmann E, Weller U, Hopmans J, Vogel H, Oswald S (2011) Three-dimentional visualisation and quantification of water content in the rhizosphere. *New Phytologist* **192**, 653-663.

Moran C, Pierret A, Stevenson A (2000) X-ray absorption and phase contrast imaging to study the interplay between plant roots and soil structure. *Plant and Soil* **223**, 99-115.

Motomizu S, Wakimoto T, Toel K (1983) Spectrophotometric determination of phosphate in river waters with molybdate and malachite green. *Analyst* **108**, 361-367.

Nadaraya E (1964) On Estimating Regression. *Theory of Probability and its Applications* **9**, 141-142.

Nagel K, Kastenholz B, *et al.* (2009) Temperature responses of roots: impact on growth, root system archetecture and implications for phenotyping. *Functional Plant Biology* **36**, 947-959.

Nielsen K, Eshel A, Lynch J (2001) The effect of phosphorus availability on the carbon economy of contrasting common bean (Phaseolus vulgaris L.) genotypes. *Journal of Experimental Botany* **52**(335), 239-339.

North P (1976) Towards an absolute measurement of soil structural stability using ultrasound. *Journal of Soil Science* **27**, 451-459.

O'Donnell A, Young I, Rushton S, Shirley M, Crawford J (2007) Visualization, modeling and prediction of soil microbiology. *Nature Reviews Microbiology* **5**, 689-699.

Officer S, Dunbabin V, Armstrong R, Norton R, Kearney G (2009) Wheat roots proliferate in response to nitrogen and phosphorus fertilisers in sodosol and vertisol soils of south-eastern Australia. *Australian Journal of Soil Research* **47**, 91-102.

Passioura J (2002) Soil conditions and plant growth. *Plant, Cell and Environment* **25**, 311-318.

Perez Corona M, Van Der Klundert I, Verhoeven J (1996) Availability of organic and inorganic phosphorus compounds as phosphorus sources for *Carex* species. *New Phytologist* **133**, 225-231.

Perret J, Al-Belushi M, Deadman M (2007) Non-destructive visualisation and quantification of roots using computed tomography. *Soil Biology and Biochemistry* **39**, 391-399.

Petrovic A, Siebert J, Rieke P (1982) Soil bulk density analysis in three dimensions by computed tomographic scanning. *Soil Science Society of America Journal* **46**, 445-450.

Phoenix GE (2009) Computed tomography and volume reconstruction. In 'Datosx training presentation. ' (Phoenix X-ray: Wunstorf, Germany)

Pierret A, Capowiez Y, Moran C, Kretzschmar A (1999a) X-ray computed tomography to quantify tree rooting spatial distributions. *Geoderma* **90**, 307-326.

Pierret A, Moran C, Doussan C (2005) Conventional detection methodology is limiting our ability to understand the roles and functions of fine roots. *New Phytologist* **166**, 967-980.

Pierret A, Moran C, Pankhurst C (1999b) Differentiation of soil properties related to the spatial association of wheat roots and soil macropores. *Plant and Soil* **211**, 51-58.

Pierzynski G, McDowell R, Sims J (2005) Chemistry, cycling and potential movement of inorganic phosphorus in soils. In 'Phosphorus: Agriculture and the environment.' (Eds J Sims and A Sharpley) pp. p.53-86. (American Society of Agronomy, Crop Science Society of America, Soil Science Society of America, Inc.,: Madison, WI)

Preibisch S, Saalfeld S, Tomancak P (2009) Globally opimal stitching of tiled 3D microscopic image acquisitions. *Bioinformatics* **25**, 1463-1465.

Prodanovic M, Lindquist W, Seright R (2006) Porus structure and fluid partitioning in polyethylene cores from 3D X-ray microtomographic imaging. *Journal of Colloid and Interface Science* **298**, 282-297.

R Development Core Team (2010) R: A language and environment for statistical computing. In. ' 2.10.1 edn. (R Foundation for Statistical Computing: Vienna, Austria)

Ramaekers L, Remans R, Rao I, Blair M, Vanderleyden J (2010) Strategies for improving phosphorus acquisition efficiency of crop plants. *Field Crops Research* **117**, 169-176.

Reymond M, Svistoonoff S, Loudet O, Nussaume L, Desnos T (2006) Identification of QTL controlling root growth response to phosphate starvation in Arabidopsis thaliana. *Plant, Cell and Environment* **29**, 115-125.

Robinson D (1994) Tansley Review No. 73 The responses of plants to non-uniform supplies of nurtients. *New Phytologist* **127**, 635-674.

Robinson D (2005) Integrated root responses to variations in nutrient supply. In 'Nutrient acquisition by plants- an ecological perspective. Vol. 181.' Ed. H BrassiriRad). (Springer-Verlag: Heidelberg Berlin, Germany)

Rose T, Rengel Z, Ma Q, Bowden J (2009) Crop species differ in root plasticity response to localised P supply. *Journal of Plant Nutrition and Soil Science* **172**, 360-368.

Rubio G, Walk T, Ge Z, Yan X, Liao H, Lynch J (2001) Root gravitropism and below-ground competition among neighbouring plants: a modelling approach. *Annals of Botany* **88**, 929-940.

Sato Y, Nakajima S, Shiraga N, Atsumi H, Yoshida S, Koller T, Gerig G, Kikinis R (1998) Three-dimensional multi-scale line filter for segmentation and visualisation of curvilinear structures in medical images. *Medical Image Analysis* **2**, 143-168.

Schachtman D, Reid R, Ayling S (1998) Phosphorus uptake by plants: from soil to cell. *Plant Physiology* **116**, 447-453.

Schindelin J, Arganda-Carreras I, *et al.* (2012) FiJi: and open-source platform for biological-image analysis. *Nature Methods* **9**, 676-682.

Schrader S, Rogasik H, Onasch I, Jegou D (2007) Assessment of soil structural differentiation around earthworm burrows by means of x-ray computed tomography and electron microscopy. *Geoderma* **137**, 378-387.

Schulz H, Postma J, van Dusschoten D, Scharr H, Behnke S 3D reconstruction of plant roots from MRI images. In 'International Conference on Computer Vision Theory and Applications', 2012, Rome,

Smith F (2002) The phosphate uptake mechanism. *Plant and Soil* **245**, 105-114.

Stock SR (2008) Recent advances in X-ray microtomography applied to materials. *International Materials Reviews* **53**(3), 129-181.

Strom S, Owen A, Godbold D, Jones D (2005) Organic acid behaviour in a calcareous soil imlicatiopns for rhizosphere nutrient cycling. *Soil Biology and Biochemistry* **37**, 2046-2045.

Sun W, Brown S, Leach R (2012) NPL Report 32 -An overview of industrial X-ray computed tomography. National Physical Labratory, Teddington, Middlesex.

Svistoonoff S, Creff A, Reymond M, Sigoillot-Claude C, Ricaud L, Blanchet A, Nussaume L, Desnos T (2007) Root tip contact with low- phosphate media reprograms plant root architecture. *Nature Genetics* **39**, 792-796.

Taina I, Heck R, Elliot T (2008) Application of X-ray compted tomography to soil science: a literature review. *Canadian Journal of Soil Science* **88**, 1-20.

Tibbet M (2000) Roots, foraging and the exploitation of soil nutrient patches: the role of mycorrhizal symbiosis. *Functional Biology* **14**, 397-399.

Ticconi C, Abel S (2004) Short on phosphate: plan surveillance and countermeasures. *Trends in Plant Science* **9**, 548-555.

Tillman D, Cassman K, Matson P, Naylor R, Polasky S (2002) Agricultural sustainability and intensity production practices. *Nature* **418**, 671-677.

Tinker P, Nye P (2000) 'Solute Movement in the Rhizosphere.' (Oxford University Press: New York)

Tippkotter R, Eickhorst T, Taubner H, Gredner B, Rademaker G (2009) Detection of soil water in macropores of undisturbed soil using microfocus X-ray tube computerized tomography (μCT). *Soil and Tillage Research* **105**, 12-20.

Tracy S, Black C*, et al.* (2011) Quantifying the effect of soil compaction on three varieties of wheat (Triticum aestivum L.) using X-ray micro computed tomography (CT). *Plant and Soil* **353**, 195-208.

Tracy S, Black C, Roberts J, Sturrock C, Mairhofer S, Craigon J, Mooney S (2012) Quantifying the impact of soil compaction on root system architecture in tomato (Solanum lycopersicum) by X-ray micro-computed tomography. *Annals of Botany* **110**, 511-519.

Tracy S, Roberts J, Black C, McNeill A, Davidson R, Mooney S (2010) The X-factor: Visualising undisturbed root archetecture in soils using X-ray computed tomography. *Journal of Experimental Botany* **61**(2), 311-313.

USDA (1999) Soil Taxonomy- a basic system of soil classification for making and interpreting soil surveys. In. ' Second Edition edn. Ed. USDo Agriculture). (U.S. Government Printing Office: Washington, DC, USA)

Valizadeh G, Rengel Z, Rate A (2002) Wheat genotypes differ in growth and phosphorus uptake when supplied with different sources and rates of phosphorus banded or mixed in soil in pots. *Australian Journal of Experimental Agriculture* **42**, 1103-1111.

Van den Bulcke J, Boone M, Van Acker J, Van Hoorebeke L (2009) Three-dimensional X-ray imaging and analysis of fungi on and in wood. *Microscopy and Microanalysis* **15**, 395-402.

Van Dusschoten D (2011) Quantitative 3D root imaging in natural-like soil by MRI. In 'Rhizosphere 3 International Conference. ' Ed. H Lambers): Perth, Australia)

Vance C, Uhde-Stone C, Allen D (2003) Phosphorus acquisition and use: Critical adaptions by plants for securing a nonrenewable resource. *New Phytologist* **157**, 423-447.

Vontobel P, Lehmann E, Hassanein R, Frei G (2006) Neutron tomography: method and applications. *Physica B* **385-386**, 475-480.

Waisel Y, Eshel A, Kafkafi U (1996) 'Plant Roots: the hidden half.' 2nd edn. (Marcel Dekker: New York, USA) 1002

Wang Y, De Carlo F*, et al.* (2001) A high-throughput X-ray microtomography system at the Advances Photon Source. *Review of Scientific Instruments* **72**, 2062-2068.

Wang Y, Garvin D, Kochian L (2002) Rapid induction of regulatory and transporter genes in response to phosphorus, potassium, and iron deficiencies in Tomato roots. Evidence for cross talk and root/rhizosphere-mediated signals. *Plant Physiology* **130**, 1361-1370.

Watanabe K, Mandang T, Tojo S, Ai F, Huang B (1992) Non-destructive root-zone analysis with X-ray CT scanner. Paper 923018. In 'American Society of Agricultural Engineers. ' St. Joseph, MI, USA)

Watson G (1964) Smooth Regression Analysis. *Sankhya: The Indian Journal of Statistics* **26**, 359-372.

Watt M, Evans J (1999) Proteoid Roots. Physiology and development. *Plant Physiology* **121**, 317-323.

Watt M, Kirkegaard J, Rebetzke G (2005) A wheat genotype developed for rapid leaf growth copes well with the physical and biological constraints of unploughed soil. *Functional Plant Biology* **32**, 695-706.

Wildenschild D, Armstrong R, Herring A, Young I, William Carey J (2011) Exploring capillart trapping efficiency as a function of interfacial tension, viscosity and flow rate. *Energy Procedia* **4**, 4945-4952.

Wildenschild D, Hopmans J, Vaz C, Rivers M, Rikard D, Christensen B (2002) Using X-ray computed tomography in hydrology: systems, resolutions and limitations. *Journal of Hydrology* **267**, 285-297.

Williamson L, Ribrioux S, Fitter A, Leyser H (2001) Phosphate availability regulates root system architecture in Arabidopsis. *Plant Physiology* **126**, 875-882.

Yang H, Knapp J, Koirala P, Rajagopal D, Ann Peer W, Silbart L, Murphy A, Gaxiola R (2007) Enhansed phosphorus nutrition in monocots and dicots over-expressing a phosphorus-responsive type I H^+-pyrophosphatase. *Plant Biotechnology Journal* **5**, 735-745.

Young I (1998) Biophysical interactions at the root-soil interface: a review. *Journal of Agricultural Science* **130**, 1-7.

Young I, Crawford J, Nunan N, Otten W, Spiers A (2008) Microbial distribution in soils: physics and scaling. *Advances in Agronomy* **100**, 81-121.

Young I, Crawford J, Rappoldt C (2001) New methods and models for characterising structural heterogeneity of soil. *Soil and Tillage Research* **61**, 33-45.

Young IM, Crawford J (2004) Interactions and self- organisation in the soil-microbe complex. *Science* **304**, 1634-1637.

Zhu J, Lynch J (2004) The contribution of lateral rooting to phosphorus acquisition efficiency in maize (Zea mays) seedlings. *Functional Plant Biology* **31**, 949-958.

Zuiderveld K (1994) Contrast limited adaptive histogram equalization. In 'Graphics gems IV.' Ed. SH Paul) pp. 474-485. (Academic Press Professional, Inc.)

Publications arising from this thesis

Publications

Helliwell J.R., Sturrock C.J., Grayling K.M., Tracy S.R., **Flavel R.J.**, Young I.M., Whalley W.R., Mooney S.J. (2013), Applications of X-ray computed tomography for examining biophysical interactions and structural development in soil systems: a review. *European Journal of Soil Scienc*e, DOI: 10.1111/ejss.12028

Flavel, R., Guppy, C., Tighe, M., Watt, M., McNeill, A., Young, I. (2012) Non-destructive quantification of cereal roots in soil using high-resolution X-ray tomography. *Journal of Experimental Botany* 63: 2503-2511

Flavel, R., Guppy, C., Watt, M., Tighe, M., Young, I.M (Submitted) Quantifying *in situ* root plasticity and architecture in soil: phosphorus responses. Submitted to *Nature*

Conference presentations

Flavel, R., Guppy, C., Young, I., (2012) Detecting change in root length density in response to nutrient patches using micro-CT, *Roots to the future- 8th international symposium of the International Society of Root Research,* Dundee, Scotland (Peer reviewed) Poster Prize.

Flavel, R., Guppy, C., Young, I., (2011) The use of X-ray tomography for measuring cereal root proliferation in response to phosphorus nutrition, *Rhizosphere 3 International Conference 2011,* Perth Australia (Peer reviewed).

Guppy, C., **Flavel, R.** (2011) Cereals seeking phosphorus: how much to spend on a first date? *Grains Research and Development Corporation Research Update*, Goondiwindi, Australia.

Guppy, C., **Flavel, R.,** Schneider, D., Roberts, J., Jasper, S., Young, I., (2011) Preliminary soil compaction results from McMaster research station. *Grains Research and Development Corporation Research Update*, Goondiwindi, Australia.

Appendices

Appendix 1

Appendix 1| Image J macro toolbar file contents for the FlavelThesisMacro.ijm. Corresponds with Figure 4.1.when the Macro is installed.

```
//====== Import .vol files
macro "Flavel Vol Import Action Tool - C090L808fL8fcaL4a8fL1fff"{
	requires("1.46c");
	vol = File.openDialog("Open Phoenix .vol File:");
	dir = File.getParent(vol);
	name = File.getName(vol);
	sample = File.nameWithoutExtension;
	vgi = dir+File.separator+sample+".vgi";

	LF=10; TAB=9;
	s1 = File.openAsRawString(vgi);
	n = lengthOf(s1);
	String.resetBuffer;
	for (i=0; i<n; i++) {
	    c = charCodeAt(s1, i);
	    if (c==LF)
	        String.append("\n");
	    else if (c==TAB)
	        String.append(" ");
	    else if (c>=32 && c<=127)
	        String.append(fromCharCode(c));
	}
	s2 = String.buffer;
	print("\\Clear");
	n = lengthOf(s2);

	split(s2,"\n");
	sizeX = substring(s2,34,37);
	sizeY = substring(s2,38,41);
	sizeZ = substring(s2,42,45);
	bitdepth = substring(s2,63,65);
	if (bitdepth=="bi"){bitdepth="32f";}
	res = substring(s2,n-37,n-28);
```

```
      unit = substring(s2,n-20,n-17);
      selectWindow("Log");
      run("Close");

      Dialog.create("According to the .vgi");
      Dialog.addMessage("Please Check these are correct:");
      Dialog.addNumber("X Dimensions:", sizeX);
      Dialog.addNumber("Y Dimensions:", sizeY);
      Dialog.addNumber("Z Dimensions:", sizeZ);
      Dialog.addString("Bit Depth:", bitdepth);
      Dialog.addNumber("Resolution:", res,8,10,"");
      Dialog.addString("Units:", unit);
      Dialog.addCheckbox("Print details?",false);
      Dialog.show();
      sizeX = Dialog.getNumber();
      sizeY = Dialog.getNumber();
      sizeZ = Dialog.getNumber();
      bitdepth = Dialog.getString();
      res = Dialog.getNumber();
      unit = Dialog.getString();
      quiet = Dialog.getCheckbox();

      if (quiet==true){

      print("Xdim:",sizeX);print("Ydim:",sizeY);print("Zdim:",sizeZ)
;print("BitDepth:",bitdepth);print("Resolution:",res);print("Unit:",
unit);
            print("vol:", vol);print("vgi:",vgi);print("name:",
name);print("directory:", dir);print("sample:", sample);
            }

      if (bitdepth=="16"){
            run("Raw...", "open=&vol image=[16-bit Unsigned]
width=&sizeX height=&sizeY offset=0 number=&sizeZ gap=0 little-
endian");
            } else if (bitdepth=="32"){
            run("Raw...", "open=&vol image=[32-bit Unsigned]
width=&sizeX height=&sizeY offset=0 number=&sizeZ gap=0 little-
endian");
            } else if (bitdepth=="32f"){
```

```
            run("Raw...", "open=&vol image=[32-bit Real]
width=&sizeX height=&sizeY offset=0 number=&sizeZ gap=0 little-
endian");
            } else {
            exit("Error -there is a problem with the bit depth
figure");
            }

      setVoxelSize(res, res, res, unit);
}
//======
macro "Clear Outside Action Tool - C090R11eeO11ee" {
      requires("1.46c");
      setSlice(nSlices/2);
      setBackgroundColor(0,0,0);
      setTool(1);
      makeOval(0,0,(getWidth()),(getHeight()));
      waitForUser("","Please Ajust Circle Position");
      run("Clear Outside", "stack");
      run("Select None");
}
//====== Align 1st peak (inferior surrogate for full normalisation)
macro "Flavel Align 1st Peak Action Tool -
C090L0f50L50afL5fa0La0ff"{
      requires("1.46c");
      if (bitDepth()!=16){run("16-bit");}
      A=fstPeakMed(1,65534);
      //print("Peak Count",A[0],"-","Peak Value",A[1]);
      Dialog.create("Setting peak value");
      Dialog.addMessage("Please enter the grey-scale \nvalue you
want the peak to be at:");
      Dialog.addNumber("Grey value:", 30000,0,10,"");
      Dialog.addCheckbox("Print peak values?",false);
      Dialog.show();
      std = Dialog.getNumber();
      prnt=Dialog.getCheckbox();

      alignHist(A[1],std);
      if (prnt==true) {print("Peak Height:",A[0]," Peak
Value:",A[1]);}
      }
```

```
//====== Stack sequential scans
macro "Flavel Scan Stacker Action Tool - C090L33d3L38d8L3ddd"{
      requires("1.46c");
      Dialog.create("Image Stacker");
      Dialog.addMessage("The following information is required to
\nstack your laterally adjoining images:");
      Dialog.addNumber("How many scans do you need to stack?", 3,
0,2,"scans");
      Dialog.addNumber("How many slices overlap between scans?", 6,
0,3,"slices");
      Dialog.addNumber("Grey value for peak?", 30000,0,10,"");
      Dialog.addCheckbox("How would you like to correct the
histogram?\nby histogram first peak (tick) or by subsample mean
(untick) or by", true);
      Dialog.show();
      volNo = Dialog.getNumber();
      overlap = Dialog.getNumber();
      stand = Dialog.getNumber();
      sampOrHist = Dialog.getCheckbox();

      imtitles=newArray(volNo);
      for (k=1;k<=volNo;k++){
            waitForUser("Please select scan"+k+" (starting at the
top)");
            imtitles[(k-1)]=getTitle();
            wait(50);
      }
      if (sampOrHist==false){
            run("Set Measurements...", "  median redirect=None
decimal=3");
            for (k=1;k<=volNo;k++){
                  selectWindow(imtitles[k-1]);

      makeOval((0.475*getWidth()),(0.475*getHeight()),(0.05*getWidth
()),(0.05*getWidth()));
                  waitForUser("","Please Ajust Elipse Position");
                  A=measureStack("Median");
                  Array.getStatistics(A,x,x,mn,x);
                  selectWindow(imtitles[k-1]);
                  waitForUser("","Please click outside the Elipse");
                  alignHist(mn,stand);
```

```
            }
            selectWindow("Results");
            run("Close");

      } else {
            for (k=1;k<=volNo;k++){
                  selectWindow(imtitles[k-1]);
                  if (bitDepth()!=16){run("16-bit");}
                  X=fstPeakMed(1,65534);
                  wait(250);
                  alignHist(X[1],stand);
            }
      }
      selectWindow(imtitles[0]);
      las=nSlices-(0.5*overlap);
      run("Duplicate...", "title=[Stack1] duplicate range=1-&las");
      //selectWindow(imtitles[0]);
      //close();
      if (volNo>2){
            for (k=1;k<=(volNo-2);k++){
                  selectWindow(imtitles[k]);
                  fir=(0.5*overlap);
                  las=nSlices-(0.5*overlap);
                  title="Stack"+(k+1);
                  run("Duplicate...", "title=&title duplicate
range=&fir-&las");
                  //selectWindow(imtitles[k]);
                  //close();
            }
      }
      selectWindow(imtitles[(volNo-1)]);
      fir=(0.5*overlap);
      title="Stack"+volNo;
      run("Duplicate...", "title=&title duplicate range=&fir-
&nSlices");
      //selectWindow(imtitles[(volNo-1)]);
      //close();

      title="M"+imtitles[0];
      if(volNo==2) {run("Concatenate...", " title=&title
image1=[Stack1] image2=[Stack2] image3=[-- None --]");}
```

```
      else if(volNo==3) {run("Concatenate...", " title=&title
image1=[Stack1] image2=[Stack2] image3=[Stack3] image4=[-- None --
]");}
      else if(volNo==4) {run("Concatenate...", " title=&title
image1=[Stack1] image2=[Stack2] image3=[Stack3] image4=[Stack4]
image5=[-- None --]");}
      else if(volNo==5) {run("Concatenate...", " title=&title
image1=[Stack1] image2=[Stack2] image3=[Stack3] image4=[Stack4]
image5=[Stack5] image6=[-- None --]");}
      else if(volNo==6) {run("Concatenate...", " title=&title
image1=[Stack1] image2=[Stack2] image3=[Stack3] image4=[Stack4]
image5=[Stack5] image6=[Stack6] image7=[-- None --]");}
      else run("Concatenate...");
}
//====== RootOne
macro "Flavel RootOne Action Tool - C090L0a2aL2a4dL4d63L63f3T8f121"{
//improve output to 16-bit, check tubeness settings, alter LowerTh
>1
      requires("1.46c");
      tick=getTime();
      run("16-bit");

      Imagetitle = getTitle();
      Sliceno = nSlices;
      getVoxelSize(x,y,z,Unit);
      Res=x;

      // spatially callibrate images
      Dialog.create("Calibrate Image:");
      Dialog.addMessage("Please check voxel side length:");
      Dialog.addNumber("", Res, 6,8,Unit);
      Dialog.addMessage("Check the stacks you want to save:");
      Dialog.addCheckbox("Save the Grey Fill Stack?", true);
      Dialog.addCheckbox("Save the Binary Stack?", false);
      Dialog.addMessage("(Save Binary required for 3D vis)");
      Dialog.addCheckbox("Require 3D vis of Binary Stack?", false);
      Dialog.addCheckbox("Save Log file?", true);
      Dialog.addCheckbox("Remove Pores?", false);
      //Dialog.addCheckbox("Run fast?", true);
      Dialog.show();
      Voxdim = Dialog.getNumber();
```

```
	goGreyFill = Dialog.getCheckbox();
	goBinStack = Dialog.getCheckbox();
	go3DVis = Dialog.getCheckbox();
	goLogFile= Dialog.getCheckbox();
	rpores= Dialog.getCheckbox();
	//goFast= Dialog.getCheckbox();

	if (goGreyFill==true||goBinStack==true||goLogFile==true){
		Direct = getDirectory("Choose a directory for
outputs:");
	}
	setVoxelSize(Voxdim, Voxdim, Voxdim, Unit);

//Include clear outside protocol here
	//if (goFast==true){setBatchMode(true);}
//remove pores
	if(rpores==true){
		selectWindow(Imagetitle);
		run("Duplicate...", "title=[rpores] duplicate range=1-
&nSlices");
		run("Threshold...");
		waitForUser("Please set threshold for only\nthe pore
space then press 'OK'");
		run("Convert to Mask", "background=Dark black");
		selectWindow("Threshold");
		run("Close");
		selectWindow("rpores");
		//run("Find Edges", "stack");
		run("Dilate", "stack");
		run("Replace value", "pattern=0 replacement=1");
		run("Replace value", "pattern=255 replacement=0");
		imageCalculator("Multiply create stack", Imagetitle,
"rpores");
		rename("Bin Roots");
		selectWindow("rpores");
		close();

	}
	else {
		selectWindow(Imagetitle);
```

```
            run("Duplicate...", "title=[Bin Roots] duplicate
range=1-&nSlices");
      }


      run("Collect Garbage");
/*    selectWindow("Bin Roots");
      ArA=fstPeakMed(1,65534);
      UpperTh=round(0.78*ArA[1]+462);
      print(ArA[1]);
*/
//-------------------------------------------------------------------
--
// threshold roots from scan data
// improve by inserting threashold choice here rather than fixed
value
      LowerTh=8000; //improve by removing some of the pores
      UpperTh=23862;
      selectWindow("Bin Roots");
      setThreshold(LowerTh, UpperTh);
      run("Convert to Mask", " black");
//perfrom distance transform on the binary data
      selectWindow("Bin Roots");
      run("Duplicate...", "title=[Distbw] duplicate range=1-
&nSlices");
      run("Invert", "stack");
      run("Distance Transform 3D");
      Stack.getStatistics(x,x,smin,smax,x);
      smax=smax/10;
      run("Divide...", "value=smax stack");
      run("Add...", "value=1 stack");
      run("Enhance Contrast", "saturated=0.35");
      selectWindow("Distbw");
      close();

//perform tubeness transform on the binary data
      selectWindow("Bin Roots");
      sig=1.5*Voxdim;
      run("Tubeness", "sigma=&sig use");
      rename("Tube");
      Stack.getStatistics(x,x,smin,smax,x);
```

```
	smax=smax/10;
	run("Divide...", "value=smax stack");
	run("Add...", "value=1 stack");
	run("Enhance Contrast", "saturated=0.35");

//aquire inverted grey roots
	selectWindow("Bin Roots");
	run("Replace value", "pattern=255 replacement=1");
	imageCalculator("Multiply create 32-bit stack", Imagetitle,
"Bin Roots");
	rename("InvGreyRoots");
	selectWindow("Bin Roots");
	run("Replace value", "pattern=1 replacement=255");
	selectWindow("InvGreyRoots");

	run("Invert", "stack");
	Stack.getStatistics(x,x,smin,smax,x);
	tmax=smax-(smax*0.1);
	setThreshold(0,tmax);
	run("NaN Background", "stack");
	resetThreshold();
	Stack.getStatistics(x,x,smin,smax,x);
	smax=smax/10;
	run("Divide...", "value=smax stack");
	run("Add...", "value=1 stack");
	run("Enhance Contrast", "saturated=0.35");

//combine the information from distance and tubeness

	imageCalculator("Multiply create 32-bit stack","Distance",
"Tube");
	rename("DistxTube");
	selectWindow("Distance"):
	close();
	selectWindow("Tube");
	close();
	run("Collect Garbage");
	Stack.getStatistics(x,x,smin,smax,x);
	smax=smax/10;
	run("Divide...", "value=smax stack");
	run("Add...", "value=1 stack");
```

```
	run("Enhance Contrast", "saturated=0.35");
	imageCalculator("Multiply create 32-bit stack","DistxTube",
"InvGreyRoots");
	run("16-bit");
	run("Convert to Mask", "method=MaxEntropy background=Dark
black");
	rename("Bin Roots");
	selectWindow("DistxTube");
	close();
	selectWindow("InvGreyRoots");
	close();
	run("Collect Garbage");

	run("Replace value", "pattern=255 replacement=1");
	imageCalculator("Multiply create stack","Bin
Roots",Imagetitle);
	rename("Grey Roots");//(8-bit stack)
	if (goGreyFill==true) {
getStatistics(decoy,decoy,decoy,max,decoy,decoy);}
	selectWindow("Bin Roots");
	run("Replace value", "pattern=1 replacement=255");

// create grey background and save
	if (goGreyFill==true) {
		selectWindow("Grey Roots");
		Replace = max + 1;
		run("Replace value", "pattern=0 replacement=&Replace");
		GBDir =
Direct+File.separator+"GB"+Imagetitle+File.separator;
		File.makeDirectory(GBDir);
		GBName = "GB"+Imagetitle;
		run("Image Sequence... ", "format=TIFF name=&GBName
start=0 digits=4 save=&GBDir");
	}

// save outputs to file in
	if (goBinStack==true){
		BinDir =
Direct+File.separator+"Bin"+Imagetitle+File.separator;
		File.makeDirectory(BinDir);
		selectWindow("Bin Roots");
```

```
            BinName = "Bin"+Imagetitle;
            run("Image Sequence... ", "format=TIFF name=&BinName
start=0 digits=4 save=&BinDir");
      }
// clean up unnecessary stacks
      //if (goFast==true){setBatchMode(false);}

// view in 3D viewer
      if (go3DVis==true) {
            run("Image Sequence...", "open=&BinDir number=&Sliceno
starting=1 increment=1 scale=100 file=[] or=[] sort");
            run("3D Viewer");
            call("ij3d.ImageJ3DViewer.setCoordinateSystem",
"false");
            call("ij3d.ImageJ3DViewer.add", BinName, "None",
BinName, "0", "true", "true", "true", "2", "0");
            }

      tock=getTime();
      time=(tock-tick)*0.00001666;
      if (goLogFile==true){
            print("Sample: ",Imagetitle);
            print("Number of slices: ",nSlices);
            print("Voxel dimentions: [x] ",x," [y] ",y," [z] ",z,"
Units ",Unit);
            //print("GoFast was set to: ",goFast);
            print("And RootOne took: ",time," mins");
            print("The inflection point Threshold Value",ArA[1]);
            print("The Lower threshold was set to: ",LowerTh);
            print("Corrected upper threshold estimate: ",UpperTh);
            selectWindow("Log");
            saveAs("Text", Direct+File.separator+Imagetitle+"-
log.txt");
      }

      selectWindow("Log");
      run("Close");
      wait(1000);
      beep();
}
//====== Root Length Density and Branching Density
```

```
macro "Flavel RLD BD Determinator Action Tool - C090L515fL58d8"{
	requires("1.46c");
	Imagetitle = getTitle();
	getVoxelSize(x,y,z,Unit);

	Dialog.create("Flavel RLD/BD Calculator:");
	Dialog.addMessage("Please Check voxel side length:");
	Dialog.addNumber("X", x, 6,8,Unit);
	Dialog.addNumber("Y", y, 6,8,Unit);
	Dialog.addNumber("Z", z, 6,8,Unit);
	Dialog.addMessage("Check the stacks or outputs you want to
save:")
	Dialog.addCheckbox("Save the Smoothed Stack?", true);
	Dialog.addCheckbox("Save the Skeletonised Stack?", false);
	Dialog.show();
	x = Dialog.getNumber();
	y = Dialog.getNumber();
	z = Dialog.getNumber();
	Smooth = Dialog.getCheckbox();
	Skele = Dialog.getCheckbox();

	if (Smooth==true||Skele==true){
		Direct = getDirectory("Choose a directory for
outputs:");
	}
//Calibrate image to pix count-
	setVoxelSize(1,1,1,"Pix");
//Determine Area of Pot and assign to variable
	setTool("oval");
	makeOval(0,0,(getWidth()),(getHeight()));
	waitForUser("","Please Ajust Circle Position to Area of
Soil");
	run("Set Measurements...", "area limit redirect=None
decimal=3");
	A=measure("Area");
	run("Clear Results");
	resultname="Results "+Imagetitle;
	IJ.renameResults("Results",resultname);
//Clear Circle
	waitForUser("","Please Click Outside Circle");
//Calculate Variables for future calculations
```

```
	Rcm=(x*0.1);
	R=(x*0.1)*(y*0.1)*(z*0.1);
//Gaussian blur and threshold image to reconnect gaps, remove holes
	run("Smooth (3D)", "method=Gaussian sigma=1.5 use");
	run("Auto Threshold", "method=IsoData white stack");
	//run("Auto Threshold", "method=Li white stack");
//Fill holes
	run("Analyze Particles...", "size=0-Infinity pixel
circularity=0.00-1.00 show=Masks include stack");
	Imagetitle2 = Imagetitle+"Smooth";
	rename(Imagetitle2);
	selectWindow("Smoothed");
	close();
	run("Collect Garbage");
	selectWindow(Imagetitle2);
	run("Convert to Mask", "method=Default background=Dark
black");
//Measure and Save Root Volume
	setThreshold(254,255);
	rv=measureStack("Area");
	rV=arrayByValue(rv,R);
	ChangeResultWind("F",resultname);
	array2Results(rV,"RootVolPerSlice-cm3");
	ChangeResultWind("B",resultname);

//Save Smooth Stack if required
	if (Smooth==true){
		selectWindow(Imagetitle2);
		setVoxelSize(x,y,z,Unit);
		SmDir =
Direct+File.separator+Imagetitle2+File.separator;
		File.makeDirectory(SmDir);
		run("Image Sequence... ", "format=TIFF name=&ImageTitle2
start=0 digits=4 save=&SmDir");
		setVoxelSize(1,1,1,"Pix");
	}
//Skeletonise
	run("Skeletonize (2D/3D)");
//Measure and Save Root Length and RLD
	setThreshold(254,255);
	sv=measureStack("Area");
```

```
	sV=arrayByValue(sv,Rcm);
	rld=arrayByValue(sV,(1/(A*R)));
	ChangeResultWind("F",resultname);
	array2Results(sV,"RootLengthPerSlice-cm");
	array2Results(rld,"RLD-cmcm3");
	ChangeResultWind("B",resultname);

//Save skeleton if required
	if (Skele==true){
		selectWindow(ImageTitle2);
		setVoxelSize(x,y,z,Unit);
		SkDir =
Direct+File.separator+Imagetitle+"Skele"+File.separator;
		File.makeDirectory(SkDir);
		ImageTitle4=Imagetitle+"Skele";
		run("Image Sequence... ", "format=TIFF name=&ImageTitle4
start=0 digits=4 save=&SkDir");
		setVoxelSize(1,1,1,"Pix");
	}
//Measure and save Branching Density
	run("Analyze Skeleton (2D/3D)","prune=none");
	selectWindow("Tagged skeleton");
	setThreshold(69,71);
	bd=measureStack("Area");
	bD=arrayByValue(bd,(1/(A*R)));
	ChangeResultWind("F",resultname);
	array2Results(bD,"BranchDen-Bcm3");
	array2Results(rv,"RootVol-count");
	array2Results(sv,"SkeleVol-count");
	array2Results(bd,"Branches-count");

//Record results in table and save to .xls
	aa="Sample: "+Imagetitle;
	ab="Source Location: "+Direct;
	ac="Area of the pot: "+A+" pix";
	ad="Voxel dimentions: [x] "+x+" [y] "+y+" [z] "+z+" Units
"+Unit;
	ae="Resolution: "+Rcm+" cm";
	af="Voxel Volume: "+R+" cm^3";
	ag="Volume of pot per slice: "+(A*R)+" cm^3";
	print("Flavel RLD/BD determinator");
```

```
	print(aa);
	print(ab);
	print(ac);
	print(ad);
	print(ae);
	print(af);
	print(ag);

//Save result files to folder
	selectWindow("Results");
	XLS=Direct+File.separator+Imagetitle+"-results.xls";
	saveAs("results", XLS);
	selectWindow("Log");
	XLS=Direct+File.separator+Imagetitle+"-log.txt";
	saveAs("text", XLS);
	selectWindow("ResultsPad");
	run("Close");
}
//======
macro "Branching Angle Action Tool - C090La11eL1eeeT8c08oDa9"{
	requires("1.39f");
	Imagetitle = getTitle();
	Sliceno = nSlices();
	dir = File.getParent(getDirectory("image"));
	getVoxelSize(xv,yv,zv,unit);

	Dialog.create("Flavel Branch Angle Calculator:");
	Dialog.addMessage("Please Enter Voxel Side Length:");
	Dialog.addNumber("",xv,6,8,unit);
	Dialog.addNumber("",yv,6,8,unit);
	Dialog.addNumber("",zv,6,8,unit);
	Dialog.show();
	xv = Dialog.getNumber();
	yv = Dialog.getNumber();
	zv = Dialog.getNumber();

	setVoxelSize(xv,yv,zv, unit);
	run("Analyze Particles...", "size=0-Infinity pixel
circularity=0.00-1.00 show=Masks include stack");
	Imagetitle2="Mask of "+Imagetitle;
	selectWindow(Imagetitle);
```

```
	close();
	selectWindow(Imagetitle2);
	rename(Imagetitle);
	setThreshold(254,255,"black & white");

	Imagetitle2=Imagetitle+"Skele"
	run("Duplicate...", "title=&Imagetitle2 duplicate range=1-
&Sliceno");
	run("Skeletonize (2D/3D)");

	run("Analyze Skeleton (2D/3D)", "prune=none");
	selectWindow(Imagetitle2);
	close();

	imageCalculator("XOR create stack", "Tagged
skeleton",Imagetitle);

	run("Replace value", "pattern=185 replacement=20");
	run("Replace value", "pattern=128 replacement=115");
	run("Replace value", "pattern=225 replacement=180");

	selectWindow("Tagged skeleton");
	close();
	selectWindow("Results");
	run("Close");
	selectWindow(Imagetitle);
	close();
	selectWindow("Result of Tagged skeleton");
	Imagetitle3=Imagetitle+" Composite";
	rename(Imagetitle3);
	setLocation(10,10);
	run("In [+]");

	run("Install...");

}

//=================================================================
=========================
//======
//======
```

```
	function arrayByValue(A4,V){
		A5=newArray(nSlices);
		for (it=0;it<nSlices;it++){
			A5[it]=A4[it]*V;
		}
		return A5;
	}
//======
	function porosityArray(A1,A2){
		A3=newArray(nSlices);
		for (j=0;j<nSlices;j++){
			A3[j]=A1[j]/A2[j];
		}
		return A3;
	}
//======
	function ChangeResultWind(fob,rname){
		if (fob=="F"){
			IJ.renameResults("Results","ResultsPad");
			IJ.renameResults(rname,"Results");
			selectWindow("Results");
		} else if (fob=="B"){
			IJ.renameResults("Results",rname);
			IJ.renameResults("ResultsPad","Results");
			selectWindow("Results");
		} else waitForUser("Houston...we have a problem!");
	}
//======
	function array2Results(A,H){
		for (k=0;k<nSlices;k++){
			setResult(H,k,A[k]);
		}
		updateResults();
	}
//======
	function measureStack(col) {
		measureResultA=newArray(nSlices);

		for (i=0;i<nSlices;i++){
			setSlice(i+1);
			run("Measure");
```

```
                measureResultA[i]=getResult(col);
            }
        return measureResultA;
        }
//======
        function measure(col) {
            run("Measure");
            measureResult=getResult(col,(nResults-1));
        return measureResult;
        }
//======
        function alignHist(fpv,std){
            if(fpv>std){
                diff=fpv-std;
                run("Subtract...","value=&diff stack");
            } else {
                diff=std-fpv;
                run("Add...","value=&diff stack");
                for (i=1;i<=nSlices;i++){
                    setSlice(i);
                    changeValues(0,diff,0);
                }
            }
        }
//======
        function fstPeakMed(lwr,upr){
            //lwr=1;upr=65534;
            HighNo=0;
            HighRow=0;
            range=upr-lwr;
            setKeyDown("alt");
            run("Histogram", "bins=&range x_min=&lwr x_max=&upr
y_max=Auto stack");
            Plot.getValues(values, counts);
            close();
            //Array.print(values);Array.print(counts);
            for (i=0; i<=range-1; i++){
                if (counts[i]>HighNo){
                    HighNo=counts[i];
                    HighRow=values[i];
```

```
                        } else if ((HighNo-counts[i])>4000)
{i=(range-1);}
                  }
            //print(getTitle(),HighNo,"-",HighRow);
            Arr=newArray(HighNo,HighRow);
            return Arr;
      }
//======
      function CDF(lwr,upr){
            if (bitDepth()!=16){exit("Error Requires 16-bit
image");}

            //lwr=1;upr=65534;
            range=upr-lwr;
            setKeyDown("alt");
            run("Histogram", "bins=&range x_min=&lwr x_max=&upr
y_max=Auto stack");
            Plot.getValues(values, counts);
            close();
            //Array.print(values);Array.print(counts);
            sum=0;
            arA=newArray(range);
            for (i=0; i<=range-1; i++){
                  sum=sum+counts[i];
                  arA[i]=sum;
                  }
            //Array.print(arA);
            return arA;
      }
//======
```

Appendix 2| Image J macro, File contents for the RootOne first attempt. When Installed the macro is activated my consecutively depressing the 'W','E' and 'R' keys for the '*Exclude Outside*' function and preliminary version of RootOne. This provides an example of how the code can be hard coded for a specific application to make the code appear more automatic. This code also represents very early use of the Image J language and is cumbersome and slow.

Appendix 2

```
// ..............Tubeness Root segmentation.............
// file contents of "RootOne.img"
//load tiff stack with PVC and outside removed (values set to 0)
// set input stack to 16 bit
//
//
//===Remove outside
macro "RootOneprep1 [w]" {
setSlice(45);
makeOval(38, 46, 433, 431);
setTool(1);
}
macro "RootOneprep2 [e]" {
run("Crop");
run("Clear Outside", "stack");
}
//===

//===Root One
macro "Root1 [r]" {

tick=getTime();
run("16-bit");
Imagetitle = getTitle();
Sliceno = nSlices();

Res=0.06854831

// spatially callibrate images
Dialog.create("Calibrate Image:");
Dialog.addMessage("Please Enter Voxel Side Length:");
Dialog.addNumber("", Res, 6,8,"mm");
Dialog.addNumber("Slices in first scan:", 486);
Dialog.addNumber("Slices in second scan:", 460);
Dialog.addMessage("Check the stacks you want to save:")
Dialog.addCheckbox("Save the Grey Scale Corrected Stack?", true);
Dialog.addCheckbox("Save the Grey Fill Stack?", true);
Dialog.addCheckbox("Save the White Fill Stack?", false);
Dialog.addCheckbox("Save the Binary Stack?", false);
Dialog.addMessage("(Save Binary required for 3D vis)")
Dialog.addCheckbox("Require 3D vis of Binary Stack?", false);
Dialog.addNumber("Between Sample Standard Peak:", 22280);
Dialog.addCheckbox("Save Log file?", true);
Dialog.addCheckbox("Run fast?", true);
Dialog.show();
Voxdim = Dialog.getNumber();
scan1 = Dialog.getNumber();
scan2 = Dialog.getNumber();
goCorStack = Dialog.getCheckbox();
goGreyFill = Dialog.getCheckbox();
goWhiteFill = Dialog.getCheckbox();
goBinStack = Dialog.getCheckbox();
go3DVis = Dialog.getCheckbox();
Standard= Dialog.getNumber();
goLogFile= Dialog.getCheckbox();
goFast= Dialog.getCheckbox();


setVoxelSize(Voxdim, Voxdim, Voxdim, "mm");

scan2  = scan1+scan2;
```

```
scan11 = scan1+1;
scan22 = scan2+1;

//print(scan1,scan11,scan2,scan22,Sliceno)
selectWindow(Imagetitle);
run("Duplicate...", "title=[First] duplicate range=1-&scan1");
selectWindow(Imagetitle);
run("Duplicate...", "title=[Second] duplicate range=&scan11-
&scan2");
selectWindow(Imagetitle);
run("Duplicate...", "title=[Third] duplicate range=&scan22-
&Sliceno");

selectWindow("First");
nBins = 65535;
nBins1= 65534;
row=0;
HighNo=0;
run("Clear Results");

setKeyDown("alt");
run("Histogram", "bins=&nBins x_min=1 x_max=&nBins1 y_max=Auto
stack");
setLocation(1,22);
Plot.getValues(values, counts);

for (i=0; i<=nBins1; i++){
      setResult("Value", row, values[i]);
      setResult("Count", row, counts[i]);
      row++;
}
updateResults()
for (i=1; i<=nBins1; i++){
      if (getResult("Count",i)>HighNo){
            HighNo=getResult("Count",i);
            HighRow=i;
      }
}

//print("Highest Count:", HighNo);
//print("Corresponding Row:", HighRow);
Stack1mo= round(getResult("Value", HighRow));
//print("Stack 1 mode:",Stack1mo);

selectWindow("Second");
nBins = 65535;
nBins1= 65534
row=0;
HighNo=0;
run("Clear Results");

setKeyDown("alt");
run("Histogram", "bins=&nBins x_min=1 x_max=&nBins1 y_max=Auto
stack");
Plot.getValues(values, counts);
setLocation(1,290);

for (i=0; i<=nBins1; i++){
      setResult("Value", row, values[i]);
      setResult("Count", row, counts[i]);
      row++;
```

```
}
updateResults()
for (i=1; i<=nBins1; i++){
      if (getResult("Count",i)>HighNo){
            HighNo=getResult("Count",i);
            HighRow=i;
      }
}

//print("Highest Count:", HighNo);
//print("Corresponding Row:", HighRow);
Stack2mo= round(getResult("Value", HighRow));
//print("Stack 2 mode:",Stack2mo);

selectWindow("Third");
nBins = 65535;
nBins1= 65534
row=0;
HighNo=0;
run("Clear Results");

setKeyDown("alt");
run("Histogram", "bins=&nBins x_min=1 x_max=&nBins1 y_max=Auto
stack");
Plot.getValues(values, counts);
setLocation(1,559);

for (i=0; i<=nBins1; i++){
      setResult("Value", row, values[i]);
      setResult("Count", row, counts[i]);
      row++;
}
updateResults()
for (i=1; i<=nBins1; i++){
      if (getResult("Count",i)>HighNo){
            HighNo=getResult("Count",i);
            HighRow=i;
      }
}

//print("Highest Count:", HighNo);
//print("Corresponding Row:", HighRow);
Stack3mo= round(getResult("Value", HighRow));
//print("Stack 3 mode:",Stack3mo);
//print(Standard);

run("Clear Results");

selectWindow("Histogram of First");
close();
selectWindow("Histogram of Second");
close();
selectWindow("Histogram of Third");
close();
selectWindow("Results");
run("Close");

if (goFast==true){setBatchMode(true);}

if (Stack1mo > Standard){
      St1lw = Stack1mo - Standard;
```

```
	selectWindow("First");
	run("Subtract...","value=&St1lw stack");
}
else {
	St1lw = Standard - Stack1mo;
	selectWindow("First");
	run("Add...","value=&St1lw stack");
	SL=nSlices();
	for (i=1; i<=SL; i++){
		setSlice(i);
		changeValues(0,St1lw,0);
	}
}
if (Stack2mo > Standard){
	St2lw = Stack2mo - Standard;
	selectWindow("Second");
	run("Subtract...","value=&St2lw stack");
}
else {
	St2lw = Standard - Stack2mo;
	selectWindow("Second");
	run("Add...","value=&St2lw stack");
	SL=nSlices();
	for (i=1; i<=SL; i++){
		setSlice(i);
		changeValues(0,St2lw,0);
	}
}
if (Stack3mo > Standard){
	St3lw = Stack3mo - Standard;
	selectWindow("Third");
	run("Subtract...","value=&St3lw stack");
}
else {
	St3lw = Standard - Stack3mo;
	selectWindow("Third");
	run("Add...","value=&St3lw stack");
	SL=nSlices();
	for (i=1; i<=SL; i++){
		setSlice(i);
		changeValues(0,St3lw,0);
	}
}

Imagetitle1= Imagetitle+"cor";
//print(Imagetitle);
run("Concatenate...", " Title=Imagetitle image1=First image2=Second
image3=Third image4=[-- None --]");
rename(Imagetitle1);

////////////////////////////////////////
//setBatchMode(true);
//-------------------------------------------------------------------
--
Sliceno=nSlices();
a=(Sliceno/2);
aL=a+75;
aU=a-75;
UppTh = 2;
LowerTh = 1;
```

```
selectWindow(Imagetitle1);
run("Duplicate...", "title=Subsection duplicate range=&aU-&aL");

Sliceno2 = nSlices();
//Imagetitle = getTitle();
diffpeak=0;
DYDX=0;
minVal=1;
keepGoing=true;
j=1;

do {
      selectWindow("Subsection");
      jj="UpperThreshold "+(j+1);
      run("Duplicate...", "title=&jj duplicate range=1-&Sliceno2");

      print("Image:", jj);
      setThreshold(LowerTh, UppTh);
      run("Convert to Mask", " black");
      run("Set Measurements...", "area limit redirect=None
decimal=3");

      print("Counting Voxels...");
      k=1;
      sum=0;

      while (k<=Sliceno2){
            setSlice(k);
            run("Measure");
            sum=sum+getResult("Area", k+(Sliceno2*(j-1))-1);
            setResult("Sum",j-1,sum);
            //print("Counting voxels, slice...",k);
            k++;
      }
      print("Sum",sum);

      if (j>=2){
            y1=getResult("Sum",j-2);
            y2=getResult("Sum",j-1);
            x1=j-2;
            x2=j-1;
            setResult("DyDx",j-2,(y2-y1)/(x2-x1));
            DYDX=getResult("DyDx",j-2);
            print("Calculated DyDx", DYDX);
      }
//-----------------------------------------
      while (sum>0 && keepGoing==true){
            minVal=100*DYDX;
            print("minVal",minVal);
            keepGoing=false;
            }
//-----------------------------------------
      if (DYDX<minVal || DYDX>= diffpeak){
            //print("Going down IF");
            diffpeak=getResult("DyDx",j-2);
            inflex=UppTh-1;
            proceed=true;
      } else if (abs(DYDX-diffpeak)<5) {
            diffpeak=getResult("DyDx",j-2);
            inflex=UppTh-1;
            proceed=true;
```

```
      }else {
            //print("Going down ELSE");
            proceed=false;
      }

      selectWindow(jj);
      close();
      UppTh++;
      j++;
} while (proceed==true);


print("The inflection point sum differential:",diffpeak);
print("The inflection point Threshold Value",inflex);

UpperTh=round(0.78*inflex+0.6);

print("Corrected upper threshold estimate:",UpperTh);

//-----------------------------------------------------------------
--
// threshold roots from scan data
// improve by inserting threashold choice here rather than fixed
value
selectWindow(Imagetitle1);
setThreshold(LowerTh, UpperTh);
run("Convert to Mask", " black");
rename("Bin Roots");

// complete tubeness analysis
run("Tubeness", "sigma=&Voxdim use");
selectWindow ("tubeness of Bin Roots");
run("8-bit");
run("Auto Threshold", "method=Default stack");
selectWindow("Bin Roots");
run("Close");
selectWindow ("tubeness of Bin Roots");
rename("Bin Roots");

run("Duplicate...", "title=[WhiteVol] duplicate range=1-&Sliceno");
selectWindow("WhiteVol");
run("8-bit");
run("Set...","value=255 stack");

imageCalculator("Divide create stack", "Bin Roots", "WhiteVol");
imageCalculator("Multiply stack", "Result of Bin Roots",
Imagetitle1);
rename("Grey Roots");

// save outputs to file in sister directory
//Imagetitle = getTitle();
//Imagetitle1= Imagetitle+"cor";
selectWindow(Imagetitle);
Dir = getDirectory("image");
Direct = File.getParent(Dir);
//print(Imagetitle);
//print(Imagetitle1);
//print(Dir);
//print(Direct);
if (goCorStack==true){
```

```
      CorDir = Direct+ File.separator +Imagetitle1+
File.separator+File.separator;
      //print(CorDir);
      File.makeDirectory(CorDir);
      selectWindow(Imagetitle1);
      run("Image Sequence... ", "format=TIFF name=&Imagetitle1
start=0 digits=4 save=&CorDir");
}


if (goWhiteFill==true){
      GreyDir =
Direct+File.separator+"Grey"+Imagetitle1+File.separator+File.separat
or;
      File.makeDirectory(GreyDir);
      selectWindow("Grey Roots");
      GreyName = "Grey"+Imagetitle1;
      run("Image Sequence... ", "format=TIFF name=&GreyName start=0
digits=4 save=&GreyDir");
}

if (goBinStack==true){
      BinDir =
Direct+File.separator+"Bin"+Imagetitle1+File.separator+File.separato
r;
      File.makeDirectory(BinDir);
      selectWindow("Bin Roots");
      BinName = "Bin"+Imagetitle1;
      run("Image Sequence... ", "format=TIFF name=&BinName start=0
digits=4 save=&BinDir");
}

// create grey background and save
if (goGreyFill==true) {
      selectWindow("Grey Roots");
      Replace = UpperTh + 1;
      run("Replace value", "pattern=0 replacement=&Replace");

      GBDir =
Direct+File.separator+"GB"+Imagetitle1+File.separator+File.separator
;
      File.makeDirectory(GBDir);
      GBName = "GB"+Imagetitle1;
      run("Image Sequence... ", "format=TIFF name=&GBName start=0
digits=4 save=&GBDir");
}

// clean up unnecessary stacks
selectWindow("WhiteVol");
close();
selectWindow("Tubes");
close();

if (goFast==true){setBatchMode(false);}

//setBatchMode(false);

// view in 3D viewer

if (go3DVis==true) {
```

```
      run("Image Sequence...", "open=&BinDir number=&Sliceno
starting=1 increment=1 scale=100 file=[] or=[] sort");
      run("3D Viewer");
      call("ij3d.ImageJ3DViewer.setCoordinateSystem", "false");
      call("ij3d.ImageJ3DViewer.add", BinName, "None", BinName, "0",
"true", "true", "true", "2", "0");
      }

tock=getTime();
time=(tock-tick)*0.00001666;
print(time);
if (goLogFile==true){
      selectWindow("Log");
      saveAs("Text",
Direct+File.separator+"logfile"+Imagetitle+".txt");
}
// beep, allert or email...exec()
// computational time
selectWindow("Results");
run("Close");
selectWindow("Log");
run("Close");
wait(1000);
beep();
}
```

Appendix 3

Appendix 3| File structure and import protocol for GE Phoenix *.vol files.

The *.vol produced by GE Phoenix *Reconstruction* software contains the voxel contents of the volume reconstructed. The file has no separators, headers or offset bytes to the first image or between images. The byte order is little endian. Since there is no data on the dimensions or bit depth available from the header of the file, prior knowledge is required to easily import the file. Such information can be found in the *.vgi file simultaneously created by the *Reconstruction* program. The essential information to be extracted from the *.vgi file is the bit depth (16- or 32-bit etc) height, width and number of slices (in pixel units). The isotropic voxel size can also be extracted to calibrate the image upon import. Having extracted these values, the image can be imported as a raw file type. The data is arranged according to the voxel co-ordinates incrementing first in width (w), then in height (h) and finally in slice (s). e.g.

(0,0,0), (0,0,1) … (0,0,w-1);
(0,1,0), (0,1,1) … (0,1,w-1);
… (0,h-1,w-1);
… (s-1,h-1,w-1);

Appendix 4

Appendix 4| Image J macro tool used to identify the grey value of the 'soil' peak (mode) and manually determine the ideal threshold value. The macro records the values identified in a unique log file.

```
macro "Flavel Indentify 1st Peak Action Tool -
C090L0f50L50afL5fa0La0ff"{
	requires("1.46c");
	if (bitDepth()!=16){run("16-bit");}
	sample=getTitle();
	A=fstPeakMed(1,65534);

	print("Peak Height",A[0],"-","Peak Grey Value",A[1]);

	run("Threshold...");

	waitForUser("","Please insert threshold value: ");

	Dialog.create("Set threshold");
	Dialog.addMessage("Please enter the grey-scale \nvalue you
want the peak to be at:");
	Dialog.addNumber("Grey value:", 30000,0,10,"");
	Dialog.show();
	sx = Dialog.getNumber();
	print("Ideal threshold grey value: ",sx);

	selectWindow("Log");
	SaveName="/Users/rflavel/Desktop/"+sample+".txt";

	saveAs("Text",SaveName);
	selectWindow(sample);
	run("Close");
	selectWindow("Threshold");
	run("Close");
	selectWindow("Log");
	run("Close");
	//alignHist(A[1],std);
	//if (prnt==true) {print("Peak Height:",A[0]," Peak
Value:",A[1]);}
	}
//======
function fstPeakMed(lwr,upr){
	//lwr=1;upr=65534;
		HighNo=0;
		HighRow=0;
		range=upr-lwr;
		setKeyDown("alt");
		run("Histogram", "bins=&range x_min=&lwr x_max=&upr
y_max=Auto stack");
		Plot.getValues(values, counts);
		close();
		//Array.print(values);Array.print(counts);
		for (i=0; i<=range-1; i++){
		if (counts[i]>HighNo){
			HighNo=counts[i];
			HighRow=values[i];
			} else if ((HighNo-counts[i])>40000) {i=(range-
1);}
		}
	//print(getTitle(),HighNo,"-",HighRow);
	Arr=newArray(HighNo,HighRow);
```

```
return Arr;}
```

Appendix 5

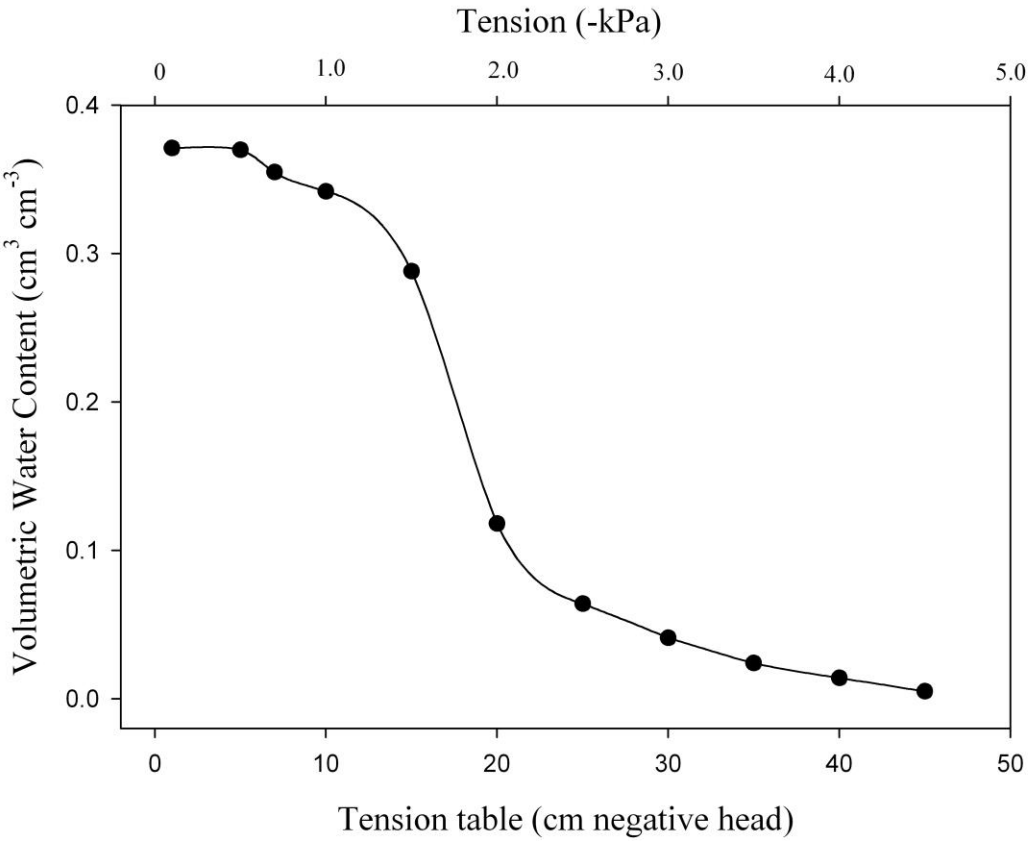

Appendix 5| Volumetric water content (cm^3cm^{-3}) of 90:10 Sand:Ferrosol (w/w) composite medium packed to oven dry bulk density of 1.37 gcm^{-3}. Determined using tension table with kaolin bed and de-aired water. Depicting the 'wet end' of the moisture release curve to demonstrate the dramatic gradient of moisture content observed in the experimental apparatus Chapter 5.